UNIVERSITY
OF TRENTO - Italy
DEPARTMENT OF INDUSTRIAL ENGINEERING

XXVIII cycle

Doctoral School in Materials Science and Engineering

OPTIMIZATION OF A PVD DEPOSITION SYSTEM FOR THE REALIZATION OF DICHROIC FILTERS USED IN CPV SPECTRAL SEPARATION SYSTEM FOR THE ENERGY PRODUCTION

WALTER RANIERO

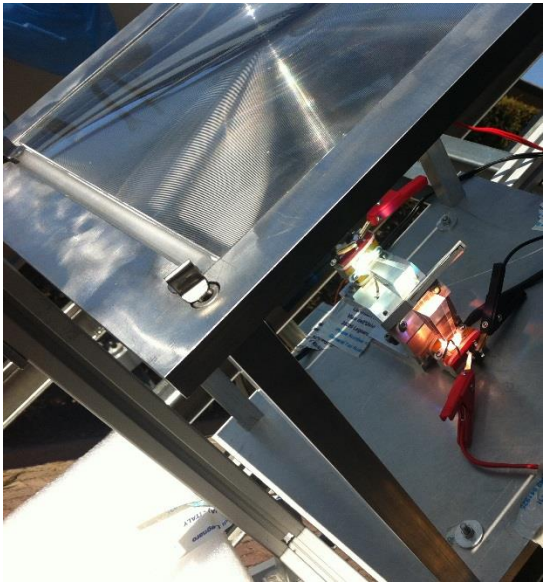

December 2015

OPTIMIZATION OF A PVD DEPOSITION SYSTEM FOR THE REALIZATION OF DICHROIC FILTERS USED IN A CPV SPECTRAL SEPARATION SYSTEM FOR THE ENERGY PRODUCTION

WALTER RANIERO
E-mail: walter.raniero@unitn.it

Approved by:

Prof. Gianantonio Della Mea, Advisor
Department of Industrial Engineering
University of Trento, Italy.

Ph.D. Commission:

Prof. Donato Vincenzi,
Department of Physics and Earth Science
University of Ferrara, Italy.

Prof. Gino Mariotto,
Department of Informatic
University of Verona, Italy.

Prof. Quaranta Alberto,
Department of Industrial Engineering
University of Trento, Italy.

University of Trento,
Department of Industrial Engineering

December 2015

University of Trento - Department of Industrial Engineering

Doctoral Thesis

Walter Raniero - 2015
Published in Trento (Italy) – by University of Trento

ISBN: - - - - - - - - -

A mio Padre…

Abstract

Photovoltaic technology in the field of renewable energy has reached a high commercial interest over the past decade.
The traditional silicon photovoltaic systems that is currently the most widespread, mainly due to government subsidies, have a low energy production.
The wide use of material and the low efficiency of the silicon modules required the research and development of photovoltaic systems more efficient.
The most promising technology is the photovoltaic concentration that increases the efficiency of the modules by reducing the area of the PV cell.
The concentration photovoltaic has had considerable technological progress related to the development of multi-junction PV cells with high efficiency.
Another approach is the technology of photovoltaic concentration with the spectral separation, so using the interference filters the solar spectrum is splitted into different optical bands.
In this research was designed and built a CPV prototype system with spectral separation.
The interference filters such as anti-reflection and dichroic mirror are made up of silicon dioxide and titanium dioxide. These oxides have been realized by means of physical vapor deposition reactive magnetron sputtering technique. The PVD technique allows to deposit thin films with a homogeneous process reproducible and reliable.

In the first part of the work, the characterization of individual layers of oxide materials have allowed to extrapolate the optical constants. This is necessary for the design of the optical multilayer.
The characterization has nvolved various analyzes such as atomic force microscopy (AFM) to determine the thickness and the roughness, compositional analysis Rutherforf backscattering spectrometry (RBS), and optical analysis UV-Vis-NIR.
These analyzes were necesary to calibrate the deposition system in order to subsequently to realize the multilayer optics. The as deposited optical

multilayers not confirm the optical design, and it was necessary to carry out an annealing at 350°C.

In the second part of the work, there were also micro structural characterizations for evaluating the phase variation of the titanium dioxide with the annealing treatment.
The Fourier transform infrared (FT-IR) analysis has checked the absorption peak of the Ti-O-Ti of the crystalline phase.
In addition, X-ray diffraction (XRD) analysis verified the phase variation of titanium dioxide from purely amorphous phase with a slight presence of rutile to the anatase phase. Through the optical analysis it was possible to extrapolate the new optical constants corresponding to the phase of anatase.

In the third part of the work, the ray tracing design of optical splitting of the CPV prototype was carry out.
The CPV system is designed by coupling a concentration Fresnel a dichroic mirror. The focus of the radiation on the PV cell, is simulated by two ideal detector. The optical optimization as function of the f-number of the lens has allowed to define the layout for the prototyping phase.
A further optimization is to insert a secondary optics element (SOE) of homogenization. The secondary optics will also limits the optical losses due to a misalignment of the CPV prototype.

In the last part of this thesis is devoted to the preparation and the characterization of the CPV prototype.
Were performed measures of solar radiation, which combined with the characteristic I-V-P curves of the solar cells have enable to evaluate the efficiency of the prototype system. The efficiency of the spectral separation system was compared with concentration multi-junction PV cells.
Daily measurement were performed to compare the spectral separation technology than to the multi-junction technology. The results show that the separation system maintains a more constant performance during the day

Finally, thermal measurements were conducted on the component of the CPV prototype separation system. The experimental results allows to guarantee that the spectral separation is also a selective filter of temperature.
This allows the solar cells to maximize the photovoltaic conversion and to reduce the overheating.

Table of contents

List of Figures

List of Tables

List of abbreviation and acronyms

n(λ) - Refractive index
k (λ) - Absorption index
T% - Relative transmittance
R% - Relative reflectance
R_F - Partial reflectance
T_F - Partial transmittance
h - Slab thickness
α - Coefficient of thermal expansion
nd - Refractive index D Fraunhofer line
nf - Refractive index F Fraunhofer line
nc - Refractive index C Fraunhofer line
CPV - Concentrated Photovoltaic System
BK7- Glass borosilicate
PMMA - Poly-metilmetacrylate
GaAs - Gallium Arsenide
Si - Silicon
SR- Spectral Response
EQE - External quantum efficiency
η_{GaAs} - Gallium Arsenide efficiency
η_{Si} - Silicon efficiency
η_{SYSTEM} - Prototype efficiency
FF - Fill factor
V_{OC} - Open Circuit Voltage
I_{SC} - Short Circui Current
FTIR - Fourier Transform Infrared
AFM - Atomic Force Microscope
RBS - Rutherford Back Scattering
SEM - Scanning Electron Microscope
PVD - Physical Vapor Deposition
f/# - f-number
DNI - Direct Normal Irradiance
MJSC - Multi Junction Solar Cell
SJSC - Single Junction Solar Cell

DJSC - Dual Junction Solar Cell
ε - Material Emissivity
T [°C] - Temperature
I-V - Current Voltage characteristic curve
V-P - Power Voltage characteristic curve
P_{MAX} - Maximum Power
I [A] - Current
V [V] -Voltage
EFL - Effective Focal Length
R_a - Algebraic roughness
R_q - Quadratic roughness
NO - Imaging optics
NOI - Non-imaging optics
SOE - Secondary optical element
POE -Primary optical element
AM - Air Mass
I - Solar Irradiance
SE - Secondary Electron
BSE - Back Scattering Electron

Chapter I

Introduction

Since the late 70s of the increasing research in semiconductor development has enabled us to develop photovoltaic technology.
The constant technological research in the production of photovoltaic cells, has resulted in an increase of efficiency with a reduction of cost. This has allowed the constant effort in the development of photovoltaic concentration systems for the production of energy [1].
The photovoltaic concentration system has as a primarily advantage significantly reducing the area of photovoltaic cell promoting this technology as economically attractive. Concentrating systems require a dual-axis tracking of the sun, which increases the daily energy yield.
On the other hand, in the last decade the devolpment of the flat silicon technology has had a strong expansion, facilitated also by government subsidies.
The continuous development of cells with high performance materials has allowed us to develop new technologies for converting solar spectrum and thus has allowed the development of system gradually more and more efficient. A further advantage of the concentration is to increase the efficiency of solar cells (Figure I-1).
The concentration III-V multi-junction solar cells have a better performance in the middle of the day where the energy demand is greater. This technology is therefore rigged for very competitive as it has the ability to get higher revenues than traditional photovoltaic systems.

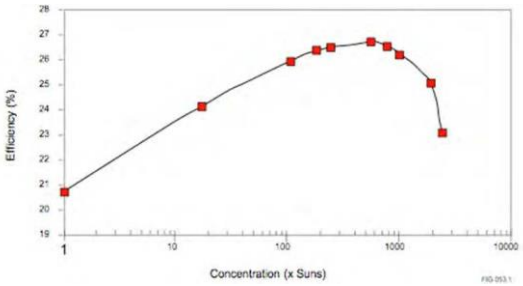

Figure I-1. Mono-crystalline silicon solar cell efficiency vs solar concentration [1].

In this thesis we have developed a new approach exploiting technologic separation of sunlight into optical bands adapted to the response of quantum semiconductor materials with different band-gaps.
As a comparison, multi-junction PV cells are formed by different semiconductor layers connected in series [2]. The total current is limited by the subcell which produces less current and therefore the daily energy yield is inconstant.
The spectral separation rather each cell operates individually and energy production is more constant during the day.
These cells, like GaAs, InGaP, Ge, etc., are applied in systems using geometrical optics for solar concentration. The concentration ratio has reduced areas of semiconductor used, by reducing the necessary amounts n of material.

In this way, the technology of optical concentration, as the Cassegrain approach or with Fresnel lenses, has as main advantage to reduce the costs linked to decrease the semiconductor area used for photovoltaic conversion [3].
On the other hand, the concentration photovoltaic systems require a solar tracking apparatus and a better angular resolution in function of the acceptance angle of the concentration, which incease the overall costs .
The use of photovoltaic systems (CPV) allow however to increase the recyclability of the installations up to a share of 97% [4]. This is due to the large use of recyclable materials such as glass, aluminum and steel (Figure I-2).

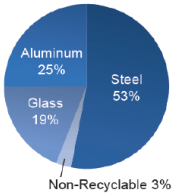

Figure I-2. Recyclable materials in concentrating photovoltaic system CPV [4].

Another advantage of the CPV system is the reduction of cooling water use compared to other technologies. [5] (Figure I-3).

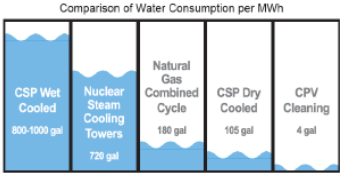

Figure I-3. Water consumption in the different energy technologies [5].

The concentration systems have low production of CO_2 in their life cycle and have the ability to integrate with the surrounding environment. The CPV technology could have a dual use as both energy production and the possibility of breeding underlying modules (Figure I-4).

Figure I-4. Dual use of land: energy production and livestock farming [5].

As previously mentioned, the photovoltaic concentration technology has been commercially developed with systems with high efficiency multi-junction cells. This PV cell is composed by a stacking of coupled junction with different optical absorption bands and allow to cover most of the solar radiation and thus to increase the overall efficiency of the system (Figure I-5) [6].

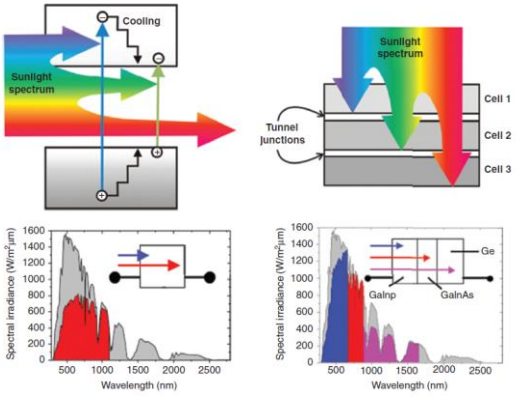

Figure I-5. Comparison of solar spectrum conversion of the silicon and the multi-junction solar cell.

Most research efforts aimed at increasing efficiency at all levels from cell to module to system. The trend lines is shown in Figure I-6 in are based on the expectations of the European Photovoltaic Technology Platform in 2011 [7] of Strategic Research Agenda (SRA). It is possible to note an increase in efficiency since 2000 with a progress from basic research and development efforts.

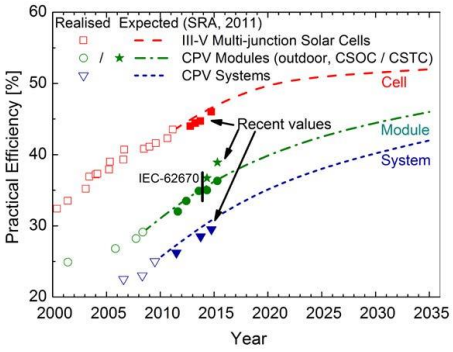

Figure I-6. Trend line of multi-junction solar cell, module and system efficiency compared with the collected published results [8].

In previous studies and applications [9] [10], since the early 2000s, many international laboratories carried on different multispectral approach, developing concentration systems using spectral separation of the light in different optical bands.

The philosophy of this technology is to split the solar spectrum in predefined optical bands with interference filters or beamsplitters. Each optical band is coupled to a PV cell with different energy gap (Figure I-7) [11].

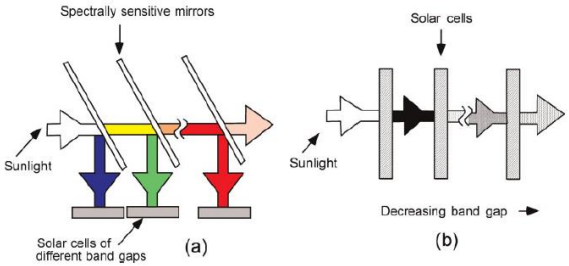

Figure I-7. Multi-junction cell concepts: (a) spectrum splitting; (b) cell stacking

In splitting system, each cell can be separately designed on unique optimized substrates without concern for substrate transparency or lattice mismatch.
Furthermore, there are several factors of optical loss with the introduction of dielectric beam splitting filters. The optical losses are linked to the edges slope transition between reflective and transmissive optical band that collect the wavelengths at the different PV cells.
In addition, the Fresnel optical losses, angular sensitivity, and misalignment issues lower the efficiency of the CPV system [12].
In order to convert a wide interval of the solar spectrum [13], international research focused on the realization of prototypes for the spectral separation based on single-junction cell [14] or dual-junction cell [11] [15] with one or more spectral separations in many different optical configurations.
Another example of the spectral separation application is in cogeneration systems where the ultraviolet and infrared optical bands of the spectrum are used for thermal generation, and the visible band is converted by PV systems [16] [17] [18].

Since 2004 the University of Trento (Department of Industrial Engineering) and the Materials Laboratory of the National Institute of Nuclear Physics (INFN) Legnaro (PD), were among the top research institutes in Italy, in collaboration with the Department of Physics of Ferrara University, studing the application of dichroic filters to concentrator PV systems.

The purpose of this research thesis is to optimize a physical vapor deposition (PVD) reactive magnetron sputtering system to realize dichroic filters to use in the photovoltaic concentration.
In particular, the aim to create and to optimize a dichroic mirror using low cost materials with good optical properties, in order to apply to future commercial CPV systems.
Currently there is no commercial CPV system with spectral separation with dichroic, mainly due to the high cost of dichroic filters.
The research focused of for pre-industrial production.
The use of readily available low cost materials and a careful design phase and production led to dichroic mirrors with a low number of layers with very good optical characteristics.

The research activity was organized into two different macro areas, which are the dichroic filter design and production and the CPV system prototype.

The research on the dichroic filter was structured as follows:

- Design and production of optical multilayer thin film;
- Characterization of thin film optical multilayer.

The research prototype system CPV was organized as follows:

- Planning and optimization of optical CPV splitting system;
- Construction and characterization of a prototype CPV splitting system.

The coating materials used in the design of dichroic filters are titanium dioxide and silicon dioxide. These materials are widely used in optical interference filters such as anti-reflection filters on photovoltaic cells [19]. They good optical properties in terms of refractive index and extinction coefficient and they are relatively cheaper material.

The optical design of the antireflection and dichroic filters was performed using a dedicated software for thin films, Tf_Calc®. In particular, have been achieved and optimized different optical designs to realize different optical multilayer filters.
Single layer samples of TiO_2 and SiO_2 were produced in order to determine their optical constants $n(\lambda)$ and $k(\lambda)$ by spectrophotometric analysis.
The deposition of single layers was also used to calibrate the PVD reactive magnetron sputtering system. PVD process parameter, as set point voltage deposition is selected by the thin film characterization to evaluate the hysteresis curve of reactive sputtering [20].
Rutherford Back Scattering analysis on single layer thin film allows to quantify the stoichiometric ratio O/Si and O/Ti at different deposition conditions necessary to calibrate the deposition system. The RBS analysis also allows to determine the spatial homogeneity of the deposition. So, the maximum deposition area where the thin film is homogeneous can be evaluated [21].

In order to determine the rate deposition and the quality of the surface [22] [23], every single layer was analyzed by atomic force microscope (AFM) for measuring both the the thickness and the surface roughness.

In order to investigate the interfaces of the multilayer coatings, we analyzed the sample in cross section with a scanning electron microscope (SEM).

The optical multilayers have undergone a process of thermal annealing to stabilize and optimize the optical response of the materials deposited.
Using Fourier transform infrared spectroscopy (FT-IR) [24] [22] and X-ray diffraction (XRD) [22] [25] techniques it has been possible to evaluate the change of phase of the titanium dioxide affecting the multilayer optical properties.
UV-Vis-NIR spectroscopy in transmission and reflection has been used to analyze the response of the optical multilayer in the range between 350nm to 1200nm.
These analyses allow to study the variation of optical constants $n(\lambda)$ and $k(\lambda)$ of the titanium dioxide correlated to the phase variation occurred with the annealing process at 350°C [26] [27]. The results has been compared with optical designs, providing the correlation between the optical responses of the heat treated optical multilayer with the process of annealing.
The spectrophotometric analysis provides the optical transmittance response at different incidence angle of multilayer [14].
The analysis of the optical multilayer transmittance as a function of incidence angle is an important parameter to proceed in the ray tracing optical design, necessary to realize a prototype CPV using a Fresnel lens.

The CPV optical design was performed with the software, Ray Tracing Zemax®. In particular, an analysis was conducted to optimize the optical geometrical coupling between an optical primary Fresnel lens (POE) and a dichroic filter, designed for focusing the spectral intervals with a non-imaging lens on two different PV cells.
The dichroic filter divides the spectrum into two optical band, one of these is transmitted on a silicon PV cell and the other one is reflected on a GaAs PV cell.

The design was conducted taking into account the optical efficiency of the splitting system by varying the lens f-number, which is the ratio between the focal point and the lens diameter.

It was conducted also an optical design of a secondary optics (SOE) to improve the uniformity of concentrated solar radiation on the 'surface of the photovoltaic cell. The homogenizers, besides increasing the uniformity of radiation distribution, also improves the angular acceptance of the prototype system.

The photovoltaic concentration systems operate only with direct sun radiation (DNI) and therefore require a solar tracking system. To characterize the prototype it was necessary to measure the I-V-P characteristic curves and the fill factor of PV cell exposed to the concentration set up.

In collaboration with the Department of Physics of University of Ferrara, the Akkutrack solar point and tracking measurement was used, allowing to track the sun with high angular sensitivity of 0.1°.
The irradiance acquisition allowed to perform daily measurements, to evaluate the prototype separation efficiency and to compare with a commercial multi-junction concentration system.

Finally, we perfomed thermal measurements of the splitting system to determine the thermal selectivity of the dichroic filter.
The thermal analyses were carried out by simulating the photovoltaic cell with a target of known material by measuring the temperature during the different irradiation condition.
The temperature has been dectected into the material with a thermocouple, while the surface temperature was detected by infrared thermography measurements.

Chapter II

Background

2.1 Photovoltaic system for energy production

The increase in energy demand worldwide, linked to the issue of reduction of polluting gases as described in the Kyoto Protocol [28] of 1997 has allowed a reduction of 5% in 2008-2012 and in 2011 after the extension of the protocol, in the second phase was forecast to decline in 2013-2017.
Such restrictions have allowed us to increase research on renewable energy sources (RES) as the production of energy and heat, limiting emissions from biomass and energy efficiency of buildings.
In particular, the photovoltaic sector has been introduced in Italy since 2005 with the first "conto energia" that included a gain for every kWh produced by the installation. These profits were derived from direct sales of electricity fed into the grid and rewarding the first self-consumption. In contrast to European countries such as Germany or Spain, which provided only the proceeds of the electricity fed into the grid.
The first "conto energia" in 2005-2006 included a remuneration energy fed into the grid only for large PV installations, while the plants with production of less than 1 MWp had no access with incentives. This limitation has been revised with the introduction of the second "conto energia" that included a remuneration depending on the characteristics of the PV system, as not integrated, partially integrated and fully integrated in buildings and depending on the size of the plant.

This process was designed to promote the distribution of small residential systems by increasing the production of energy distributed. The incentives profitable is favorable attracted numerous foreign funds and the installation companies of small and medium plants that have seen the Italian market as an excellent business opportunity.
From 2011 it was introduced the third "conto energia" during which in Italy 3.27 GW were already installed and connected, and 7.22 GW of plants considering the plants built before 2010 and not connected. The economic crisis urgently in Italy meant that the energy bill ended just after five months of initiation.
With the fourth "conto energia" in 2011 it was further revised the remuneration system according to the power produced each semester. If the installed power produced exceeds the cost limit imposed for the incentives, the remuneration is reduced. This is to prevent the exponential growth of installations to get government subsidies.
Since August 2012 with the fifth "conto energia" there was even more of an increase in remuneration for small plants and provided an incentive fee which provided both the incentive that the price of electricity sold and a bonus tied for self. A government policy aimed at small plants that encourage consumption.
The introduction of the fourth "conto energia" [29] since 1 June 2011 also concentrated photovoltaic systems can benefit from government incentives with an installed power of between 1 and 5 MW.
This has allowed the installation in Italy of a new photovoltaic concentration, allowing also to develop a technological research of new CPVprototypes.

2.2 Renewable Energy: Photovoltaic systems technology

2.2.1 Traditional PV

The traditional systems of silicon merely convert a part of the solar spectrum into electrical energy (Figure II-1).

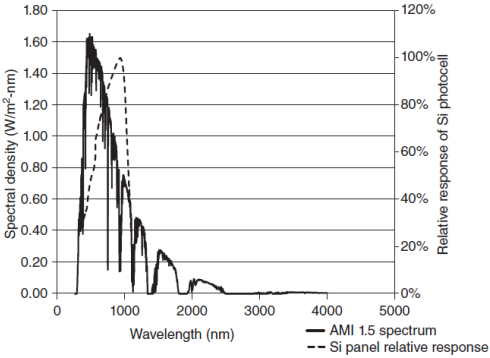

Figure II-1. Solar spectra AM 1.5 compare with silicon junction conversion [30].

The photovoltaic cell can be described by the equivalent circuit shown in Figure II-2.

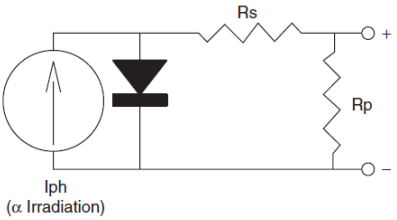

Figure II-2. Equivalent circuit of single junction solar cell.

$$I_g = I_{ph} - I_0 \exp\left(\frac{qV_g}{kT} - 1\right) \qquad 1)$$

To determine the short circuit current, set $V_g = 0$ and $I_{sc} = I_{ph}$ and this value changes proportionally to the cell irradiance (Equation-1). To determine the open circuit voltage V_{oc} (Equation-2), the cell have to current $I_g = 0$ [6].

$$V_{oc} = \frac{kT}{q} ln\left[\frac{I_{ph}}{I_0}\right] \quad 2)$$

In the Figure II-3 it is shown the characteristic curve (I-V-P) of a photovoltaic cell.

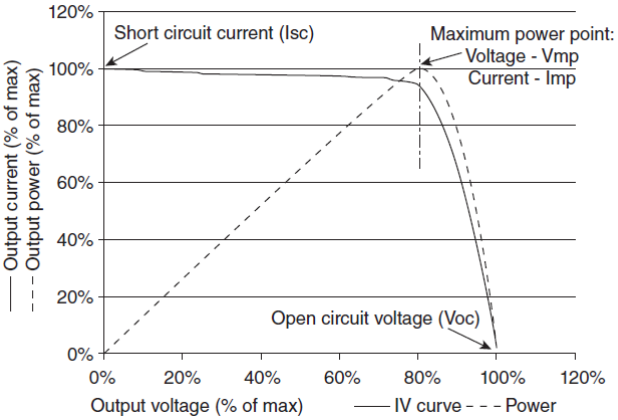

Figure II-3. I-V-P Characteristic curve of photovoltaic solar cell [30].

The product of the current and voltage produces a power–voltage curve, and series and parallel resistances (Rs and Rp) will cause deviation from ideal photodiode characteristics curve, and a figure of merit called the fill factor that identify what is the 'quality factor' of the cell (Equation-3).
Finally, through the Equation-4 is possible to define the efficiency of the PV cell.

$$FF = \frac{V_{mp} \times I_{mp}}{V_{oc} \times I_{sc}} \quad 3)$$

$$\eta = \frac{FF \times V_{0c} \times I_{sc}}{P_{in}} \quad 4)$$

Series Resistance (Rs) represents the contact resistance between the grid-metal and the surface of the crystal, and Parralel Resistance (Rp) is due to the losses current of the junction and it method used to realize the junction.
The fill factor in practice, even for photodiodes with very low Rs and very high Rp, cannot reach the maximum of 100% since the ideality factor of the diode itself contributes to the rounding of the I-V curve.

2.2.2 Concentrated Photovoltaic (CPV)

The main advantage of concentrated photovoltaic systems is to reduce the area of the used semiconductor significantly lowering the cost of the final CPV system [30].
For example is consider the Si module and the small point-focus CPV module a commercial flat plate module with 13% polycrystalline silicon solar cells with power rating of 110 W, and active semiconductor area of 62 cm * 152 cm. In contrast, one unit in the concentrator module operates at 500 suns using a 0.55 cm * 0.55 cm multijunction cell with efficiency of 37%.
Generating an equivalent power of 110 W in the CPV module is achievable from the following simple calculation: 0.37 * (0.55 cm * 0.55 cm) * 0.75 * N * 50 W cm^{-2} = 110 W where N is the number of multijunction cells and 0.75 is the optical efficiency of the module. Twenty-six cells (or 7.9 cm^2 of semiconductor area) would be required for producing the same power which is less < 0.1% of the total area of the Si cells [31].

2.3 Concentrated photovoltaic system

2.3.1 Multi-junction (MJSC) CPV system

Solar cells made of III–V semiconductors reach the highest efficiencies of any photovoltaic technology so far..
A three subcells junction system (Figure II-4) consists of GaInP, GaInAs, and Ge are stacked on top of each other and interconnected by tunnel diodes.

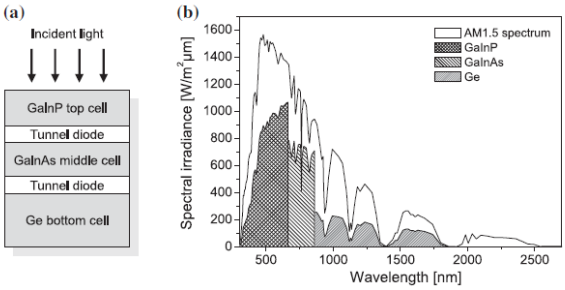

Figure II-4. a) Schematic structure of GaInP-GaInAs-Ge triple-junction solar cell. b) Spectral irradiance of the AM 1.5 spectrum and the part of the spectrum converted by triple-junction solar cell [2].

The most efficient use of the solar spectrum is obtained with every subcell with a higher band gap than the one below. In this way, each subcell absorbs the spectral range with energy lower than its band gap, and the transmission losses can also be reduced if the lowest band gap of the stack has a lower band gap than the conventional single-junction solar cells.
The subcells are connected in series within the multijunction solar cell and the total current is limited by the lowest current.
CPV systems using multijunction solar cells have another advantage. Due to the use of expensive semiconductor material the size of the system is reduced in order to be less expensive [31].

2.3.2 Solar splitting CPV system

The challenge of current multijunction solar cells can be overcome by using optical beam splitting, where an optical filter separates the light into spectral components directed onto individual cells of different band-gap energies (Figure II-5).

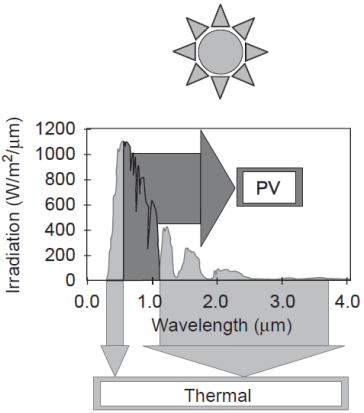

Figure II-5. Splitting the solar spectrum into components for PV and thermal energy conversion [32].

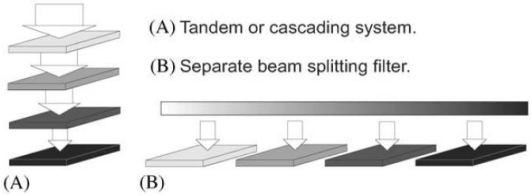

Figure II-6. Two schemes for PV spectrum splitting [32] .

In Figure II-6 case (B), light is separated into different spectral components by a beam splitting filter and it is directed onto individual cells. In this way, each cell can be separately designed, and manufactured by optimizing the substrates without concern for the transparency or lattice mismatch problems. Moreover, there are no constraints on the currents flowing through each ofthe cells; hence, the spectrum splitting approach has a slightly higher theoretical efficiency with respect to the cascading approach.

The technique of spectral separation has been known for some decades. In the Figure II-7 is possible to note a first diagram of the spectral separation with the use of a dichroic filter already in 1978. In this system, were used two single junction cells for the high to low wavelengths.

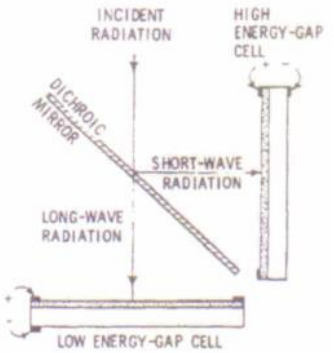

Figure II-7. First splitting system with the use of the dichroic filter and two photovoltaic cells [33].

From the 2000s the spectral separation technology for concentration systems with multijunction cells begins increasingly popular, mainly due to the use of much more efficient tracking systems from telecommunications and to the lowering of the costs of the optical components.

The research and development of photovoltaic systems for the renewable energy, allowed, thanks to a political and economic commitment of many countries, to develop different solutions for energy production from alternative energy sources. On this basis it was possible to resume the idea of spectral separation by Moon on 1978 [33] and to apply it in different ways for high efficiency prototypes based on the spectral separation on single, dual and triple-junction solar cells.

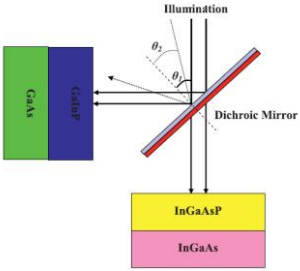

Figure II-8. Light splitting system with double junction solar cells [34].

2.3.2.1 State of art: single, dual and triple junction solar cell

In Figure II-9 is shown the Cassegrain solar concentrator module concept. It shows a primary concentrator lens and a secondary dichroic mirror to split the solar spectrum into two parts, by directing the infrared and near visible bands of the spectrum to two separate cells. An efficiency of 32.9% is reported to the solar concentrator PV module using InGaP/GaAs dual junction (DJ) cells located at the near-visible focus at the center of the primary and the GaSb infrared solar cells located behind the secondary [35].

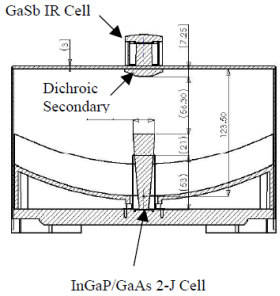

Figure II-9. Cassegrain PV module with dichroic mirror that separate the solar spectrum on different PV cells [35].

Figure II-10. Cassegrain CPV modules on 2-axis solar tracker.

Table II-1. CPV Cassegrain efficiency results.

	Packaged Cells at STC	Projected STC with 90% Optical Effic	Measure at Operate Temp (April 28)	Measure Module at STC (April 28)
DJ Cell Power	17.4 W	15.7 W	14.4 W	15.1 W
DJ Cell Effic.	31.5%	28.4%	26.1%	27.3%
IR Cell Power	3.64 W	3.28 W	2.6 W	3.1 W
IR Cell Effic.	6.6%	5.9%	4.7%	5.6%
Sum Power	21 W	19 W	17 W	18.7 W
Sum Effic.	38.1%	34.3%	30.8%	32.9%

NIP DNI = 0.92; Area = 600 cm2; Input Power = 55.2 W

In Figure II-11 is presented a multi-junction receiver based on the multiple geometry spilitting. This configuration offers complete freedom in solar cell selection, and represents a straightforward arrangement for realizing a light trapping spectral beam-splitting photovoltaic receiver [36].
This geometry provides a good basis to build a highly efficient photovoltaic receiver by minimizing the reflection losses. The reflected sunlight is always

directed to the next solar cell inside the module. Hence, the architecture provides several absorption possibilities for a wide spectral range.
In order to further reduce optical losses, the spectrally selective beam-splitters are placed directly in front of the solar cells.

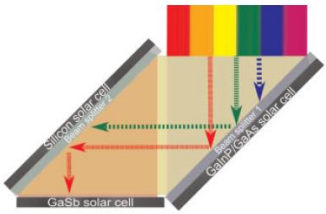

Figure II-11.Spectral beam splitting design including three solar cells and two beam splitter [36].

Figure II-12 shown an example of a designed selective beam-splitters dividing the solar spectrum into three parts. Each beam-splitter should ideally transmit the sunlight between 300nm and 850nm and reflect the light at higher wavelengths in the region of 850–1800nm.
They consist of stacks made of two materials deposited one glass substrate with hundred layers of TiO_2 and SiO_2 used to realize interference systems.

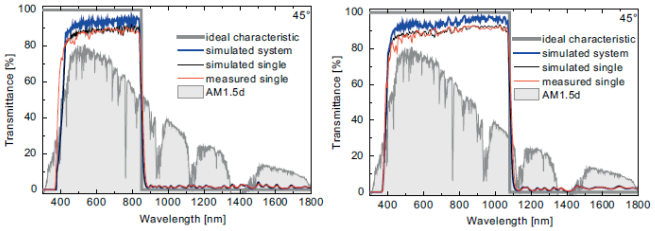

Figure II-12. Optical transmittance of beam-splitter as a function of wavelength with cut-off at 850 and 1080 nm [36].

In Table II-2 shown the efficiency results of Beam-splitting photovoltaic system with two dichroic mirror at AOI=45°.

Table II-2. Efficiency of the spectral beam-splitting system.

	FF (%)	V_{oc} (V)	η_{Ideal} (%)	η_{Sim} (%)	η_{Proto} (%)
$Ga_{0.51}In_{0.49}P$	85.8	2.32	26.7	23.8	24.1
GaAs					
Silicon	73.3	0.65	5.19	5.75	5.75
GaSb	61.6	0.29	2.44	2.27	2.28
System (Σ)			34.3	31.8	32.1

In Figure II-13 shown a system with spectral separation of CPower Srl [37] with a primary optic concentration in reflection and the use of the spectral separation with a dichroic filter placed behind an optical secondary.

In such a system are used different cells single, double and triple junction and the experimental results of system efficiency are summarized in Table II-3.

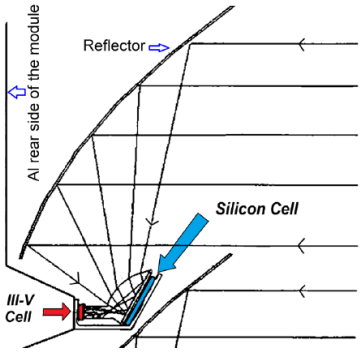

Figure II-13. Ray tracing design of CPV reflection spectra splitting [37].

Figure II-14 shows the variation of the optical transmittance of an optical filter at different angles of incidence. This describes the importance of accurate alignment and a correct solar tracking in order to optimize the optical coupling between the cells and the dichroic.

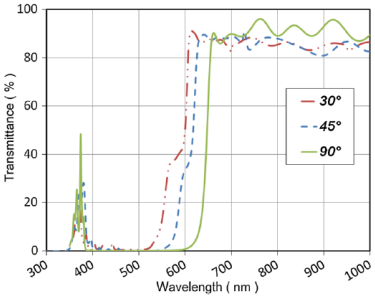

Figure II-14. Dichroic transmittance curve at different light incidence angle.

Table II-3. CPV spectra splitting SJ, DJ and TJ solar cell used.

	$\lambda_{cut\text{-}off}$ (nm)	H_{Si} (%)	$H_{III\text{-}V}$ (%)	H_{Tot} (%)
Si/SJ-InGaP	650	20	15.4	22.4
Si/DJ- InGaP/GaAs	900	20	31	30
Si/TJ- InGaP/GaAs/Ge	900–1130	20	40	36
TJ-InGaP/GaAs/Ge	—	—	40	32

Figure II-15 shown a module based on moderate optical concentration with a single dichroic mirror that directs the high energy light onto a GaInP/GaAs ‘‘mid-E’’ tandem cell and the low energy light onto a GaInAsP/GaInAs ‘‘low-E’’ tandem cell. This module is sensitive to photons with wavelengths lower than 1850 nm (Figure II-16) [15].

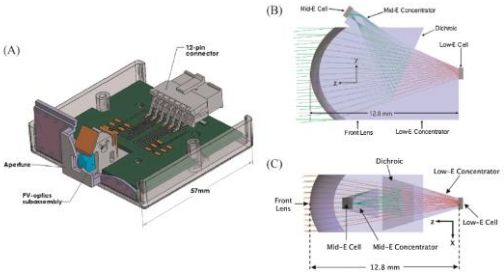

Figure II-15. CPV low concentrated with spectra separation on two DJSC.

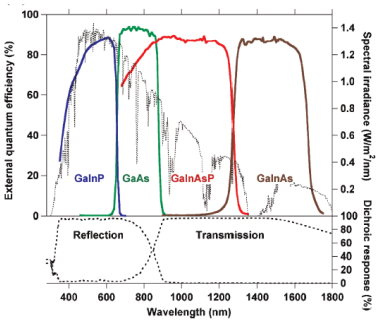

Figure II-16. EQE for the mid-E and low-E tandems cells.

Table II-4. CPV spectra splitting dual junction solar cell used.

Cell	V_{oc} (V)	I_{sc} (mA)	FF (%)	Efficiency (%)
GaInP	1.519	2.74	83.3	17.2
GaAs	1.059	2.36	82.8	10.3
GaInAsP	0.648	3.53	78.2	8.85
GaInAs	0.392	1.57	73.7	2.25
				SPE: 38.5 ± 1.9

Figure II-17 shown VHESC (Very High Efficiency Solar Cell) program where there is a lateral solar cell multiple junction solar cells, where the solar cell corresponding to each spectral band can be optimized independently from the others [38].

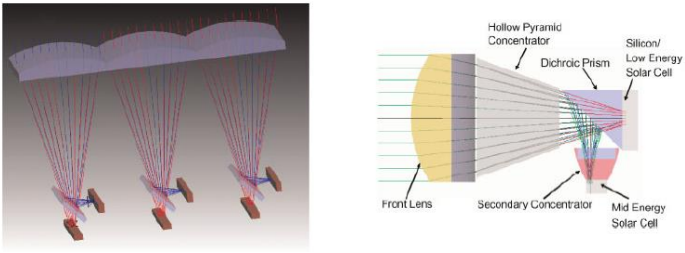

Figure II-17. Lateral spectrum-splitting concentrator [39].

Table II-5 describes the complete analysis of the components of the CPV system with lateral separation starting from single cells and subsequently with optical components. It is possible to note that the system efficiency of the module amounts to 39.5% [40].

Table II-5. Complete list of site-specific efficiency of CPV lateral spectrum splitting concentrator.

30·48X	Solar cell eff. (%)	Lens eff. (%)	Mirror eff. (%)	Optical eff. (%)	Sub-module eff. (%)
Mid-E					
Top	19·4	93·5	97·2	90·9	17·7
Bot	13·4	93·5	93·5	87·5	11·7
Low-E					
Top	8·9	91·5	97·1	88·8	7·9
Bot	2·6	91·5	92·5	84·6	2·2
Sum	**44·3**	92·9	95·9	**89·1**	**39·5**

The VHESC (Very High Efficiency Solar Cell) program has been further improved by using photovoltaic cells used in their optical band conversion. In particular in Figure II-18 are described the PV cells used, and the results are shown in

Table II-6 with a total efficiency equal to 42.7% and in Table II-7 with a total system efficiency equal to 43% [11].

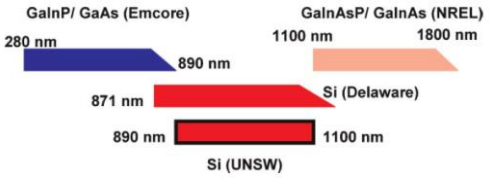

Figure II-18. Cells used in the improvement of the system of lateral splitting (VHESC program) [11].

Table II-6. Summary result of split spectrum cell result (Si Delaware) [11].

Cell	Supplier	Spectral range (nm)	Cell area (cm^2)	Irradiance (kW/m^2)	'Aperture' (cm^2)	Current density[a] (mA/cm^2)	Efficiency[b] (%)
GaInP/GaAs (two terminal stack)	Emcore	280–890	0.1245	24.2	3.0	27.6	**31.7**
Si	U Delaware	871–1200	0.158	8.67	1.4	11.7	**5.4**
GaInAsP/GaInAs	NREL	1100–4000	N/A	—	—	—	**5.6**
(three terminal stack)		1100–1350	N/A	40.1	N/A	7.8	3.7
GaInAsP GaInAs		~1350–1800	N/A	41.7	N/A	6.7	1.9
Five cell combination	—	—	—	—	—	**53.9**	**42.7 ± 2.5**

Table II-7. Summary result of split spectrum cell result (Si UNSW) [11].

Cell	Supplier	Spectral range (nm)	Cell area (cm^2)	Irradiance (kW/m^2)	Aperture (cm^2)	Current density (mA/cm^2)	Efficiency (%)
GaInP/GaAs (two terminal stack)	Emcore [4]	280–890	0.1245	24.2	3.0	27.6	**31.7**
Si	UNSW	890–1100	4.00	4.21	16.8	9.7	**5.7**
GaInAsP/GaInAs	NREL [4]	1100–4000	N/A	—	—	—	**5.6**
(three terminal stack)		1100–1350	N/A	40.1	N/A	7.8	3.7
GaInAsP GaInAs		~1350–1800	N/A	41.7	N/A	6.7	1.9
Five cell combination	—	—	—	—	—	**51.9**	**43.0 ± 1.9**

2.4 Solar optics concentrator

2.4.1 Primary optical element (POE) concentrator, reflection and refraction lens

The concentration photovoltaic systems are based on the use of reflection mirrors or refraction concentration lenses.
The most common POE is the refractive Fresnel lens, but there are many CPV companies using Cassegrain reflectors.
The Fresnel lens is usually made of polymethyl methacrylate (PMMA or acrylic) or silicon-on-glass (SOG).
The PMMA is easiest to realized, usually by embossing the lens elements onto a flat sheet of PMMA. Good mechanical tolerances can be achieved, and the process is fast, and scalable to high volume production.
A PMMA lens, though, suffers from surface and internal degradation and it is known to be susceptible to damage from mechanical cleaning and stain-causing airborne pollutants.

In SOG lens Fresnel lens are casting on one face of a glass sheet using a clear silicone gel. Silicone bonds well to glass, and the mechanical structures formed are at least as accurate as with PMMA, and the lens has a durable outside face of glass and does not suffer the degradation problems of PMMA [30].

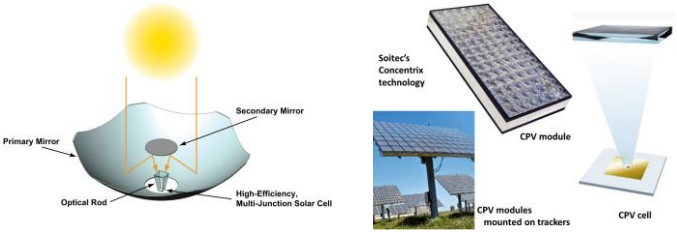

a) b)

Figure II-19. a) CPV reflection technology by Solfocus Inc., b) CPV refraction technology by Soitec.

In Figure II-20 and Figure II-21 are shown the optical transmission and reflection response of typical material used in optical concentrator system compared with solar spectrum AM 1.5.

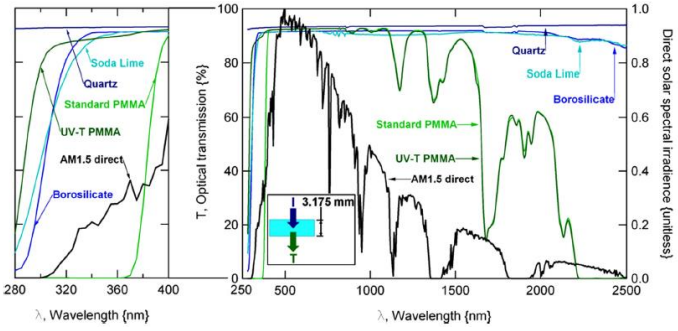

Figure II-20. Optical transmission material of CPV concentrator [41].

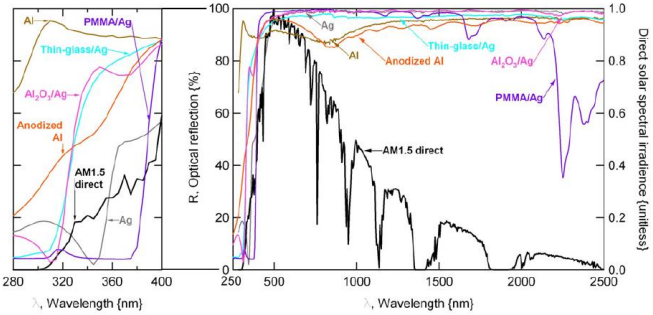

Figure II-21. Optical refraction material of CPV concentrator [42].

2.4.2 Secondary optics element (SOE)

In CPV systems it is very important the transportation efficiency of the solar radiation from the concentrating system to the photovoltaic cell. The optical design is based on optical components that help to homogenize and concentrate the solar radiation by limiting optical losses.
An important issue for CPV technology is the non-uniformity of the incident flux, which tends to cause hot spots, and the current mismatch reduces the overall efficiency of the system.
For this reason, secondary optic concentration element (SOE) is commonly used with the purpose of homogenizing the radiation on the photovoltaic cell. There are two types of homogenizers of light: reflection and refraction solar rod.

2.4.2.1 State of art

The aim of the optical system is to uniformly concentrate sunlight on the solar cell, but usually some portions of the solar cell are more exposed causing a non-uniform flux distribution on the solar cells. The presence of non-uniformity increases the temperature across some portions of the cells and causes hot spots that tend to damage significantly the cell performance.
Under concentration the solar cells produce larger amounts of currents, however this gets limited due to the losses caused by the increase of the series

resistance. As the concentration ratio of the system increases, it is more difficult to maintain uniformity of the incident flux on the solar cells [43] (Figure II-22).

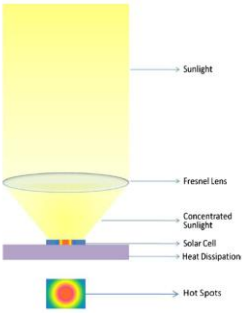

Figure II-22. Hot spot on solar cell by non-uniform illumination in CPV system.

In Figure II-23 is shown the CPV system with a primary concentrated Fresnel lens (POE) and a secondary refraction optical homogenizer (SOE) on PV cell. The optical efficiency of the system can be calculated for different angles of the incident rays, where for every incident angle an optical simulation is carried out forecasting the energy and distribution of the incident rays reaching the solar cells after the concentrating element [44].

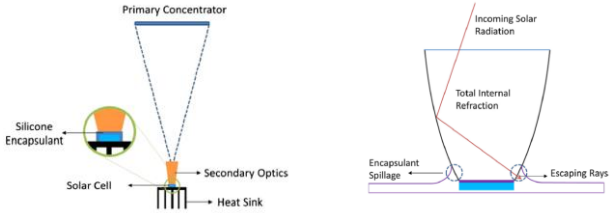

a) b)

Figure II-23. a) Scheme of Fresnel CPV system, b) SOE homogenizer on PV cell.

In Figure II-24 it is presented the design and results of optical efficiency by varing the angle of incidence on the secondary optics. It is also taken into account the optical loss between the coupling between the homogenizer and

the photovoltaic cell using an optical glue. To reduce optical losses a reflective film at the interface can further limit the optical losses.

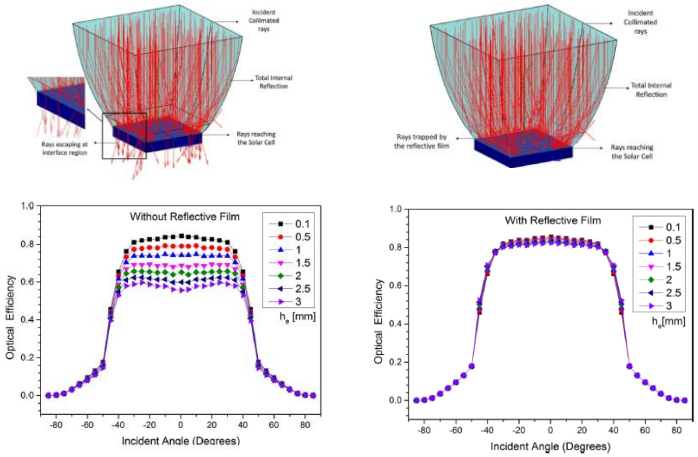

Figure II-24. a) Ray tracing design and optical efficiency result at different incident angle, b) ray tracing design and optical efficiency result at different incident angle with reflective film [44].

In Figure II-25 and in
Table II-8 described the ray tracing design of solar rod effect with different length H, on PV solar cell.

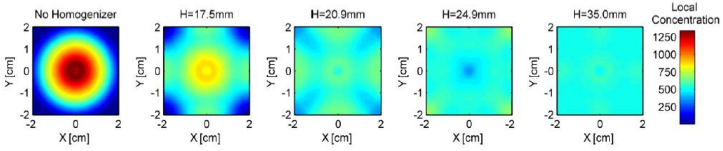

Figure II-25. Concentration map on the cell for different homogenizer length H [45].

Table II-8.Geometric and optical properties of solar rod as a function of length [45].

Homogenizer length (mm)	*0*	*17.5*	*20.9*	*24.9*	*35.0*
Aspect ratio	0	0.44	0.52	0.62	0.87
Average flux (W/cm^2)	44.9	44.9	44.4	44.9	43.2
Peak flux (W/cm^2)	109.9	72.4	53.3	57.8	47.2
Flux contrast	2367.2	69.3	1.88	1.98	1.19
Optical efficiency (%)	98.4	98.9	98.2	97.3	95.5

2.5 Optical multilayer filters

2.5.1 PVD Reactive Magnetron Sputtering technology

The PVD reactive magnetron sputtering technology is widely used to produce insulating dieletric thin film. The main drawbaks are due to the formation of arcing and instabilities and to the target poisoning by reactive gasses ghanging the physical and electrical character of the target itself.

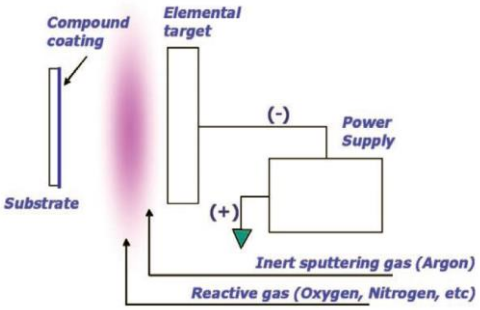

Figure II-26. Scheme of reactive sputtering [46].

The poisoning of the target swown in Figure II-26 change the voltage target parameter, the deposition rate decrease significantly and an increment of processing pressure occurs [47]. For insulating layers pulsed-dc and mid-frequency ac power is used to controntrol thereactive sputtering process, since

the reversal voltage applied to the cathod eliminates the charge build up on the target surface (Figure II-27).

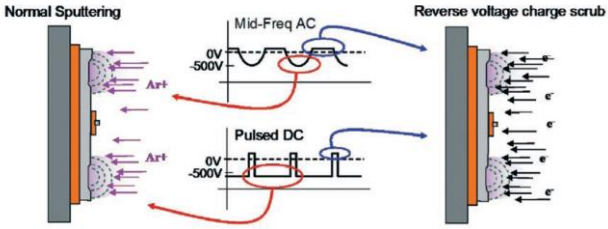

Figure II-27. Pulsed-DC and Mid-frequency Voltage reserval apply to the cathode [46].

The reserval voltage applied to the cathode drives an electron current to the target surface quenching charge build up on the insulating region during reactive sputtering. In this way, the voltage reversal is self-triggered and does not require an arc event in to dissipate charge buildup [48].
The reactive sputtering process control system is shown in Figure II-28 that explain the main devices control to create a poisoning of the target [49].

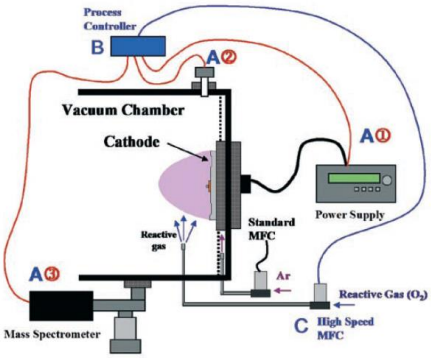

Figure II-28. Reactive sputtering system configuration.

The target poisoning is characterized by four distinct areas on the typical hysteresis curve that is shown in Figure II-29 [50]:

- Point 1 - the reactive gas is introduced but the reaction with the sputtering material it is prevented by the pumping system and the voltage, so the target remains in the metallic state;
- Point 2 - the gas pressure increases activating the reaction at the target surface; so the sputtering rate decreases when the surface of the target is covered by the reacted film;
- Point 3 - the poisoning of the target increase rapidly, and the partial pressure increase in the same time; the voltage of the target decreases, but some time it is possible to have an increase of the voltage target which depends on the material type;
- Point 4 – The target is covered with the reacted film and it is necessary to clean in order to go back at unpoisoned state;

The poisoned curve have a hysteresis effect related to the effect of gettering of the reactive gas on the target surface. The hysteresis effect can be limited by increasing the pumping speed [51].

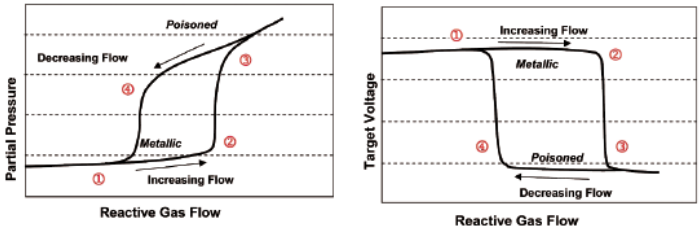

Figure II-29. The hysteresis reactive sputtering process of Al_2O_3 on the left and SiO_2 on the right.

2.5.2 Thin film optical material: State of art

The optical multilayers have to fulfill some specific properties such as transparency, roughness, homogeneity, and chemical stability.

For the optical coating, the most commonly used materials are TiO_2, SiO_2, Al_2O_3, Nb_2O_5, and MgF_2 [52].
Of particular interest is the realization of optical multilayer filters with silicon dioxide and titanium dioxide, linked to the low cost of materials.
The silicon dioxide material is more used in thevisibile spectrum for its lower index of refraction (around 1.46), its chemical stability and the phase stability during the deposition step. As regards TiO_2, it is used for the high refractive index, ranging from 2.3 to 2.7, which is depended on the phase polymorphism of the material. Thermal treatments of the deposited film are usually performed in order to control and stabilize the structure.
The Figure II-30 shown the X-Ray spectra of TiO_2 thin film phase evolution during annealing treatment. As can be observed, the phase changs completely from amorphous to anatase between 350 to 700°C, and to rutile at temperatures higher than 1100°C [26] [25].

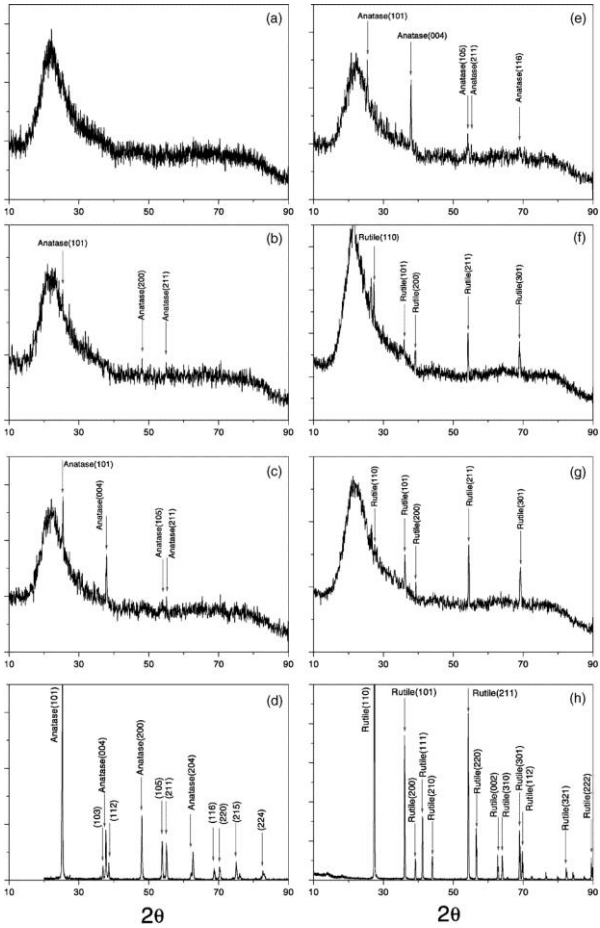

Figure II-30. X-Ray diffraction of TiO2 thi film annealed at different temperature: a) as-deposited, b) 300°C, c) 500°C, d) anatase, e) 700°C, f) 900°C, g) 1100°C, h) rutile.

The surface roughness also change with the annealing temperature and it is possible to verify that at 700°C it increases very quickly above the value of 5nm, due to a crystallization of the grains in the rutile phase [26].

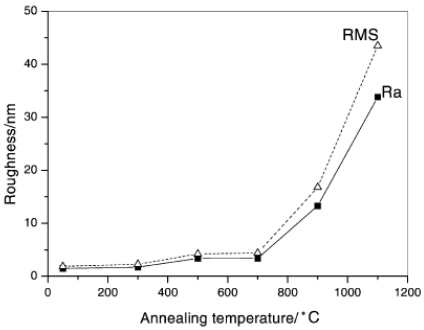

Figure II-31. Annealing temperature influence on TiO_2 thin film roughness.

The optical parameter change with annealing temperature too. In particular, the index of refraction n(λ) (Figure II-32) and the extinction coefficient k(λ)rises (Figure II-33) as the annealing temperature increases [53] [27].

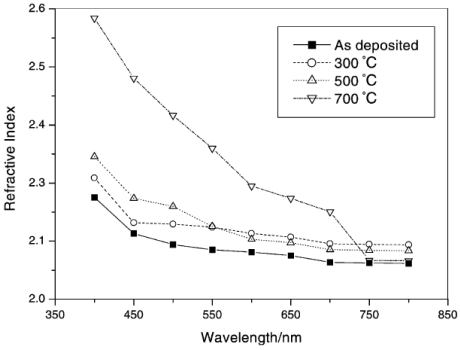

Figure II-32. Refractive index of TiO_2 thin film at different annealing temperature [26].

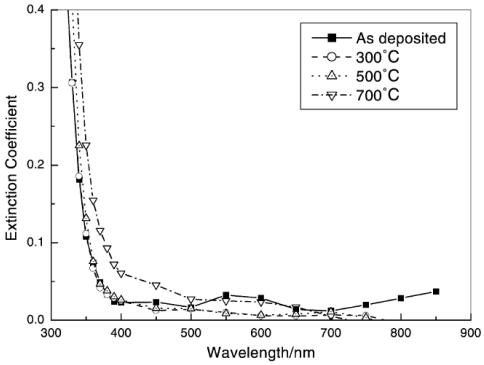

Figure II-33. Extinction coefficient of TiO_2 thin film at different annealing temperature [26].

Figure II-34 shows the optical transmittance variation of TiO_2 thin film with annealing treatment up to the temperature 600 °C, that corresponds the anatase phase.

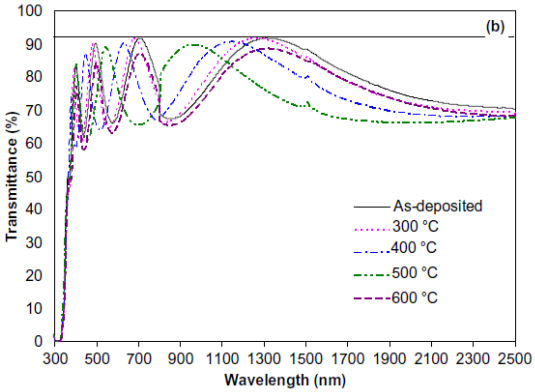

Figure II-34. Optical transmittance of TiO_2 thin film as deposited and annealing [54].

Figure II-35 shows the FT-IR analysis of TiO_2 thin film on silicon substrate as deposited after annealing at different temperatures. The plot shows the variation with the increasing annealing temperature of the peak at a 435cm^{-1} that corresponds to the phase anatase [24].

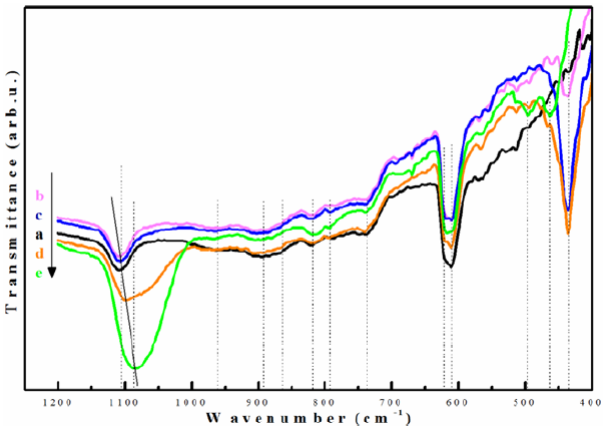

Figure II-35. FR-IR transmittance spectra of TiO2 thin film a) as deposited and annealed b) 400°C, c) 600°C, d) 800°C, e) 1000°C [22].

Chapter III

Experimental

3.1 Optical Filter Materials

3.1.1 Glass Corning Microsheet

The substrate selected for the dichroic filters is the Corning® glass Microsheet, a borosilicate glass with a thickness of 0.4mm which has high optical transparency (T > 90%) (Figure III-1) and a low thermal expansion ($\alpha = 73.8 \times 10^{-7}$ /°C).

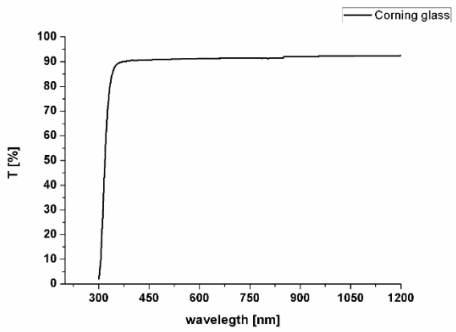

Figure III-1. Transmissionof Corning Microsheet glass.

This type of glass also has a high Abbe number (V_D = 65), high values of V_D indicating low dispersion material (Figure III-2).

$$V_D = \frac{n_D - 1}{n_F - n_C} \qquad 5)$$

The Abbe number is is characterized n_D, n_F and n_C, which are the refractive indexes at the Fraunhofer spectral lines (D = 589.3 nm, F = 486.1 nm and C = 656.3 nm).

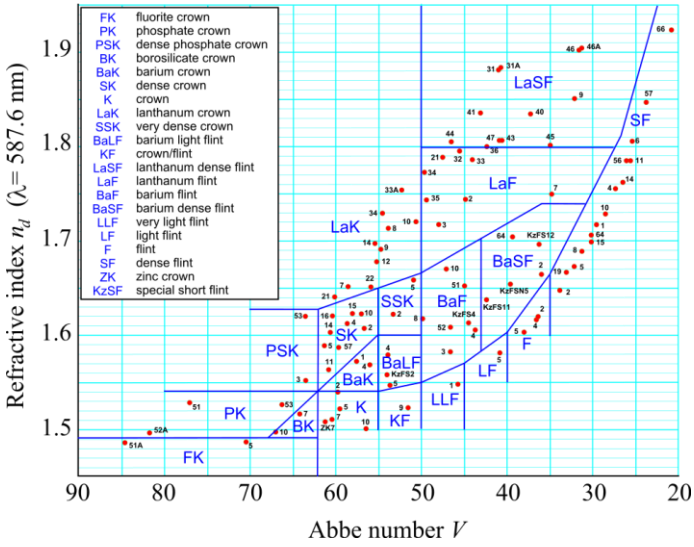

Figure III-2. Abbe diagram for several types of glass.

This Corning Microsheet glass is one of the most used in computing devices such as smartphones or tablets. The principal properties of Corning Microsheet glass used in this research are listed in Table III-1.

Table III-1. Technical datasheet of the Corning Microsheet glass.

Product Specifications	
Mechanical	**Metric**
Density	2.53g/cm^3
Young's Modulus	7.59 x 10^3 kg/mm^2
Poisson's Ratio	0.22
Shear Modulus	3.09 x 10^3 kg/mm^2
Knoop Hardness (KHN$_t$)	458
Viscosity	
Working Pt. (1 o~ poises)	1008°C
Softening Pt. (10$^{7.6}$ poises)	720°C
Annealing Pt. (1013 poises)	550°C
Strain Pt. (1014 poises)	508°C
Thermal	
Coefficient of Expansion (0-300°C)	73.8 x 10^{-7}/°C
(25°C to Set Point 513°C)	84.0 x 10^{-7}/°C
Thermal Conductivity, 0°C	$\frac{\text{cal cm}}{\text{sec cm}^2\,°\text{C}}$ .0023
Optical	
Refractive Index (589.3nm)	1.523
Transmission @ 420 nm	92%*
2200 nm	92%*
**Through a sample thickness of 1.0 mm*	
Electrical	
Log$_{10}$ Volume Resistivity @ 250°C	8.3 ohm-cm
@ 350°C	6.7 ohm-cm
Dielectric Constant @ 20°C; 1 MHz	6.7
Loss Tangent @ 20°C; 1 MHz	.46%

3.1.2 Fused Quartz

The Fused Quartz substrate used for the optical analysis on single layers of titanium dioxide has a thickness of 1mm, a high optical transparency (T > 93%) in the UV-VIS-NIR region, a low thermal expansion ($\alpha = 5.5 \times 10^{-7}$/°C); and a high Abbe number ($V_D = 67.2$).

Figure III-3 shows the optical transparency of fused quartz produced by Multi-lab (UK).

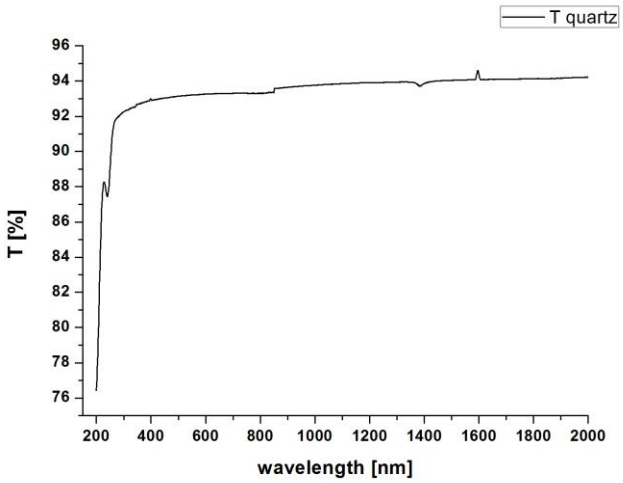

Figure III-3. Optical transmittance response of fused quartz.

The physical properties of fused quartz are listed in Table III-2.

Table III-2. Technical datasheet of fused quartz.

Hardness	5.5 - 6.5 Mohs' Scale 570 KHN 100
Design Tensile Strength	4.8×10^7 Pa (N/mm^3) (7000 psi)
Design Compressive Strength	Greater than 1.1×10^9 Pa (160.000 psi)
Bulk Modulus	3.7×10^{10} Pa (5.3×10^6 psi)
Rigidity Modulus	3.1×10^{10} Pa (4.5×10^6 psi)
Young's Modulus	7.2×10^{-10} Pa (10.5×10^6 psi)
Poisson's Ratio	0.17
Coefficient of Thermal Expansion	5.5×10^{-7}cm/cm °C (20 °C - 320 °C)
Thermal Conductivity	1.4 W/m °C
Specific Heat	670 J/kg °C
Softening Point	1683 °C
Annealing Point	1215 °C
Strain Point	1120 °C
Electrical Receptivity	7×10^7 ohm cm (350 °C)
Dielectric Properties (20 °C and 1 MHz)	
Constant	3.75
Strength	5×10^7 V/m
Loss Factor	Less than 4×10^{-4}
Dissipation Factor	Less than 1×10^{-4}
Velocity of Sound-Shear Wave	3.75×10^3 m/s
Velocity of Sound/Compression Wave	5.90×10^3 m/s
Sonic Attenuation	Less than 11 db/m MHz
Permeability Constants (cm^3 mm/cm^2 sec cm of Hg)	(700 °C)
Helium	210×10^{-10}
Hydrogen	21×10^{-10}
Deuterium	17×10^{-10}
Neon	9.5×10^{-17}
Chemical Stability (except hydrofluoric)	High resistance to water and acids

3.1.3 Sapphire

The Sapphire substrate used for the optical analysis on single layers of silicon dioxide, has a thickness of 0.43 mm an optical transparency (T > 85%) in the UV-VIS-NIR interval, a low thermal expansion (α = 8.4 x 10^{-6} /°C), and also has a high Abbe number (V_D = 67.2).
The Roditi International Corporation produced these products, and the Figure III-4 shows the optical property.

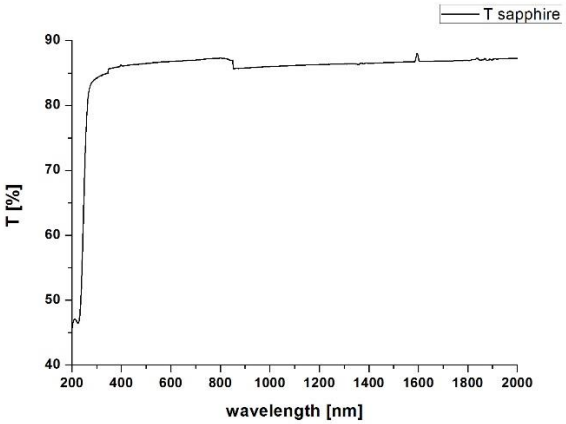

Figure III-4. Optical transmittance response of sapphire.

Table III-3. Technical datasheet of sapphire [55].

Material	**Czochralski grown sapphire (Al_2O_3 high purity > 99,995%)**	
Surface orientation	C-Plane (0001) surface orientation	
Dimension	Outer diameter	50.8mm ± 0.1mm, 76.2mm ± 0.25mm, 100.0mm ± 0.4mm, 150.0mm ± 0.5mm
	Thickness	500µm ± 10 µm, 430µm ± 10 µm, 330µm ± 15 µm
	Surface Flatness	< 25 µm
Density		3.98 g/cc
Hardness		1525 – 2000 Knoop, 9 mhos
Melting Point		2310 K (2040 °C)
Tensile Strength		275 MPa to 400 MPa
Young's Module, E		345 GPa
Thermal Conductivity	at 0° C	46.06 W/(m*K)
Thermal Expansion Coefficient	20° to 50° C	5.8 x 10^{-6}/°C
Density		3.98 g/cc

3.1.4 Carbon Plate

The glassy carbon substrate is used to analyze the thin film materials being in this case an amorphous material thus allows to highlight further the properties of the thin film material.
In the Rutherford Back Scattering analysis it is used for the low atomic number, that allows to separate the contributions of oxygen in the spectra of the coating materials. The carbon plate allows also to increase the resolution decreasing the noise in the acquired spectra. These carbon substrare are produced by SPI® Supplies (USA) (Figure III-5), and distributed in Italy by JEOL Italy.

Figure III-5. Carbon Plate substrate.

3.1.5 Silicon substate

Morphological analysis of the coating made with the atomic force microscope (AFM) have to be performed on the single layer of silicon dioxide and titanium dioxide, which have been deposited on silicon wafers from Bayville Chemical Supply Company Inc. (USA).
Such substrates have a surface roughness lower than 1nm and thus represent a good substrate for the analysis of roughness and thickness of the coatings.
Silicon wafers have the following characteristics: (100) orientation, n-Type, phosphorus doped, resistivity of 10 ohm*cm, one side chemical-mechanical polished, back side polished with diamond, 100 mm diameter, 380 μm thickness.

3.2 Concentrated Photovoltaic System (CPV) Materials

3.2.1 Glass N-BK7

The secondary optical component, shown in Figure III-6, selected to realize prototype CPV spectra splitting system [56] in this research activity is made with N-BK7 glass and in called “solar rod”. This type of material has a very good transparency throughout the visible range (Figure III-6), and a good optical clarity with index of refraction equal to 1.51 and hight Abbe Number (V_D = 64).

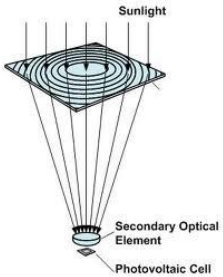

Figure III-6. Secondary optical component - solar rod.

Table III-4. Technical datasheet of N-BK7 [56].

Transmission Range	350nm to 2.5µm
Refractive Index	1.51680 @ 587.5618nm (Yellow Helium Line)
Reflection Loss	8.1% at 587.5618nm (2 surfaces)
Absorption Coefficient	--
Reststrahlen Peak	--
dn/dT	See Schott™ Table
$dn/d\mu = 0$	--
Density	2.51
Melting Point	557°C (Transformation Temperature)
Thermal Conductivity	1.114 W m^{-1} K^{-1}
Thermal Expansion	7.1 x 10^{-6} K^{-1}
Hardness	Knoop 610
Specific Heat Capacity	858 J Kg^{-1} K^{-1}
Dielectric Constant	n/a
Youngs Modulus (E)	82 GPa
Shear Modulus (G)	n/a
Bulk Modulus (K)	34 GPa
Elastic Coefficients	n/a
Apparent Elastic Limit	63.5MPa (9206psi)
Poisson Ratio	0.206
Solubility	Insoluble in water
Molecular Weight	n/a
Class/Structure	Amorphous glass

3.2.2 Poly-methylmethacrylate (PMMA)

The CPV system is composed by a primary optical concentrator which is a refractive type of a Fresnel lens. This particular lens allows to focus the light on two semi-planar surfaces. Due the particular geometry and the simplicity of production correlated to a lower cost of production, this concentrator lens is selected and integrated in the prototype CPV spectra splitting.

The PMMA material have good traspently throughout to the visible optical band (Figure III-7), good clarity (Figure III-8), Abbe number (V_D = 57), index of refraction (n =1.49) similar to the glass. This material have excellent

mechanical stability to shocks or traction, it is easy to print and polish, but it is brittle and has a poor heat resistance.

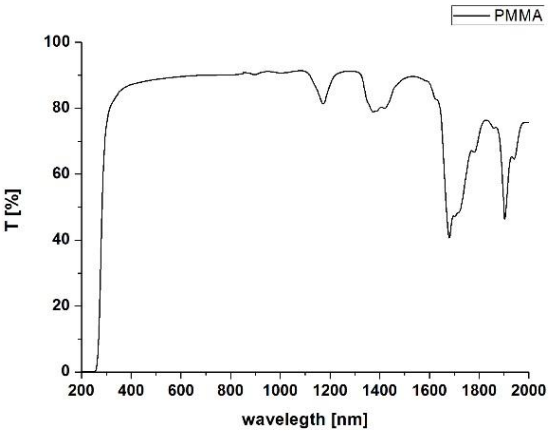

Figure III-7. Optical transmission of PMMA.

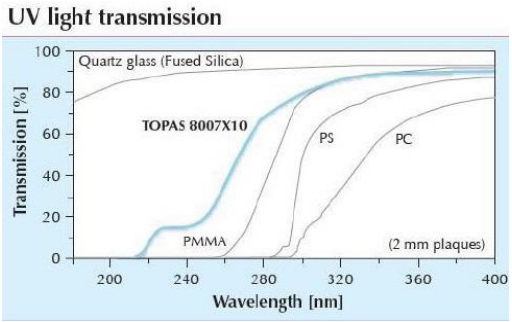

Figure III-8. Optical transmittance of common used polymer material.

Table III-5. Technical datasheet optical polyer material.

	Units	TOPAS (5013LS-01)	PC	PMMA
Total light transmittivity	(%)	91.2	87-89	91-92
Refractive Index	-	1.533	1.59	1.49
Abbe No.	-	56	30-31	57-58

3.2.3 Gallium Arsenide CPV cell

In concentrated photovoltaic (CPV) splitting system it is used a cell of gallium arsenide (GaAs) by company CESI Ricerche (Milano-Italy) with a size of 10*10mm^2. These cells have a high performance spectral response (SR) in the optical band 350 <λ< 850nm.

The external quantum efficiency (EQE) of GaAs cell presents very high values, equal to 0.8 in the optical visible band (Figure III-9) with an efficiency at standard condition 25°C and 1000 W/m^2 equal to η_{GaAs}= 19.1%.

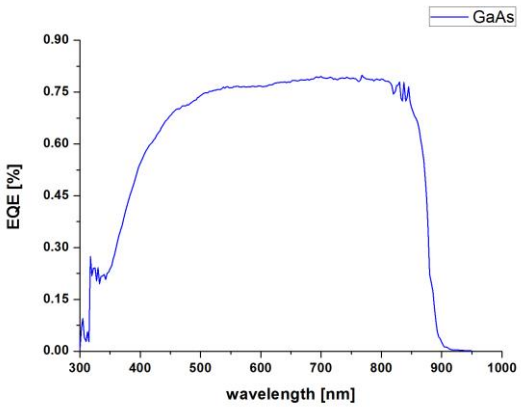

Figure III-9. EQE of Gallium Arsenide CPV cells.

3.2.4 Silicon CPV cell

In the CPV prototype spectral separation system it is coupled in the optical band transmitted by the dichroic filter a CPV Silicon (Si) cell for high concentrations with an area of 10 x 10mm^2 provided by NAREC (UK). This cell has quantum efficiency (EQE >0.9) (Figure III-10). The maximum spectral response at the wavelength λ = 900nm is shown in the Figure III-11. This cell have an efficiency at standard condition 25°C and 1000 W/m^2 equal to η_{Si} = 16.5%.

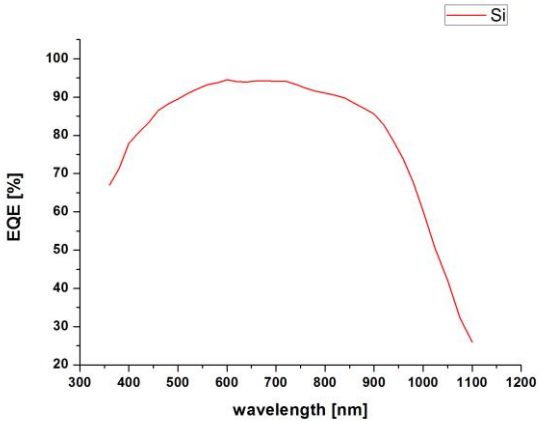

Figure III-10. EQE of Silicon CPV cells.

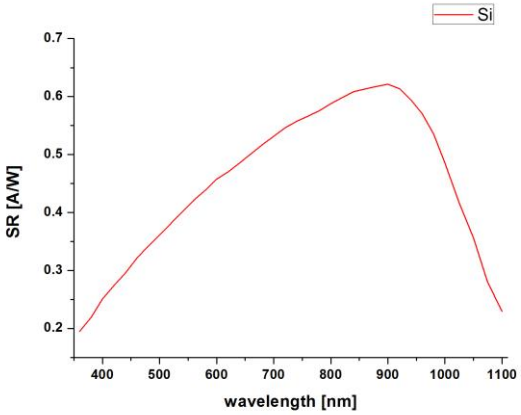

Figure III-11. Spectral Response of Silicon CPV cells.

3.2.5 Optical glue

The optical coupling in the prototype system CPV is achieved by an adhesive optical epoxy incurred by UV in the range 350<λ<400= nm.
This coupling ensures lower optical losses between the sun rod and the photovoltaic cell allowing the radiation to be focused more effectively over the exposed area of the cell.
The optical glue allows also a protection of the sensitive component of the system or the photovoltaic CPV cell by environmental factors such as dust [57] and humidity, which may compromise the functioning and the efficiency of the cell itself (Figure III-12). We used a Photo Electronics 400 UV with 400-Watt high-pressure metal halide lamp with iron and cobalt additives to realize the curing of optical glue.

Figure III-12. Optical glue material between sun-rod and CPV cell.

3.3 Optical multilayer thin film

3.3.1 Optical design of dichroic filter

The design of the multilayer is of fundamental importance. Here we describe the main steps underlying the design of the dichroic filters used for the spectral separation of the sun spectrum.

3.3.1.1 Substrate slab material

For the design of an optical multilayer film the first step is a description of the substrate to be coated, which in this case is a borosilicate glass high transparency. The glass selected is first analyzed to extrapolate its optical characteristics.
The spectrophotometric measurements reveal properties of transmittance and reflectance in a selected optical band that in this application are analized wavelength range between 350 and 1200 nm realize by Jasco570 UV-VIS-NIR spectrophotometer.
The transmittance and reflectance spectra, are used to extrapolate the optical parameters using analytical functions.
The substrates materials have a high thickness and therefore with a partial absorption of the impringing light (Figure III-13).

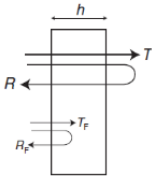

Figure III-13. Partially absorbing radiation by slab substrate.

The algebraic analysis [58] allows to obtain the values of refractive index n(λ) and extinction coefficient k(λ) [59].
Assuming that part of the radiation is absorbed by the material, the refractive index has the complex expression:

$$\tilde{n} = n - ik \qquad 6)$$

Using the experimental value R and T of reflectance and transmittance, R_F and T_F can be calculated taking into account that:

$$T_F = R_F - 1 \tag{7}$$

It is derived from the solution from a polynomial equation of the second order.

$$R_F = \Big(2 + T^2 - (1-R)^2 - \{[2 + T^2 - (1-R)^2]^2 - 4R(2-R)\}^{1/2}\Big)\big(2(2-R)\big)^{-1} \tag{8}$$

The final equations for refraction index and extinction are.

$$k(R,T) = \frac{\lambda}{4\pi h} ln\left[\frac{R_F(R,T)T}{R - R_F(R,T)}\right] \tag{9}$$

$$n_{\pm}(R,T) = \frac{1 + R_F(R,T)}{1 - R_F(R,T)} \pm \left\{\frac{4R_F(R,T)}{[1 - R_F(R,T)]^2} - \left(\frac{\lambda}{4\pi h}\right)^2 ln^2\left[\frac{R_F(R,T)T}{R - R_F(R,T)}\right]\right\}^{1/2} \tag{10}$$

The calculated constants are used for the modeling of the multilayer by means of the software Tf_Calc or FilmStar.

3.3.1.2 Design of optical single layer thin film

The numerical analysis for transmittance and reflectance of the deposited thin films [60] allows to evaluate the optical constants of the deposited by the PVD Reactive Magnetron Sputtering technology [61].
The two materials used as optical coatings are described with two different analytical expressions [62]:

- The titanium dioxide is deposited on quartz substrates, and analyzed with a Sellmeier 1 functions for the index of refraction and an exponential function for the extinction coefficient.

$$n(\lambda) = \sqrt{A_0 + \frac{A_1 \lambda^2}{\lambda^2 - A_2}} \quad 11)$$

$$k(\lambda) = B_1 * exp(B_2 \lambda^{-1}) \quad 12)$$

- The silicon dioxide is deposited on substrates of sapphire and analyzed with a Cauchy function for the refractive index and an exponential for the extinction coefficient.

$$n(\lambda) = A_0 + \frac{A_1}{\lambda_1^2} + \frac{A_1}{\lambda_2^4} \quad 13)$$

$$k(\lambda) = B_1 * exp(B_2 \lambda^{-1}) \quad 14)$$

The dispersion functions were used to fit the experimental curves using an iterative process of calculation. This allows to convergence with a gap between the optical experimental curves and the optical simulations around 1%.

3.3.1.3 Design of multilayer thin film

The optical design of thin film multilayer focuses on a specific objective to be achieved which is called ideal target. It is shown in Figure III-14.

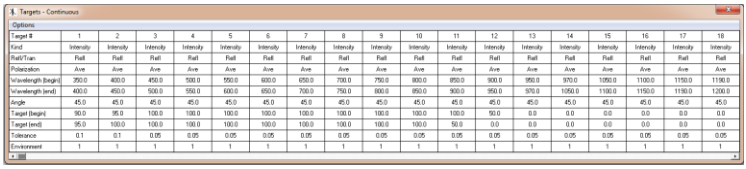

Target #	1	2	3	4	5	6	7	8	9	10	11	12	13	14	15	16	17	18
Kind	Intensity	Intensity	Intensity	Intensity	Intensity	Intensity	Intensity	Intensity	Intensity	Intensity	Intensity	Intensity	Intensity	Intensity	Intensity	Intensity	Intensity	Intensity
Refl/Tran	Refl	Refl	Refl	Refl	Refl	Refl	Refl	Refl	Refl	Refl	Refl	Refl	Refl	Refl	Refl	Refl	Refl	Refl
Polarization	Ave	Ave	Ave	Ave	Ave	Ave	Ave	Ave	Ave	Ave	Ave	Ave	Ave	Ave	Ave	Ave	Ave	Ave
Wavelength (begin)	350.0	400.0	450.0	500.0	550.0	600.0	650.0	700.0	750.0	800.0	850.0	900.0	950.0	970.0	1050.0	1100.0	1150.0	1190.0
Wavelength (end)	400.0	450.0	500.0	550.0	600.0	650.0	700.0	750.0	800.0	850.0	900.0	950.0	970.0	1050.0	1100.0	1150.0	1190.0	1200.0
Angle	45.0	45.0	45.0	45.0	45.0	45.0	45.0	45.0	45.0	45.0	45.0	45.0	45.0	45.0	45.0	45.0	45.0	45.0
Target (begin)	90.0	95.0	100.0	100.0	100.0	100.0	100.0	100.0	100.0	100.0	100.0	50.0	0.0	0.0	0.0	0.0	0.0	0.0
Target (end)	95.0	100.0	100.0	100.0	100.0	100.0	100.0	100.0	100.0	100.0	50.0	0.0	0.0	0.0	0.0	0.0	0.0	0.0
Tolerance	0.1	0.1	0.05	0.05	0.05	0.05	0.05	0.05	0.05	0.05	0.05	0.05	0.05	0.05	0.05	0.05	0.05	0.05
Environment	1	1	1	1	1	1	1	1	1	1	1	1	1	1	1	1	1	1

Figure III-14. Optical multilayer design target Tf_Calc Software [63].

The target project can be described in different ways: discrete, continuous or cone angle.

The continuous target was chosen to design the optical multilayer thin film is. In this case, the dichroic filter is a edge-type filter that must reflect or transmit precise wavelengths and the transition between the two optical bands must take place in a gradual manner.

This transition can occur within very sharp optical bands and the difficulty in the design of such filters (Figure III-15). Is to have a good transition while maintaining relatively high efficiency in the optical bands.

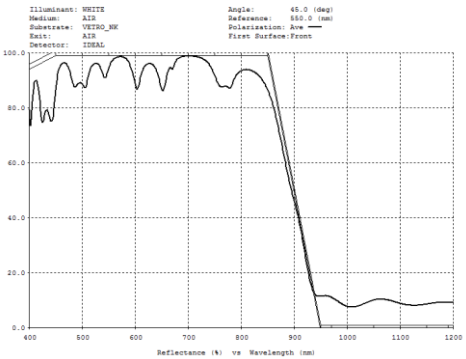

Figure III-15. Edge filter design with project target.

3.3.1.4 Optimization of multilayer thin film

The process of optimization of the optical design is based on an iterative process (Figure III-16).

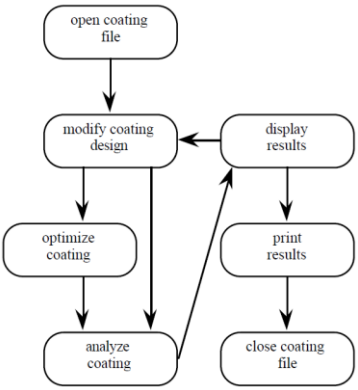

Figure III-16. Interactive process of Optical multilayer design [64].

In the first step, a manual stacking of alternating layers of TiO_2 and SiO_2 is provide by the operator. This method allows to gradually insert a layer at a time or a group of layer [65]. In this way, there is the possibility to optimize, according to the project target, the optical response of the multilayer filter by limiting the number of layers (Figure III-17) [66].
The optimization of the optical design using modeling software TF_Calc may occurs following three different procedures: manual, constrained or automatic.

- Manual: in this mode a couple of layers is inseted step by step with the last layer with the with high refractive index material: in this way it is possible to increase the reflectivity of the system [67].
- Constrained: in this mode the boundary conditions maximum and minimum thickness of the layers, or the maximum thickness of the whole multilayer; this approach allows to fix the thickness range in order to optimize deposition time.
- Automatic: in this mode the software selects the number needed to obtain the best possible convergence.

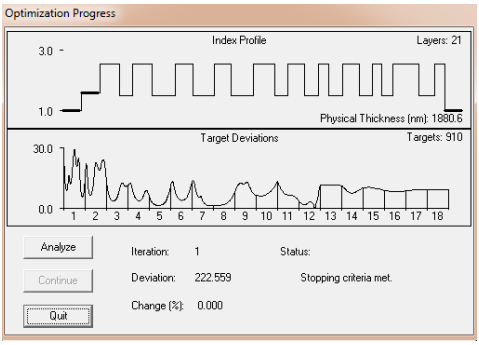

Figure III-17. Optimization process of Optical multilayer design.

In this research we selected the constrained simulation mode, in order to proceed at a later stage of realization of the filter and the optimization of the deposition. This procedure is necessary for developing an industrial coating system and at the same time for providing good results maintaining low realization times.

3.3.2 Production of optical thin film

3.3.2.1 PVD (Physical Vapor Deposition)

PVD (physical vapor deposition) has become in recent years a method of producing thin films increasingly affirmed in the field of both research and industry.
This process takes place at the atomic level, that is, it achieves the film growth atom by atom on the substrate.
The physical vapor deposition allows the creation of films characterized by good purity and it can be applied both to metal materials and to dielectric materials.
The PVD process takes place in a vacuum about 10^{-3} mbar and consists of three distinct phases:

1 Formation of the species in the vapor phase
2 Vapor phase transport from the source to the substrate
3 Condensation of the vapor on the substrate and subsequent growth

There are two major philosophies in the PVD process. The first is the thermal evaporation, the second is sputtering. In the first method, the heating of the material causes the material evaporation. In the second method, the vaporization occurs through the collision between the atoms of the target surface and ionized particles.
In this thesis we selected the methodology of the physical deposition processes by sputtering.
The sputtering deposition consists in the emission of particles (atoms, ions, clusters) from the target due to the impact of ions and electrons generated in the plasma region and accelerated by an electric field.
The amount of emitted matter, "sputtering yield", depends on many variables including:

- Mass and energy of the incident ions;
- Gas pressure in the deposition chamber;
- Temperature of target and substrate;
- Angle of incidence

3.3.2.2 PVD Reactive Magnetron sputtering

Thin film single layers were deposited by a reactive sputtering prototype system (Figure III-18). This prototype was designed and realized in collaboration with the Institute of Nuclear Physics INFN-LNL of Legnaro-Padua.

Figure III-18. Prototype of PVD reactive magnetron sputtering system.

In PVD Reactive Magnetron Sputtering, the sputtering of a metallic material, titanium or silicon and occurs during the poisoning in the vapor phase with oxygen released into the chamber.
In Figure III-19 has been an example used for the calibration of the titanium oxide is shown. Different powers are used, in our case the power is equal to 1.410 KW with respect to 1.0 kW reported in literature, but the trend of the poisoning of the target is similar.

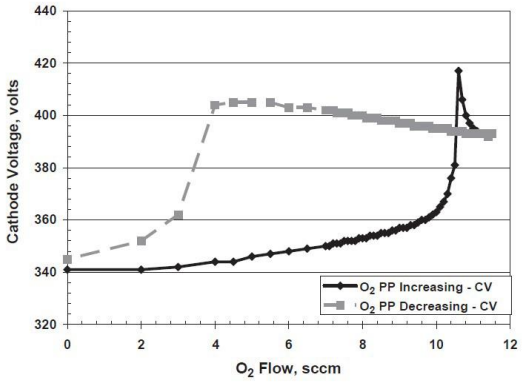

Figure III-19. Trend of titanium target d.d.p. as function of the oxygen flow at 1.0KW power [51].

The PVD magnetron reactive sputtering technique permits to control the deposition voltage. By using the voltage control of the target it is possible to regulate the reactant gas flow through mass flow controllers or piezo-valves, obtaining the poisoning curve of the material target [50] [46] (Figure III-20).

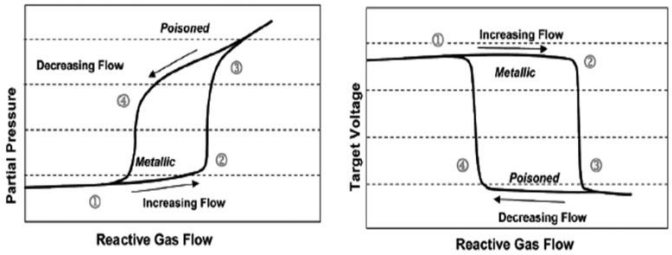

Figure III-20. Reactive gas partial pressure and silicon target voltage versus oxygen reactive gas [46].

3.3.3 Characterization of optical thin film

3.3.3.1 AFM analysis

The assessment of the rate of deposition was carried out with the morphology analysis of the titanium dioxide and silicon dioxide thin film by AFM technique (atom force microscope) DME Dual Scope 98-50.

Figure III-21. AFM - DME Dual Scope 98-50.

By the AFM measurements was also possible to measure the quadratic and algebraic surface roughness [68] of the deposited coating and the thickness of the individual layers used as calibration samples of the deposition plant.
The algebrical roughness R_a is the average value of the whole area

$$R_a = \frac{1}{P}\sum_{j=1}^{N}\sum_{i=1}^{M}|\eta(i,j)| \qquad 15)$$

where P is the number of points of the entire scanned area A, N and M are points of the coordinates x and y, and η is equal to:

$$\eta(z,y) = \left[I(x,y) - \left[\frac{1}{P} \sum_{j=1}^{N} \sum_{i=1}^{M} I(i,j) | (i,j) \in A \right] | x = 1, \dots, M; y = 1, \dots N; (x,y) \in A \right] \quad 16)$$

P the number of the tops of the whole area.
The quadratic roughness R_q is the Root Mean Square (RMS) of all the points of the area to the square divided by the number of points.

$$X_{RMS} = \sqrt{\frac{1}{n} \sum_{i=1}^{n} x_i^2} = \sqrt{\frac{x_1^2 + x_2^2 + \cdots + x_{1n}^2}{n}} \quad 17)$$

$$R_q = \sqrt{\frac{1}{P \sum_{j=1}^{N} \sum_{i=1}^{M} \eta^2(i,j)}} \quad 18)$$

3.3.4 Optical measurement

3.3.4.1 UV-VIS-NIR spectroscopy analysis

Optical spectra of thin film films and slab materials were recorded with a Jasco570 UV-Vis-NIR spectrophotometer, within a wavelength range of 250-2000 nm.

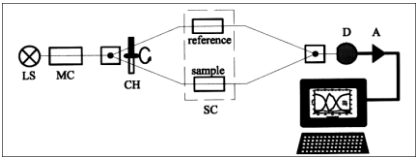

Figure III-22. Functional diagram of a spectrophotometer.

With the spectrophotometer instrument is possible to analyze the transmittance and absorbance, related to the transmittance for the Beer-Lambert law. The reflectance was analyze with a highly reflective reference.

3.3.4.2 Fourier transform infrared spectroscopy (FTIR) analysis

The FT-IR analysis of thin film coating material on a slab substrate were carried out by a FT-IR spectrometer Jasco FT-IR 660 Plus equipped with beam splitter Ge coated KBr substrates as standard and working in vacuum.
A scanning range from 1500 to 350 cm^{-1} is used.

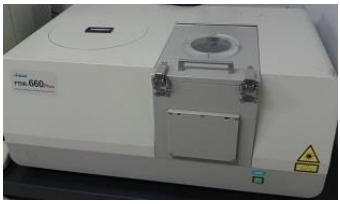

Figure III-23. FT-IR spectrometer Jasco FT-IR 660 Plus.

3.3.5 Rutherford Back Scattering analysis (RBS)

Rutherford back scattering is applied to investigate the atomic composition of the uppermost layers of matter. A beam with high-energy ions, in the order of MeV, impinge the sample surface and part of them is backscattered. BAckscattered ions are characterized by an energy due to the elastic collisions with the taget nuclei and to inelastic collision with the electrons.
The acceleration system used in the measurements is a Van de Graaf AN2000 HVEC (Figure III-24) with a maximum acceleration voltage of 2.4 MV at the National Laboratories of Legnaro National Institute of Nuclear Physics (LNL-INFN).

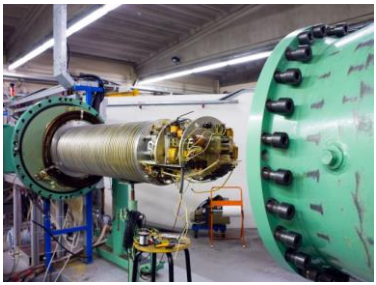

Figure III-24. Van de Graaf AN2000 accelerator at LNL-INFN Legnaro-Padua.

Using RBS technique can obtain different information:

- analyzing the back-scattering energy of the ions the surface chemical species can be identifying;
- the quantitative analysis can be obtained through the scattering cross section;
- concentration profile are reconstructed by analyzing energy loss of the projectile penetrating into the target.

3.3.6 Scannig Electron Microscope analysis

Scanning electron microscopy (SEM) technique was used to evaluate the multilayer coatings on silicon. The SEM analysis were carried out with a Vega3 LM Tescan scanning electron microscope (Figure III-25). The maximum voltage used reaches 30 kV with a resolution of 3 nm with secondary electrons (SE) and back scattered electron (BSE), and a Tungsten heated cathode.

Figure III-25. Vega3 LM Tescan scanning electron microscope.

3.3.7 Heat treatment analysis

Thermal treatments were with a Lenton furnaces tube that allows to reach up a maximum temperature of 1300°C.
Thin film samples were treated at atmospheric pressure into an alumina pipe at 350°C for 1h,12h and 24h (Figure III-26).
The ramp temperature for the thermal cycle used is as follows:

- Heating ramp to 350 ° C in 3 hours (2 ° C / min)
- Stationing heat at 350 ° C for 1h, 12h or 24 hours
- Ramp cooling 350 ° C in 5 hours (1.2 ° C / min)

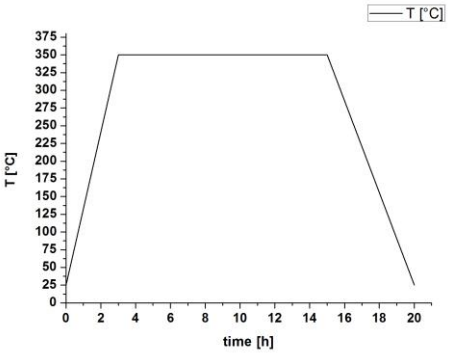

Figure III-26. Heat treatment cycle on thin film samples.

3.3.8 X-Ray diffraction analysys

Titanium dioxide sampleswere analyzed with the X-Ray diffraction technique to compare the results obtained with the FT-IR analysis.
The analyses were done before and after heat treatment in order to evaluate the structural phase using a hight resolution Philips X'PERT™ PRO MRD Diffractometer (at the Cu $K\alpha_1$ =1.54184 Å wavelength).

3.4 Design of prototype CPV spectra splitting system

3.4.1 Preliminary stages of optical design

The optical design of the concentrating photovoltaic system with the spectral separation was realized with Zemax software in order to apply the dichroic filters to a concentrating photovoltaic system with optimized geometric.
In particular, it has been selected a concentration system using a refractive Fresnel lens. This type of concentration presents simple constructive characteristics and manufacturing low costs.

In particular, the Fresnel lens is easily applicable in concentrated photovoltaic systems, limiting the alignment optics error than the reflection concentration systems.

3.4.2 Design of a CPV system with Fresnel lens

The concentrating photovoltaic system has the peculiarity to focus the incoming solar radiation on a PV cell (Figure III-27).
The prototype CPV consists of:

- Optical concentrator
- CPV receiver
- Spectral separator

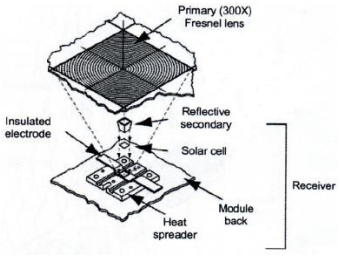

Figure III-27. Components of a CPV commercial system.

3.4.2.1 Optical Concentrator

A first distinction can be made by analyzing the type of optics used in the concentrator. The concentration optics is essentially divided into two strands, the "imaging optics" (IO) which arise conventional image forming optical, and the "non-imaging optics" (NIO) [10] [69] founded in 1975 by R. Wilson and based on light transport and not on image formation.

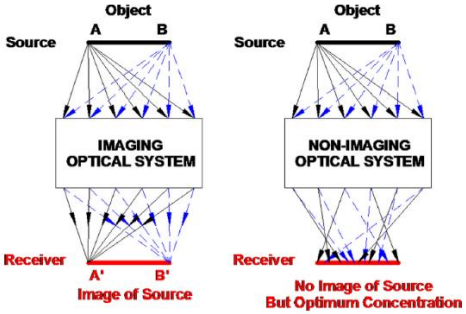

Figure III-28. Imaging and non-imaging optical system [41].

The IO systems are almost exclusively of paraxial type, because components are placed in proximity to or on the optical axis of the system and their dimensions are such that the rays have a small angle with respect the optical axis. The loss of these conditions brings a system IO with large aberrations, and the concentrator determines a reduction in the efficiency of the optical system.

The primary optics concentrator is a Fresnel lens [70] designed using the constant pitch mode, where the distance between the ring is kept constant while the depth of the same ring is kept constant (Figure III-29).

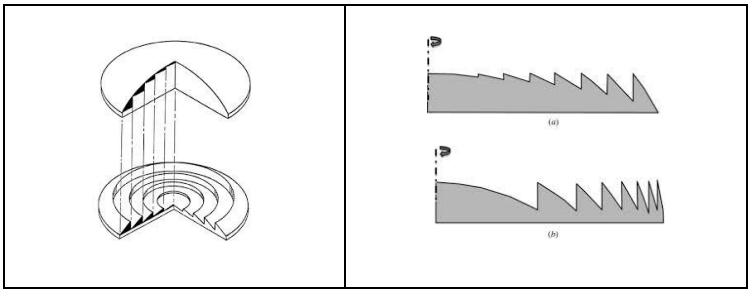

Figure III-29. Fresnel lens design a) constant pitch, b) constant depth.

In the design stage of the lens we studied the effect of different lenses with equal effective diameter but with different effective focal length (EFL). This process allowed us to analyze the optical response of the lens varying the f/number and at the same time it was possible to analyze the efficiency of the total optical system.

3.4.2.2 CPV Receiver

The receiver system is composed of the photovoltaic cell and the electronic circuit with insulating material made of alumina from Aurel Automation S.p.a. technology.
In the photovoltaic receiver there is also the secondary optical homogenization that is required to collect all the focused radiation from the primary concentration system. The secondary optic is made of N-BK7 from Silo S.r.l. with the geometry of a truncated pyramid with square base, where the geometry allows an internal total reflection at interfaces equal to the maximum of three times [71] [72].
The secondary optics has it's the main aim to uniform the solar radiation flow on the receiver [72], and to increase the angular tolerance, by directing light rays which have too high divergence.
The secondary optics is aligned with the PV receiver through the optical epoxy glue. (Figure III-30)

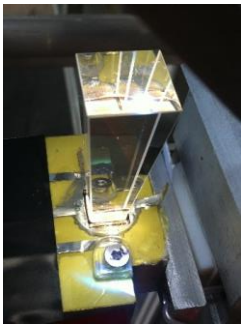

Figure III-30. CPV receiver and solar rod.

3.4.2.3 Spectral separator

The spectral separator is the technological heart of the prototype CPV system. It is designed to include the Fresnel lens, the dichroic filter and the two single junction solar cells (SJSC).
The spectral separator and consists of a support to accommodate the dichroic filter at an angle equal to 45°, that of the design angle of the optical multilayer, and two berths in order to submit in the two optical band the solar receivers.

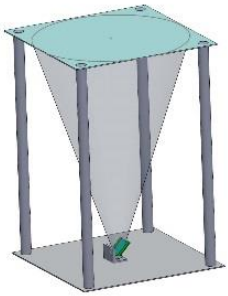

Figure III-31. Design of CPV system with spectral separator.

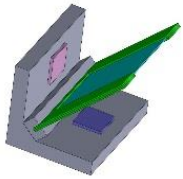

Figure III-32. Design of spectral separator system.

3.5 Characterization of CPV spectra splitting system

3.5.1 Indoor I-V-P characteristic curve

Photovoltaic cells and CPV system spectral separation without optical concentration used are characterized by using a solar simulator of Abet Technology Air Mass 1.5 (ASTM 927-91) with a maximum power of 2000 W/m^2 (Figure III-33).

Figure III-33. Indoor photovoltaic characterization system.

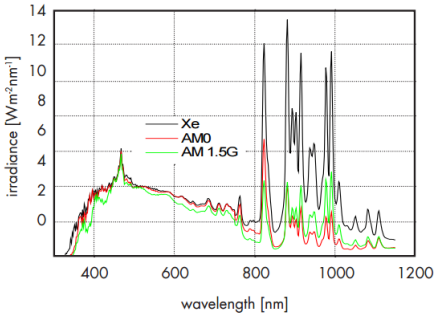

Figure III-34. Spectra Solar simulator AM O, AM 1.5 G.

The acquisition system for the electrical characterization is composed of a photo radiometer Delta Ohm HD2102-02 with a probe for the irradiance measurement of LP 471 RA acquiring the radiation of the solar simulator. It was necessary to calibrate the position of the cell in a reference to a standard of 1000 W/m^2 and 25°C [73], Keithley 2400 source meter analyzer was used to measure the current across the cell with the four-point measuring technique and the data were processed with ReRa tracer software.

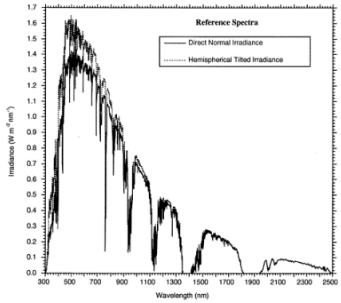

Figure III-35. Direct Normal Spectral Irradiance (Solid Line) and Hemispherical Spectral Irradiance on 37° Tilted Sun-Facing Surface [73].

Table III-6. Data sheet of measurement probe LP 471 RAD.

Sonda di misura dell'IRRADIAMENTO LP 471 RAD completa di modulo SICRAM in linea con lo strumento

Campo di misura (W/m^2):	0.1·10^{-3}... 999.9·10^{-3}	1.000...19.999	20.00...199.99	200.0...1999.9
Risoluzione (W/m^2):	0.1·10^{-3}	0.001	0.01	0.1

Campo spettrale:	400nm... 1050nm
Incertezza di calibrazione:	<5%
f_2 (risposta come legge del coseno):	<6%
f_3 (linearità):	<1%
f_4 (errore sulla lettura dello strumento):	±1digit
f_5 (fatica):	<0.5%
Deriva ad un anno:	<1%
Temperatura di lavoro:	0...50°C

Curva di risposta tipica

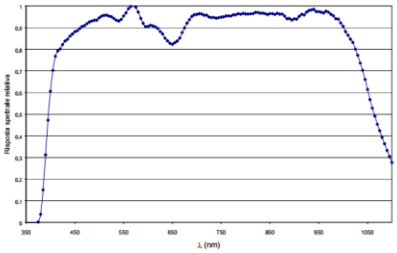

3.5.2 Outdoor I-V-P characteristic curve

The outdoor characterization of the photovoltaic system CPV is conducted with experimental measurements.
The solar rays are to a good approximation parallel to each other with an angular divergence equal to 0.27°. It is therefore necessary to use a solar tracking system to be able to maintain the orthogonality between the plane of the Fresnel lens and the sunlight. The sunlight angular divergence can be calculated as follows:

$$\theta = arcsin\left({}^{R}/_{D}\right) = 0.266° \qquad 19)$$

where R is the radius of the sun (6.9599 x 10^8 m) and D is distance of the sun from the earth (1.505 x 10^{11} m).
The electrical characterization of the CPV system to measure the I-V curves is obtained by the solar module analyzer, ISOTEC ISM 490 which measure the current with the four tips method.

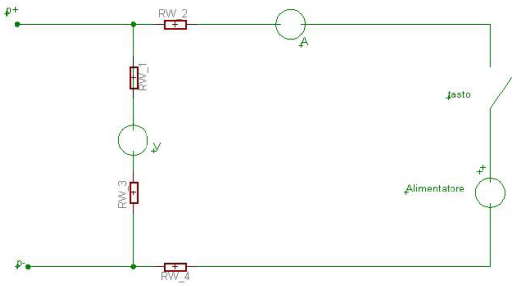

Figure III-36. Circuit for the measurement of the I-V characteristic curve with four using a programmable power supply as a load.

3.5.3 Solar radiation analysis

The prototype system CPV requires a tracking system in order to be axially aligned with the sun's rays [74]. CPV systems in contrast to the traditional PV work only with the direct normal irradiance (DNI). In order to align the concentration optics it is necessary to use a solar tracking system, and in the specific case has been used a pointing system with bi-axial drivers motors for the tracker of the AKKUtrack ™. This device also allows you to measure the irradiance (W/m^2) of the sun and acquire it during the day [75]. This is fundamental parameter to determine the CPV prototype system efficiency.

Table III-7. Data sheet of AKKUtrack™ solar tracking system [76]

AKKUtrack™	
Field of view	4.5°x2.9° (H xV)
Resolution	0.01°
Relative Accuracy	± 0.01°
Sampling Rate	60 frames/s
Data logging Rate	From 4/hour to 20/minute
Environmental Protection Class	IP 55
DNI Range	50 to 1500 W/m^2
Response Time	< 0.1s
Accuracy	± 20 W/m^2
Operating Temperature Range	-25°C to +85°C
Temperature dependence on sensitivity (-20°C to 50°C)	< 10%
RoHS Compliance	Yes

Figure III-37. AKKUtrack™ solar tracking systems.

3.5.4 Thermal analysis

The photovoltaic cell is the most delicate component in the CPV system.
The effect of temperature affects very much the photovoltaic conversion efficiency [77]. In order to assess the operation temperature with the optical concentration a system of heat dissipation of the solar receiver has to be designed [78].
We carried out a thermal study of the cells with experimental outdoor measurements under concentration. The photovoltaic cell was simulated by a known material, in this case aluminum. It was evaluated surface temperature using a thermal imager camera FLIR I7® of IRCON Overloar with an emissivity value equal to $\varepsilon = 0.93$. Also was assessed the temperature within the sample with a K thermocouple and a digital multimeter of Fluke® 179.

Chapter IV

Results and Discussion

Part of this chapter has been published in:

W. Raniero, G. Maggioni, G. Della Mea, M. Campostrini, S. Marigo, and M. Nardo
Rutherford backscattering spectrometry (RBS) analysis of dichroic systems for optical application.
AIP Publishing, AIP Conference Proceedings 1530, Vol. 133 (2013).

W. Raniero, M. Campostrini, G. Maggioni, G. Della Mea, A. Quaranta
Physical vapor deposition reactive magnetron sputtering for the production and application of dichroics in photovoltaic system with solar spectral splitting
Elsevier, Applied Surface Science, Vol. 308, pp. 170–175 (2014).

W. Raniero, G. Della Mea, M. Campostrini
Functionalization of surfaces with optical coatings produced by PVD magnetron sputtering
IGI-Global, in press (2015).

4.1 Multilayer optical filters

4.1.1 PVD Reactive Magnetron Sputtering process

The multilayers are made with the PVD technique Reactive Magnetron Sputtering are fixed on a rotating sample holder (Figure IV-1) that allows realizing several samples in the same time. In the outer part of the sample holder there is a shutter which alternately, with a rotation concentric to the sample holder is placed in front of the metal target surface (titanium or silicon).

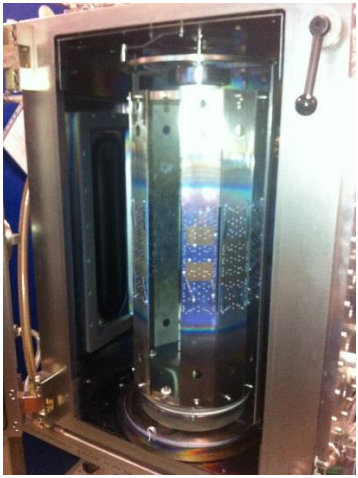

Figure IV-1. Prototype rotating sample holder.

Single layers of titanium dioxide are deposited by DC method while the samples of silicon dioxide is deposited by DC-pulsed method.
Table IV-1 [79] shows the deposition parameters used for the realization of thin films of TiO_2 and SiO_2.

Table IV-1. Deposition parameter of SiO_2 and TiO_2 [79].

	TiO_2	SiO_2
Power (W)	DC - 1410	DC pulsed -1480
Voltage (V)	468 ± 0.4	370 ± 0.5
Current (A)	3 ± 0.01	4 ± 0.01
Vacuum limit (mbar)	2.8×10^{-6}	2.8×10^{-6}
O_2 flow (sccm)	11 ± 0.5	28 ± 0.5
O_2 partial pressure (mbar)	3.25×10^{-3}	3.30×10^{-3}
Ar flow (sccm)	30 ± 0.2	30 ± 0.2
Ar partial pressure (mbar)	3.18×10^{-3}	3.18×10^{-3}
Deposition rate (nm/min)	3.40 ± 0.10	11.40 ± 0.34

4.1.2 Optical characterization of the substrates

4.1.2.1 Corning glass Microsheet substrate

The Glass substrate of Corning Microsheet used for the realization of optical multilayers are analyzed with a spectrophotometric analysis to obtain the reflectance and transmittance optical response (Figure IV-2).

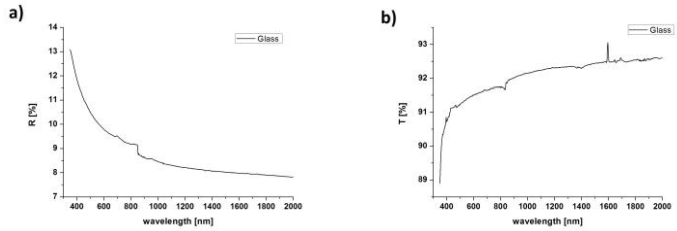

Figure IV-2. a) Corning Glass Refractance, b) Corning Glass Transmittance.

From the experimental data (Equation 5, 6) the curves of the refractive index (n) and the extinction coefficient (k) of Corning Glass Figure IV-3 and were obtained.

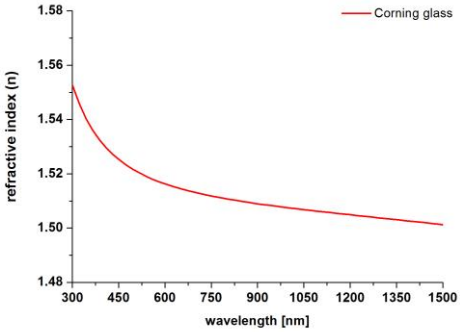

Figure IV-3. Refractive index of Corning Glass.

4.1.2.2 Quartz substrate

The Quartz substrate used for to analyze the TiO_2 thin film are analyzed with a spectrophotometric method to obtain the reflectance and transmittance optical response (Figure IV-4).

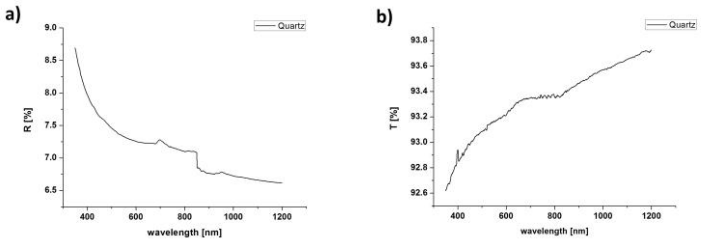

Figure IV-4. a) Quartz Refractance, b) Quartz Transmittance.

Optical experimental data were processed in order to octain refractive index (n) and the extinction coefficient (k) of Quartz (Figure IV-5).

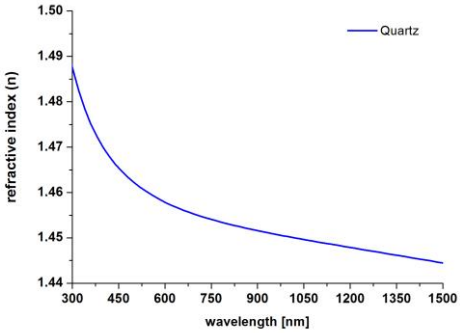

Figure IV-5. Refractive index of Quartz.

4.1.2.3 Sapphire substrate

The Sapphire substrate used for to analyze SiO_2 thin film was analyzed by a spectrophotometric analysis in order to obtain the reflectance and transmittance optical response (Figure IV-6).

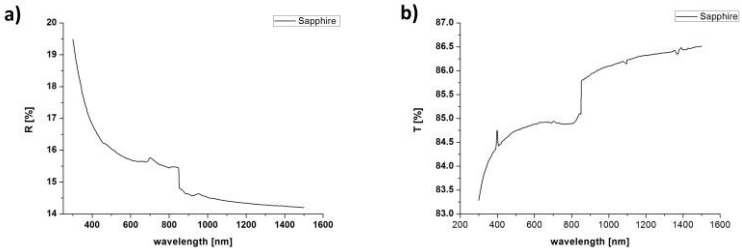

Figure IV-6 a) Sapphire Refractance, b) Sapphire Transmittance

Using the experimental data we derived the curves of the refractive index (n) and the extinction coefficient (k) of Sapphire substrate (Figure IV-7).

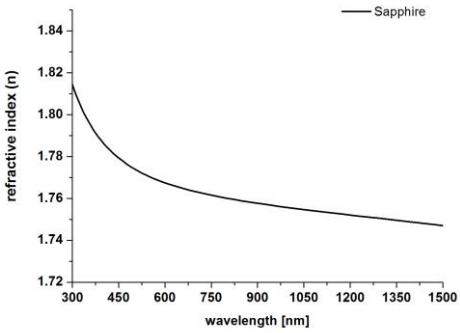

Figure IV-7. Refractive index of Sapphire.

4.1.2.4 Comparison of the substrates optical parameters

In Figure IV-8 it is possible to compare the refractive index calculated from experimental measurements on the substrates. These values are used for the design of optical multilayers.

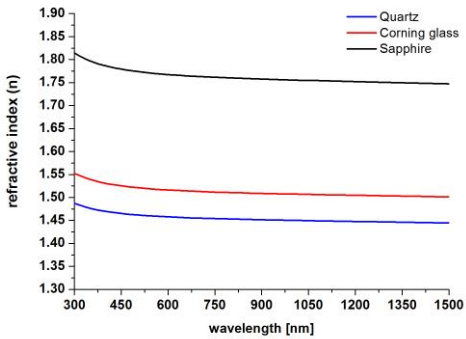

Figure IV-8. Refractive index of glass, quartz and sapphire.

The extinction coefficient curves of the optical substrates used. It is possible to note that these materials have a very high performance in the optical range of the visible since the extinction coefficient is in the order of 10^{-6}-10^{-7}, and then negligible.

4.1.3 Optical characterization of single layer thin film

4.1.3.1 Optical analysis of TiO_2

The single layers of TiO_2 deposited on substrates of quartz are analyzed by spectrophotometric analysis. The optical responses of transmittance and reflectance are quantified as a function of the thickness of the coating (Figure IV-9).

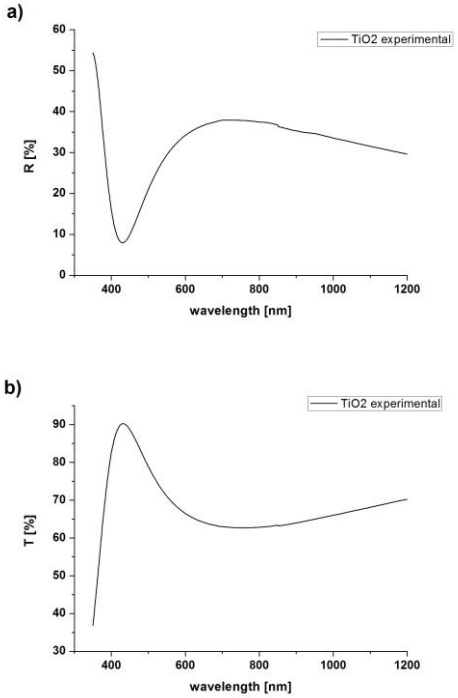

Figure IV-9. Experimental TiO_2 thin film: a) Refractance, b) Trasmittance

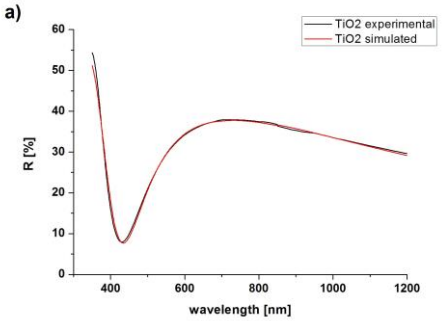

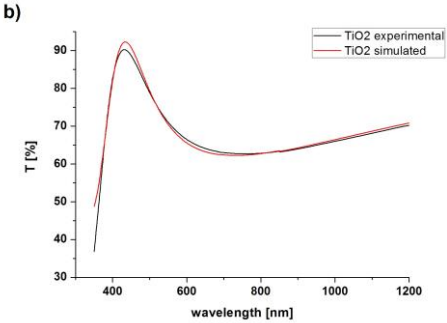

Figure IV-10. Experimental and simulated TiO_2 thin film: a) Refractance, b) Trasmittance

Table IV-2. Fitting simulation of TiO_2 material by Tf_Calc software.

TiO_2 tickness	**79.3nm ± 1.2 nm**	
$n(\lambda) = \sqrt{A_0 + \frac{A_1\lambda^2}{\lambda^2 - A_2}}$	A0	4.67
	A1	1.13
	A2	1.04e-1
$k(\lambda) = B_1 * exp(B_2\lambda^{-1})$	B1	0.13e-2
	B2	5.87

The analysis of the experimental optical measurements allowed to extrapolate, by using the dispersion functions, the values of refractive index n (λ) and the extinction coeffcient k (λ) of theTiO_2 material [80].

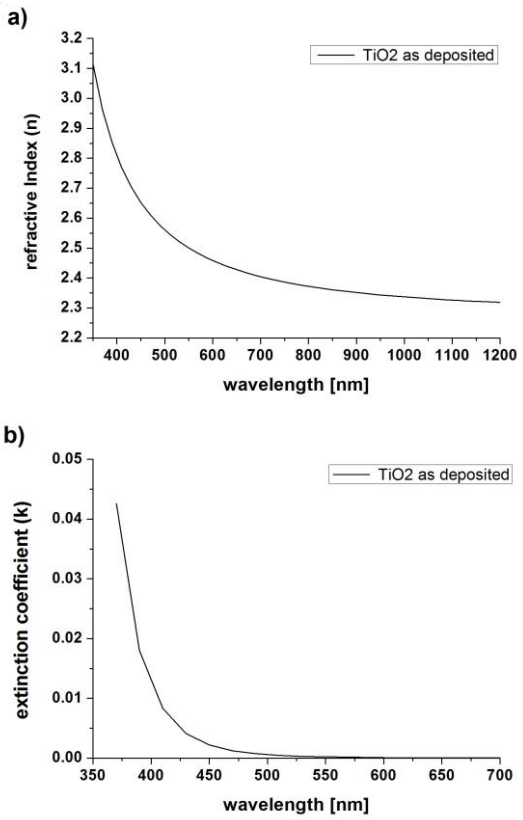

Figure IV-11. TiO_2 coating: a) Refractive index n(λ), b) Extintion coefficient k(λ).

4.1.3.2 Optical analysis of SiO_2

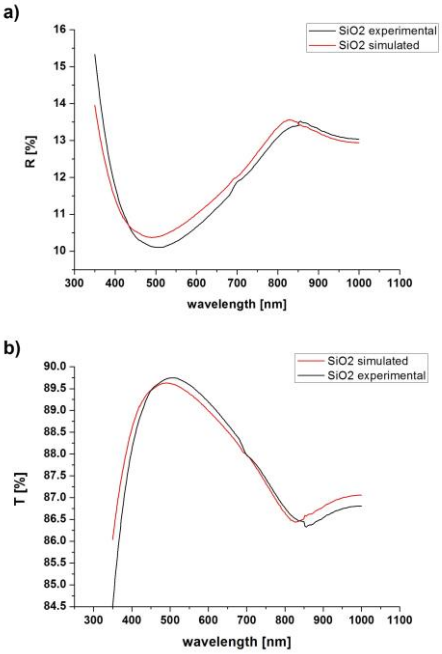

Figure IV-12. Experimental and simulated SiO_2 thin film: a) Refractance, b) Trasmittance

Table IV-3. Fitting simulation of SiO_2 material by Tf_Calc software.

SiO_2 thickness	79.2nm ± 2.4 nm	
$n(\lambda) = A_0 + \frac{A_1}{\lambda^2} + \frac{A_2}{\lambda^4}$	A0	1.40
	A1	4.40e-2
	A2	-3.23e-3
$k(\lambda) = B_1 * exp(B_2\lambda^{-1})$	B1	1.50e-3
	B2	-2.70e-1

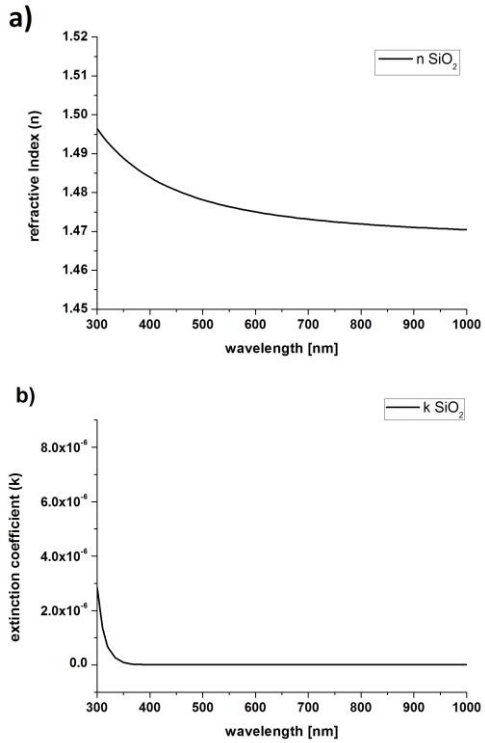

Figure IV-13. SiO_2 coating: a) Refractive index n(λ), b) Extintion coefficient k(λ).

4.1.4 Morphological characterization of thin film coating

The thin films of titanium dioxide and silicon dioxide are deposited on silicon substrates with low roughness <1nm. The coatings are analyzed by atomic force microscopy (AFM) to determine the thickness and the surface roughness.

4.1.4.1 Thickness analysis

AFM measurements on individual layers allow to accurately determine the values of thickness deposited by PVD Reactive Magnetron Sputtering technology.
In particular, the determination of the thickness allows to the deposition rate.
The scanned area is 47x47 μm^2 with a scanning speed of 10 μm/s.

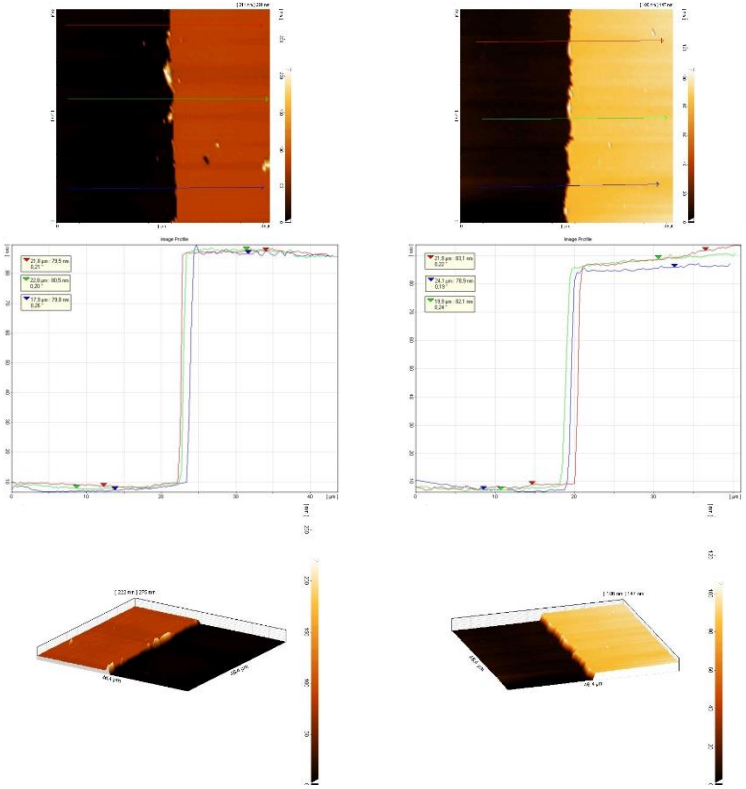

a) b)

Figure IV-14. AFM measure 2D- 3D and profile thickness thin film: a)TiO_2 , b)SiO_2

Table IV-4. AFM measurements of reference samples of SiO_2 and TiO_2.

Material	Time [s]	Thickness [nm]	Dev. Stand [nm]	Error [%]
SiO_2	535	99.4	± 3.9	3.9
SiO_2	420	79.3	± 4.5	4.4
SiO_2	420	79.5	± 2.0	2.5
SiO_2	415	79.3	± 2.4	2.9
TiO_2	599	28.5	± 0.8	2.9
TiO_2	1433	80.6	± 3.9	4.8
TiO_2	1433	79.7	± 1.1	1.3
TiO_2	1433	79.3	± 1.2	1.5

Table IV-5. Rate Deposition of SiO_2 and TiO_2.

Material	Rate Deposition [nm/min]
TiO_2	3.4 ± 0.1
SiO_2	11.4 ± 0.3

AFM measurements were also conducted on optical multilayers to compare the thickness of the project with the real deposited thickness. This measure allows to check the reliability of deposition rate of the PVD deposition system (
Table IV-6).

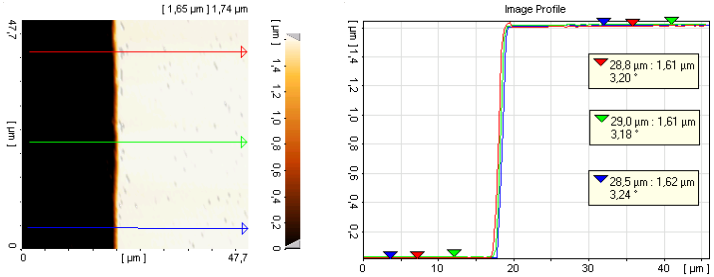

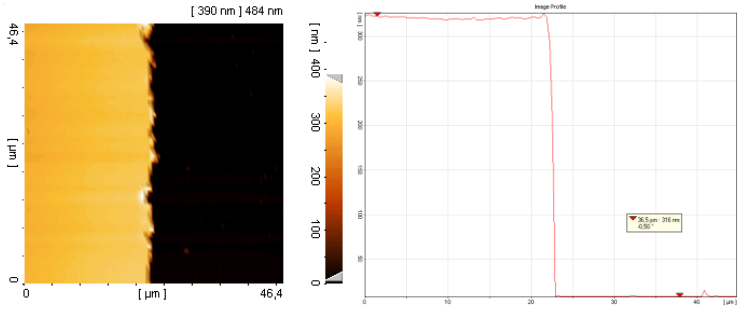

Figure IV-15. AFM measurements of a multilayer dichroic.

Table IV-6. AFM multilayer measure designed and deposited.

	Thickness [nm]
Multilayer dichroic designed	1604
Multilayer dichroic deposited	1610

4.1.4.2 Roughness analysis

The surface AFM microscopy analysis was used also ro evaluate the surface roughness of the deposited coating. This value allows to improve the surface quality obtained with the sputtering process [23] [22].

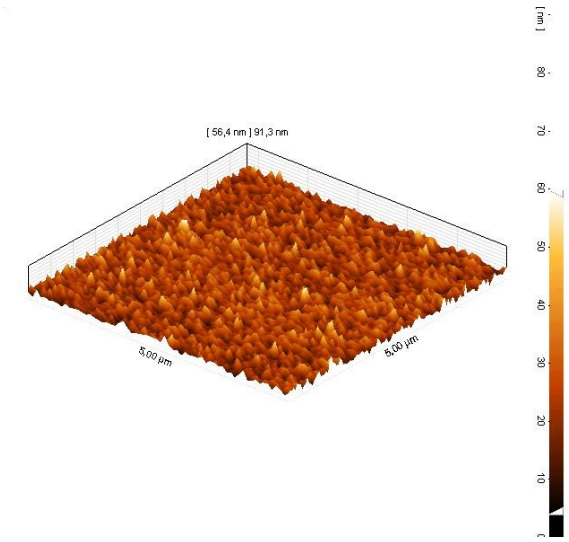

Figure IV-16. AFM roughness morphology of TiO_2 coating.

Table IV-7. Roughness value of TiO_2 thin film.

Material	Ra [nm]	Rq [nm]	Thickness [nm]
TiO_2	2.9 ± 0.2	3.9 ± 0.2	185.0 ± 8.3

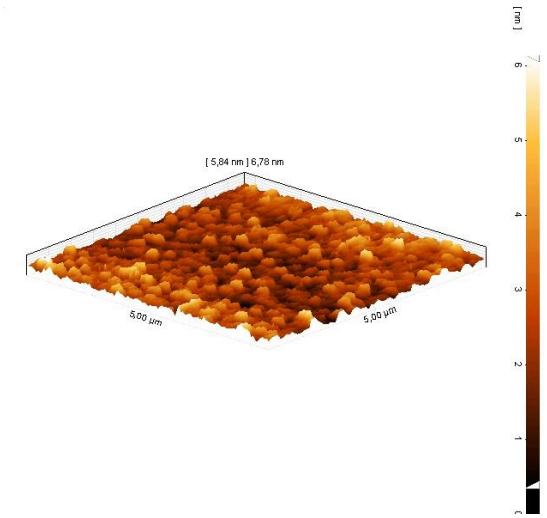

Figure IV-17. AFM roughness morphology of SiO_2 coating.

Table IV-8. Roughness value of SiO_2 thin film.

Material	Ra [nm]	Rq [nm]	Thickness [nm]
SiO_2	1.7 ± 0.1	2.1 ± 0.1	47.3 ± 2.4

4.1.5 Compositional characterization of thin film

4.1.5.1 Rutherford Backscattering (RBS) analysis

The single layer thin films are deposited on substrates of silicon or amorphous carbon. For Rutherford backscattering spectroscopy analysis, in order to quantify their composition.
Such a technique has an accuracy of 1.5 – 2.5% from the analysis of the spectra.

The substrates on which the films of TiO_2 and SiO_2 are deposited allow to distinguish the signal of all the elements.
In Figure IV-18 it is shown the difference in the acquired spectrum of a thin film on a substrate of silicon or amorphous carbon.

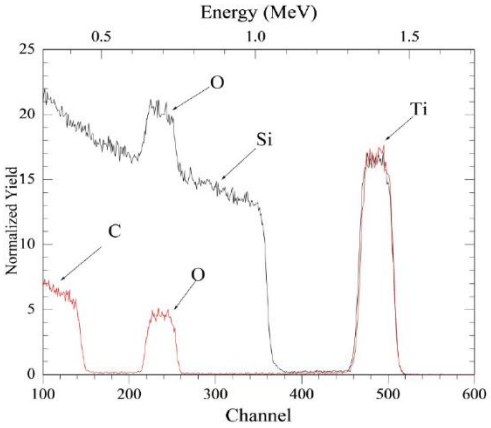

Figure IV-18. RBS spectra of TiO_2 on silicon or carbon plate.

The carbon substrate enables to separate the peaks contribution relating to the single elements of titanium and oxygen. Moreover, it reduces the noise in the bottom of the spectrum, and allows to quantify each individual element.

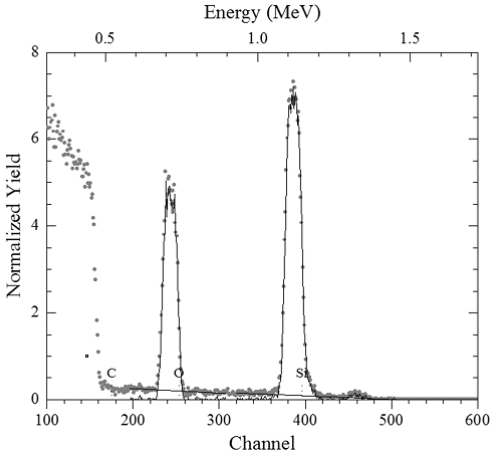

Figure IV-19. RBS spectra of SiO_2 thin film.

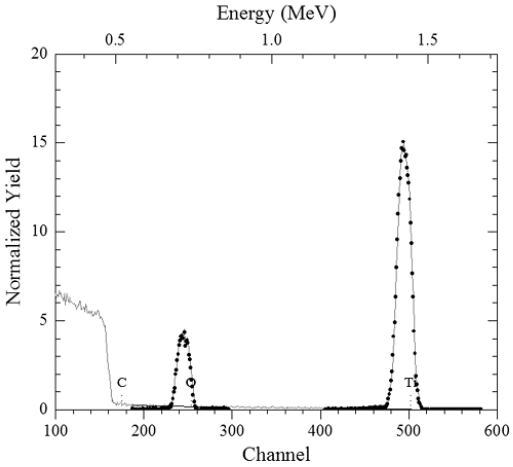

Figure IV-20. RBS spectra of TiO_2 thin film.

RBS analysis gives the stoichiometric ratio O/Ti and O/Si, therefore different samples were made with different voltage deposition in order to calibrate the reactive deposition process.
The deposition process is based on the retroactive control of the voltage applied to the cathode. The oxygen flow is controlled by a mass flow changing the concentration along the poisoning hysteresis curve of the target [81].

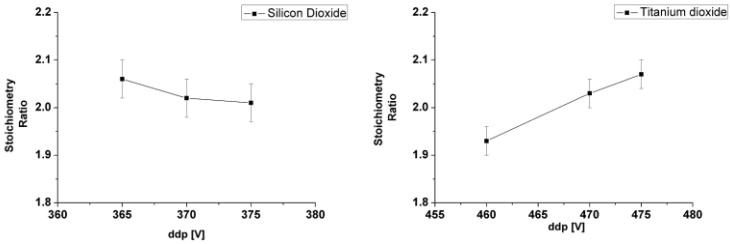

Figure IV-21. Stoichionetry ratio vs. d.d.p. of SiO_2 and TiO_2 thin film.

Table IV-9. Stoichiometry ratio O/Ti calibration.

	TiO_2 thin film	
Ddp [V]	**O/Ti**	**Error [%]**
465	1.99	± 2.0%
465	2.00	± 2.0%
470	2.03	± 2.0%
470	2.03	± 2.0%
470	2.03	± 2.0%
470	2.03	± 2.0%

Table IV-10. Stoichiometry ratio O/Si calibration.

SiO_2 thin film		
Ddp [V]	**O/Ti**	**Error [%]**
365	2.01	± 2.5%
370	2.03	± 2.5%
370	2.02	± 2.5%
370	2.02	± 2.5%
375	2.06	± 2.5%
380	2.15	± 2.5%

The stoichiometry analysis selected as the set point of deposition of d.d.p.= 370 V (SiO_2) and d.d.p.= 470 V (TiO_2).

4.1.5.2 PVD homogeneity deposition

RBS was also used for the mapping of a deposited sample to determine the planar thickness profile achieved.
This allows to find the position in the chamber in order to obtain multilayers with the same optical properties.

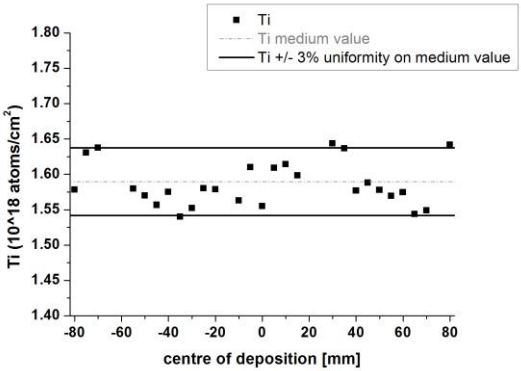

Figure IV-22. Lateral homogeneity deposition.

From RBS lateral homogeneity analysis we evaluated a maximum length of deposition of ± 80mm with respect to the center of the target, with a uniformity of ± 3%.

4.2 Design of optical multilayer

The design of optical multilayer was performed by Tf_Calc software.
The design has been divided as follows:

- Antireflection filter and dichroic mirror design used to characterize the optical properties;
- Design of dichroic filters applied to the photovoltaic concentration system.

4.2.1 AR – Coating design

The design of two different antireflection filters (AR_1 400nm< λ< 650nm) and (AR_2 650nm< λ< 1200nm) has as purpose to analyze the optical properties.
An antireflection filter have a simple design [82] since it is based onfew layers; for this reason easily it lends itself to analysis optics respect to a more complex design as the design of a dichroic filter.

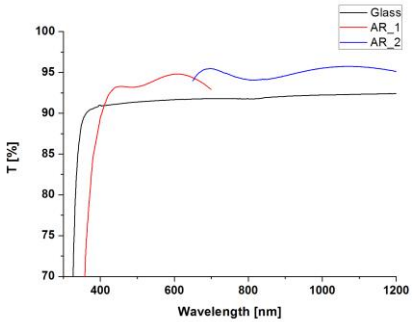

Figure IV-23. Two different antireflection filter design.

Table IV-11. Design parameter of AR_1 multilayer.

AR_1 Design				
Material	**Thickness [nm]**	**Deposition Time [s]**	**d.d.p. [V]**	**Power Generator [W]**
TiO_2	13.5	277	470	1410
SiO_2	27.8	147	370	1480
TiO_2	31.4	646	470	1410
SiO_2	21.5	114	370	1480
TiO_2	21.3	438	470	1410
SiO_2	84.3	446	370	1480

In Figure IV-24, it is compared the optical response of the anti-reflective filter AR_1 designed and realized.
There is mismatch between the two optical feedbacks, which has allowed us to analyze in detail this issue.

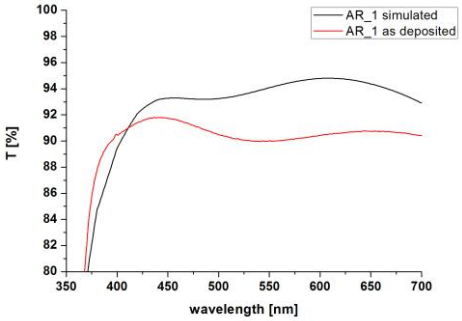

Figure IV-24. Antireflection optical filter AR_1 designed and realized.

The filter design AR_2 optimized the reflectance in the optical band 650nm< λ< 1200nm. The Figure IV-25 shows the difference between the optical design and the experimental optical response of the filter, probably due to

incorrect deposition thicknesses or different optical properties of the deposited material.

Table IV-12. Design parameter of AR_2 multilayer.

AR_2 Design				
Material	**Thickness [nm]**	**Deposition Time [s]**	**d.d.p. [V]**	**Power Generator [W]**
TiO_2	23.1	476	470	1410
SiO_2	81.8	433	370	1480
TiO_2	29.8	614	470	1410
SiO_2	180.5	956	370	1480

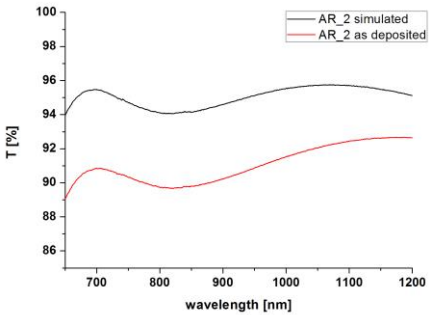

Figure IV-25. Antireflection optical filter AR_2 designed and realized.

4.2.2 Dichroic multilayer design

The dichroic design has involved the definition of two different types of multilayers. The first type is a low-pass filter with an edge at 625 nm and 650 nm, while the second type is always a low-pass filter with an edge at 825 nm. Tree different dichroic filters, denominated Dic_1, Dic_2 and Dic_3, were analyzed showing a marker diffrerence between the optical response of the project and the experimental response of the multilayers [83].

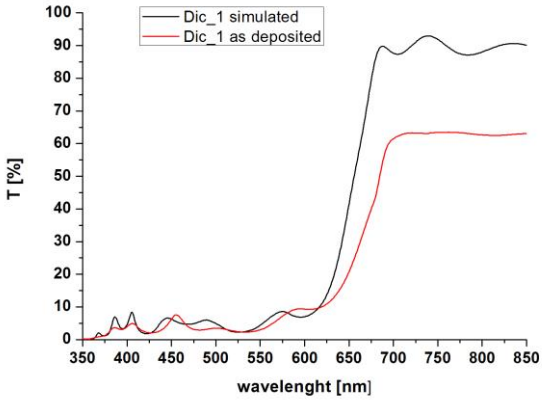

Figure IV-26. Optical response of dichroic filter Dic_1 designed and realized.

Table IV-13. Optical design of dichroic (Dic_1).

Dic_1 Design				
N° Layer	**Material**	**Thickness [nm]**	**d.d.p. [V]**	**Power Generator [W]**
1	TiO_2	32.5	470	1410
2	SiO_2	27.3	370	1480
3	TiO_2	28.3	470	1410
4	SiO_2	47.1	370	1480
5	TiO_2	68.4	470	1410
6	SiO_2	108.6	370	1480
7	TiO_2	45.7	470	1410
8	SiO_2	117.6	370	1480
9	TiO_2	59.4	470	1410
10	SiO_2	95.5	370	1480
11	TiO_2	34.6	470	1410
12	SiO_2	85.6	370	1480
13	TiO_2	9.2	470	1410
14	SiO_2	49.7	370	1480
15	TiO_2	16.8	470	1410
16	SiO_2	74.8	370	1480
17	TiO_2	36.4	470	1410
18	SiO_2	88.8	370	1480
19	TiO_2	30.2	470	1410
20	SiO_2	77.4	370	1480
21	TiO_2	27.7	470	1410
22	SiO_2	95.0	370	1480
23	TiO_2	21.9	470	1410

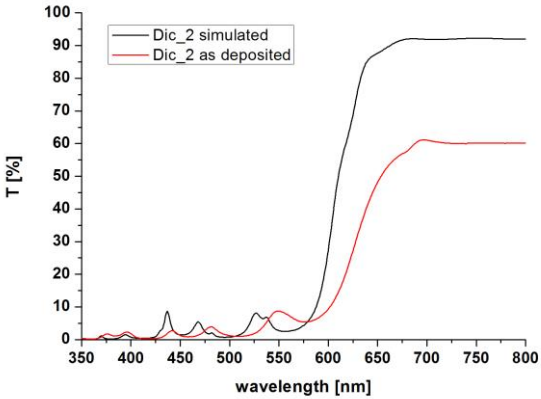

Figure IV-27. Optical response of dichroic filter Dic_2 designed and realized.

Table IV-14. Optical design of dichroic (Dic_2).

Dic_2 Design				
N° Layer	**Material**	**Thickness [nm]**	**d.d.p. [V]**	**Power Generator [W]**
1	TiO_2	29.7	470	1410
2	SiO_2	91.7	370	1480
3	TiO_2	44.8	470	1410
4	SiO_2	123.5	370	1480
5	TiO_2	39.9	470	1410
6	SiO_2	98.2	370	1480
7	TiO_2	65.1	470	1410
8	SiO_2	82.0	370	1480
9	TiO_2	45.6	470	1410
10	SiO_2	106.0	370	1480
11	TiO_2	48.5	470	1410
12	SiO_2	58.7	370	1480
13	TiO_2	34.4	470	1410
14	SiO_2	72.5	370	1480
15	TiO_2	28.7	470	1410
16	SiO_2	90.2	370	1480
17	TiO_2	37.1	470	1410
18	SiO_2	60.9	370	1480
19	TiO_2	21.9	470	1410
20	SiO_2	101.0	370	1480
21	TiO_2	28.5	470	1410
22	SiO_2	71.8	370	1480
23	TiO_2	80.4	470	1410
24	SiO_2	143.7	370	1480

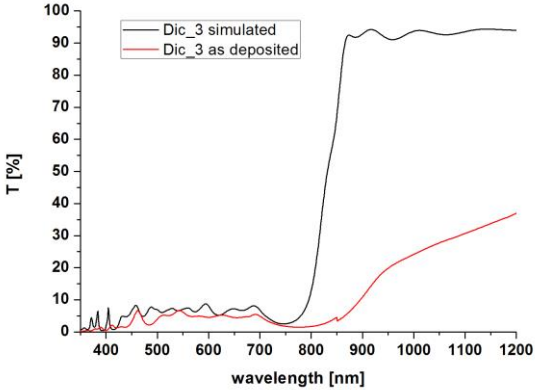

Figure IV-28. Optical response of dichroic filter Dic_3 designed and realized.

Table IV-15. Optical design of dichroic (Dic_3).

Dic_2 Design				
N° Layer	**Material**	**Thickness [nm]**	**d.d.p. [V]**	**Power Generator [W]**
1	TiO_2	47.2	470	1410
2	SiO_2	111.3	370	1480
3	TiO_2	64.0	470	1410
4	SiO_2	107.00	370	1480
5	TiO_2	41.6	470	1410
6	SiO_2	106.1	370	1480
7	TiO_2	60.1	470	1410
8	SiO_2	111.3	370	1480
9	TiO_2	57.7	470	1410
10	SiO_2	201.1	370	1480
11	TiO_2	55.7	470	1410
12	SiO_2	108.7	370	1480
13	TiO_2	107.6	470	1410
14	SiO_2	118.5	370	1480
15	TiO_2	45.4	470	1410
16	SiO_2	55.8	370	1480
17	TiO_2	13.4	470	1410
18	SiO_2	121.7	370	1480
19	TiO_2	59.7	470	1410
20	SiO_2	66.1	370	1480
21	TiO_2	11.6	470	1410
22	SiO_2	119.6	370	1480
23	TiO_2	29.9	470	1410
24	SiO_2	85.2	370	1480
25	TiO_2	11.8	470	1410
26	SiO_2	84.3	370	1480
27	TiO_2	55.0	470	1410
28	SiO_2	19.4	370	1480
29	TiO_2	39.7	470	1410
30	SiO_2	81.1	370	1480
31	TiO_2	15.4	470	1410
32	SiO_2	137.3	370	1480

4.3 Characterization of optical multilayer

4.3.1 Annealing heat treatment

The optical analysis on the antireflection multilayer and dichroic mirror have shown lack of correspondence between the projects and the realized samples. For this reason, the samples were treated with a thermal cycle at a temperature of 350°C for changing the microstructure of the material and its optical properties [84] [85].
The thermal cycle as at atmospheric pressure already mentioned in Figure III-26, was performed both on single layer of titanium dioxide is in and on some multilayers, both antireflection and dichroic.

4.3.1.1 FT-IR analysis

FT-IR analysis was performed on titanium dioxide single layers of deposited on the silicon, taking as a reference the silicon substrate. The absorption peaks of crystalline TiO_2 were studied (Figure IV-29) [22]. FT-IR spectroscopy is used to provide information on the of crystallinity degree of the thin films.
Two absorption peaks can be observed: one at 1100 cm^{-1} corresponds to the Si-O steching mode probably due to surface oxidation of the substrate.
The second peak starting at 990 cm^{-1} corresponds to the absorption peak of Ti-O, with maximum at 446 cm^{-1} wavenumber [86] [87]. The shape and the width of the peak indicate a crystalline structure characterized by heterogeneous Ti-O bond length; this implies a polycristalline or amorphous structure of the sample.

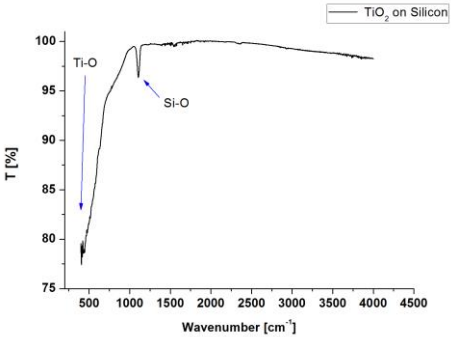

Figure IV-29. IR spectra of TiO_2 on silicon substrate

The analyses are made on TiO_2 thin film of 158.6nm ± 2.3nm on silicon after different heat treatments, in order to observe the evolution as a function of the temperature, as swown in Figure IV-30.

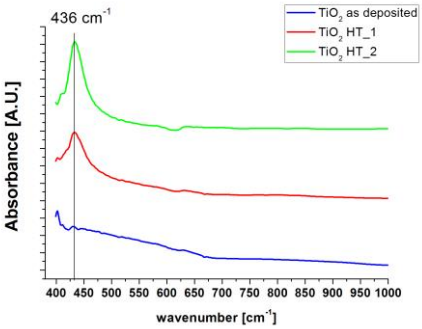

Figure IV-30. Trend of the absorbance of thin films of TiO_2 as a function of the annealing temperature.

Table IV-16. Heat treatment on TiO_2 single layer.

TiO_2 thin film				
Sample	**T [°C]**	**Heating Rate [°C/min]**	**Constant Temperature [hour]**	**Cooling Rate [°C/min]**
TiO_2 as deposited	-	-	-	-
TiO_2_HT_1	330	2	1	1.2
TiO_2_HT_2	350	2	1	1.2

The variation of the absorbance spectrum in the range from 400 cm^{-1} to 700 cm^{-1} that describes the evolution of the material at different treatments.
On the TiO_2 as deposited sample, it is possible to note a broad absorption band in the region 400 cm^{-1} -700 cm^{-1}. The formation of a so wide band corresponds to the presence of bonds Ti-O-Ti with different lengths and characteristic of amorphous phases.
In sample HT_2 treated at 350 ° C it can be noticed the appearance of a well defined peak at 436 cm^{-1}, corresponding to the stretching mode of Ti-O-Ti anatase [88] [24].
Sample HT_1 corresponds to an intermediate state between the amorphous phase and anatase, with a gradual transition from one phase to another, through a process of nucleation and growth.

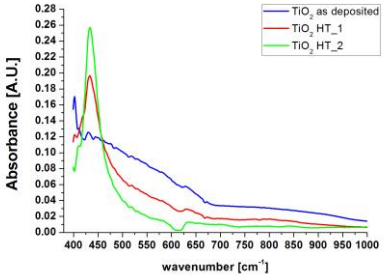

Figure IV-31. Wavenumber range to calculate FWHM.

From Figure IV-31 it was obtained the FWHM value (Figure IV-32) of the three absorption curves, in the range of 400 cm^{-1} - 993cm^{-1}. The interval was determined from the lower limit of sensitivity of the detector (400cm^{-1}) and the wavenumber where it has the first change of slope of the curve of the sample not heat-treated (TiO_2 as deposited), which corresponds to 993cm^{-1}.

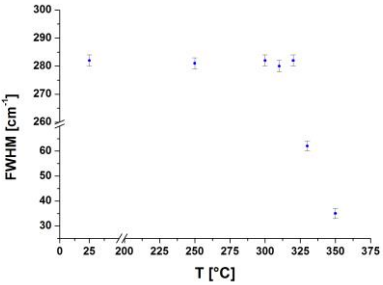

Figure IV-32. FWHM at 436 cm^{-1} as a function of the annealing temperatures.

As can be observed the phase variation occurs within a limited temperature range between 330 and 350°C; below this temperature it remains the in amorphous phase.

Table IV-17. FWHM estimation of different termal treatment.

TiO_2 thin film		
Sample	**Temperature Treatment [°C]**	**FWHM [cm^{-1}]**
TiO_2 as deposited	25	282
TiO_2 HT_A	250	281
TiO_2 HT_B	300	282
TiO_2 HT_C	310	280
TiO_2 HT_D	320	282
TiO_2 HT_E	330	62
TiO_2 HT_F	350	35

4.3.1.2 XRD analysis

To confirm the crystal structure of TiO_2 detected by FT-IR analysis were performed XRD analysis on as deposited TiO_2 and sample HT_2 on silicon substrate.

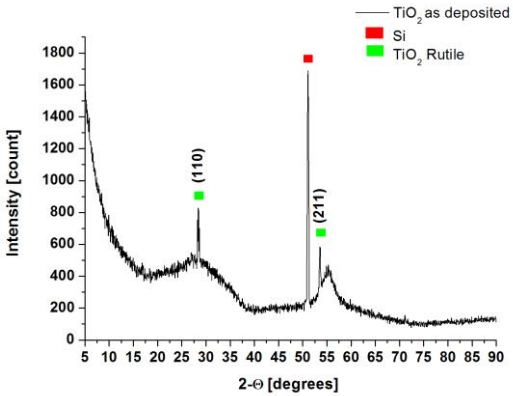

Figure IV-33. XRD spectra of TiO_2 thin film as deposited.

Figure IV-33 illustrates the spectrum produced by the as deposited sample. The peak marked red at 2θ=51.25° correspond to the silicon substrate (100) [89], while the peaks marked in green indicate a trace of rutile phase.
The two peaks broad features near the rutile peaks, indicate the presence of anatase phase in a amorphous structure. The first peak at 2θ = 27.35° is referred to the (110) [90] crystallographic plane of rutile, while the second at 2θ = 53.57 ° indicate the presence of rutile phase (211) [91] immersed in a purely amorphous phase [92] [93].

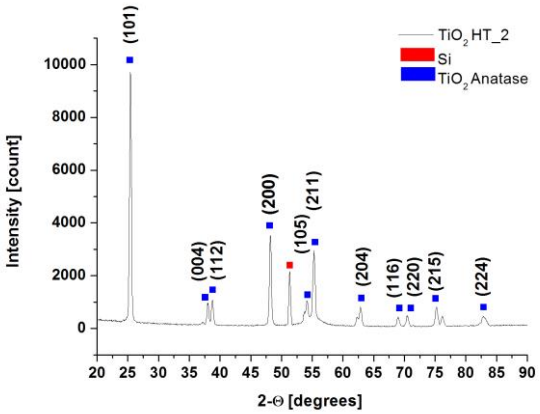

Figure IV-34. XRD spectra of TiO_2 HT_2 thin film termal treatment.

In Figure IV-34 we observe the presence of the most significant peak at 2θ = 25.4 ° referring to the plane (101) of anatase phase [94] [95] [25].
On this peak the crystallite size was calculated by applying the Debye-Scherrer equation [96] [27].

$$D = \frac{k \cdot \lambda}{B \cdot cos\theta} \qquad 20)$$

where:

- k is a constant characteristic of the material (0.89 in our case)
- λ it is the wavelength of the radiation (0.15406 nm for Cu Kα)
- B is the peak FWHM in radians
- θ it is the peak position angle in radiants.

The average grain size, calculated by the Debye-Scherrer formula is equal to 29 nm.

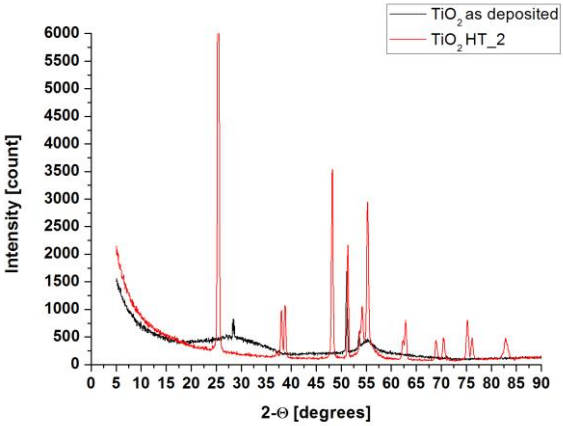

Figure IV-35. XRD spectra of the sample TiO_2 before and after heat treatment.

4.3.2 Spectrophotometric analysis

Aftrer the describe results, on every multilayer an annealing treatment wzas performed [97]. After the annealing treatment we observed the change of the optical response of the multilayers [98].

Table 6.1 shows the parameters of heat treatments on different optical multilayer.

Table IV-18. Heat treatment parameters on the optical multilayers.

TiO_2 thin film				
Sample	**T [°C]**	**Heating Rate [°C/min]**	**Costant Temperature [hour]**	**Cooling Rate [°C/min]**
AR_1	350	2	12	1.2
AR_2	330	2	12	1.2
Dic_1	350	2	24	1.2
Dic_2	350	2	24	1.2
Dic_3	350	2	12	1.2
Dic_3	350	2	24	1.2

The correspondence between design and experimental measurements of the multilayer anti-reflective and dichroic improved significantly after annealing treatment.

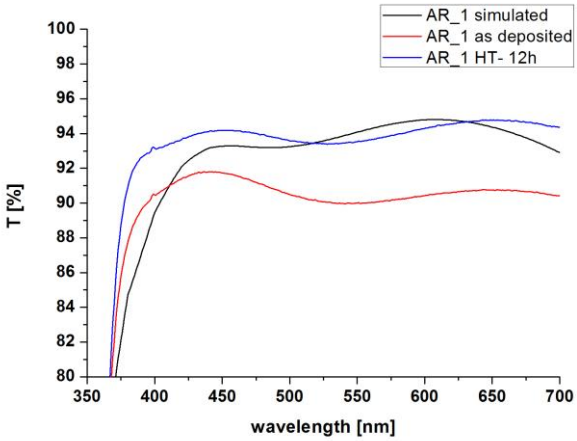

Figure IV-36. Comparative optical spectrum of simulated multilayer as deposited and annealing treatment (AR_1).

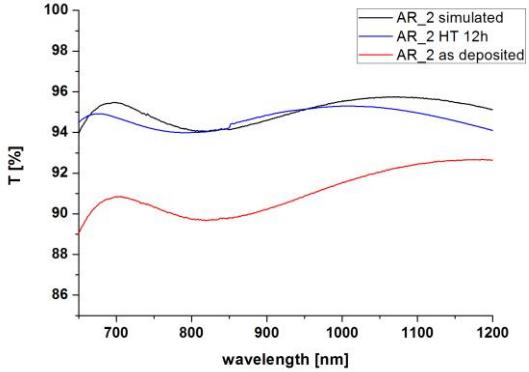

Figure IV-37. Comparative optical spectrum of simulated multilayer as deposited and annealing treatment (AR_2).

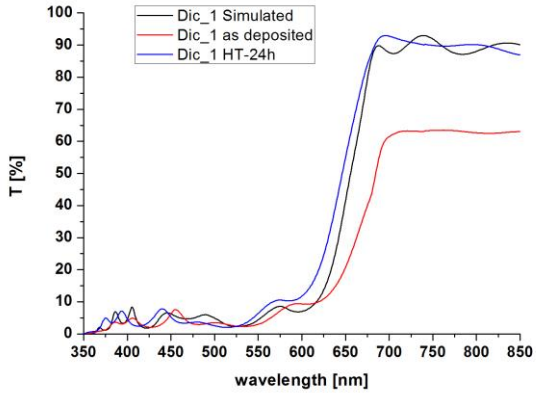

Figure IV-38. Comparative optical spectrum of simulated multilayer as deposited and annealing treatment (Dic_1).

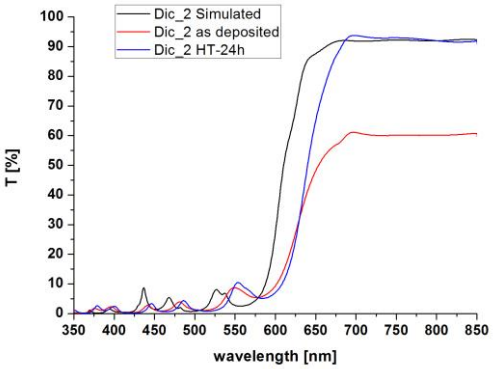

Figure IV-39. Comparative optical spectrum of simulated multilayer as deposited and annealing treatment (Dic_2).

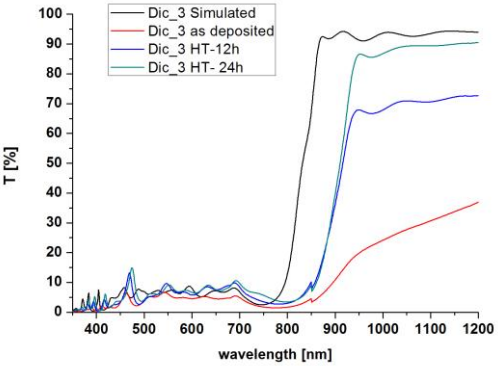

Figure IV-40. Comparative optical spectrum of simulated multilayer as deposited and annealing treatment (Dic_3).

The transmittance average of the different multilayers, was calculated on the optical band transmitted, it is shown Table IV-19.

Table IV-19. Transmittance variation pre and post Heat Treatment on different optical multilayer.

Sample	Optical band [nm]	Transmittance Average [%]	ΔT [%] pre and post HT	ΔT [%] simulated and HT
AR_1	300 - 700	91.5		
AR_1 as deposited	300 - 700	88.9		
AR_1 HT-12h	300 - 700	92.0	+ 3.1	+ 0.5
AR_2	700 - 1200	94.7		
AR_2 as deposited	700 - 1200	91.1		
AR_2 HT-12h	700 - 1200	95.0	+ 4.0	+ 0.3
Dic_1	690 - 850	89.5		
Dic_1 as deposited	690 - 850	62.7		
Dic_1 HT-24h	690 - 850	90.1	+ 27.3	+ 0.5
Dic_2	690 - 850	92.1		
Dic_2 as deposited	690 - 850	59.7		
Dic_2 HT-24h	690 - 850	92.2	+ 32.5	+ 0.2
Dic_3	870 - 1200	94.7		
Dic_3 as deposited	870 - 1200	25.1		
Dic_3 HT-12h	870 - 1200	70.2	+ 45.1	- 23.1
Dic_3 HT-24h	870 - 1200	88.5	+ 63.5	- 4.7

Table IV-20. Transmittance average of TiO_2 in multilayer optical filter as function of thickness.

Sample	Thick TiO_2 [nm]	Thick SiO_2 [nm]	Tot. Thick [nm]	T [%] average
AR_1	52.1	263.6	316.6	89.0
AR_2	66.2	134.3	200.5	91.1
Dic_1	463.5	969.1	1432.6	62.7
Dic_2	504.8	1099.5	1604.4	59.8
Dic_3	716.1	1634.6	2350.6	25.1

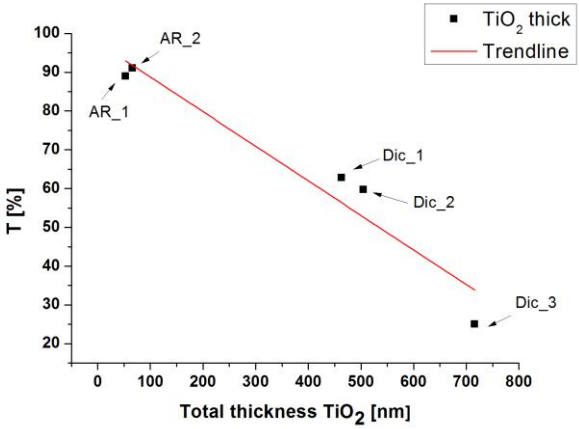

Figure IV-41. Trend of average transmittance of TiO_2 as function of thickness.

4.3.3 (RBS) analysis

Treated and untreated multylayers were analyzed with the RBS technique in order to assess possible changes in stoichiometry and for thickness variations.

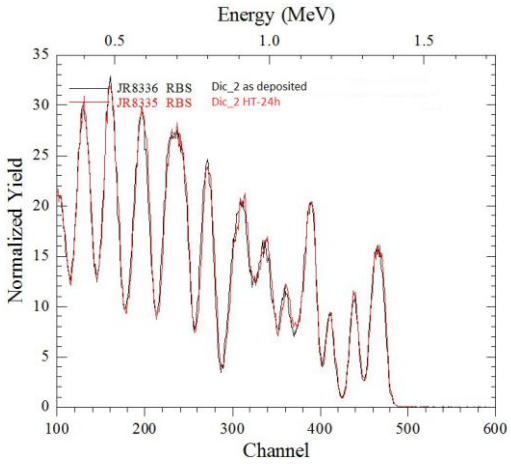

Figure IV-42. RBS spectra of Dic_1 as deposited and heat treated at 350°C - 24h.

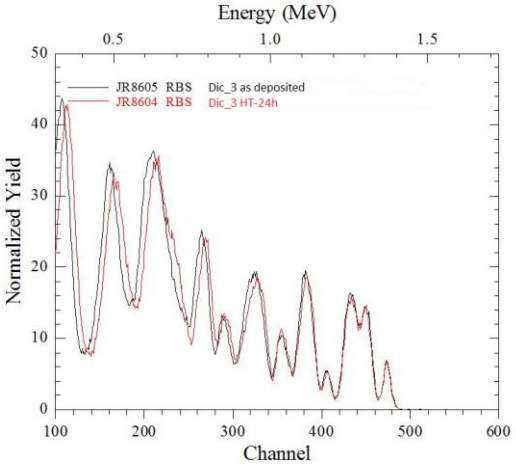

Figure IV-43. RBS spectra of Dic_3 as deposited and heat treated at 350°C - 24h.

The spectra analysis is not detailed since it is hard to extract the thicknes values of the layers. Actually a more reliable measure was undertaken with atomic force microscopy on multilayer deposited before and after treatment to verify possible change of thickness.
In Figure IV-44 is shown the correlation between experimental RBS spectrum of a dichroic Dic_1 as recorded and a simulation performed with X-Rump software taking into account the correlation with the AFM measurements conducted on two single layers of TiO_2 and SiO_2 performed to calibrate each layer of the multilayer [99].

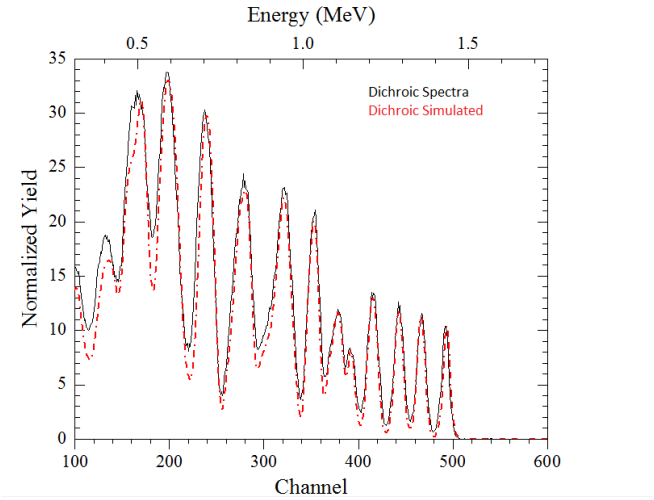

Figure IV-44. RBS spectra dichroic Dic_1 as deposited vs X-Rump spectra simulation.

Table IV-21. RBS spectra X-Rump simulation of dichroic Dic_1.

n° layer	Material	Dose (m/cm2)	thickness (nm)
1	**TiO_2**	63.9	21.9
2	**SiO_2**	224.2	95.0
3	**TiO_2**	80.8	27.7
4	**SiO_2**	182.6	77.4
5	**TiO_2**	88.1	30.2
6	**SiO_2**	209.5	88.8
7	**TiO_2**	106.1	36.4
8	**SiO_2**	176.5	74.8
9	**TiO_2**	49.0	16.8
10	**SiO_2**	117.3	49.7
11	**TiO_2**	26.8	9.21
12	**SiO_2**	202	85.6
13	**TiO_2**	101	34.6
14	**SiO_2**	225.4	95.5
15	**TiO_2**	173.1	59.4
16	**SiO_2**	239.6	101.5
17	**TiO_2**	151.7	52.1
18	**SiO_2**	277.3	117.6
19	**TiO_2**	133.3	45.76
20	**SiO_2**	256.3	108.6
21	**TiO_2**	199.2	68.4
22	**SiO_2**	111.1	47.1
23	**TiO_2**	82.5	28.3
24	**SiO_2**	64.4	27.3
25	**TiO_2**	94.5	32.5

4.3.4 Atomic Force Microscope (AFM) analysis

In this paragraph we shown the thickness measurement with the AFM of multilayers (Antireflection and Dichroic) pre and post annealing treatment.

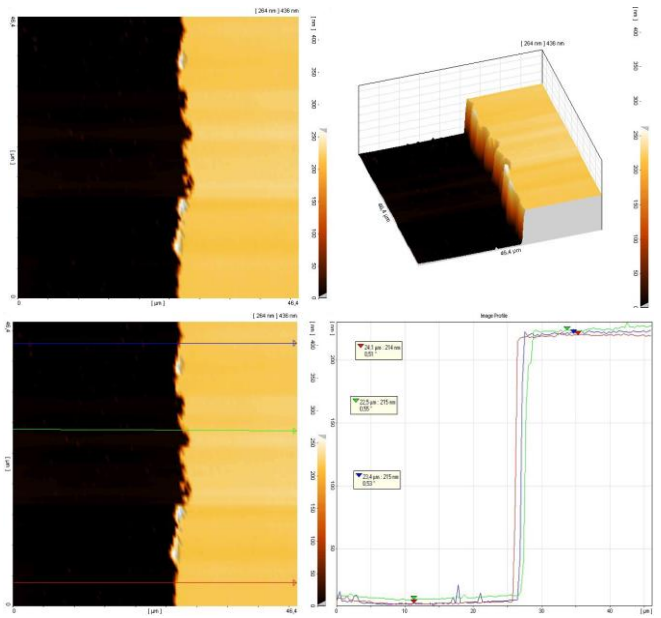

Figure IV-45. AFM measurements of the sample AR_1 after heat treatment.

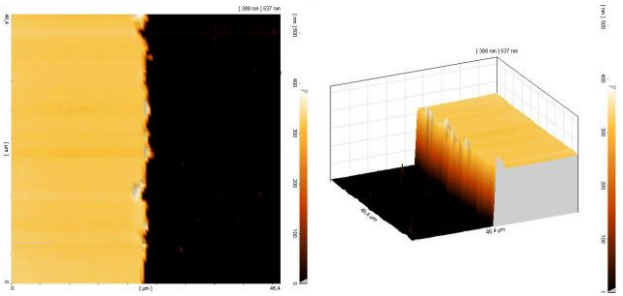

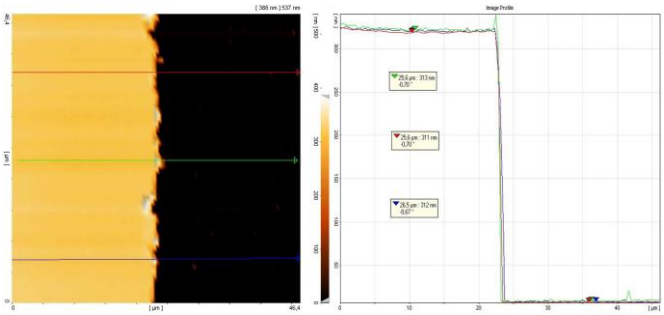

Figure IV-46. AFM measurements of the sample AR_2 after heat treatment.

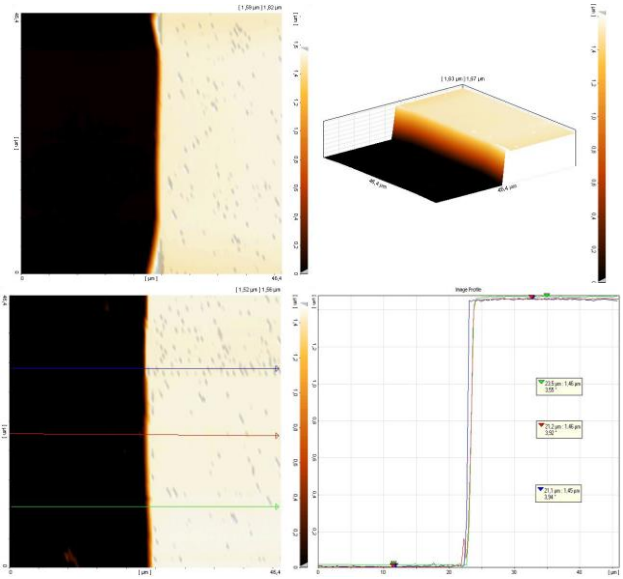

Figure IV-47. AFM measurements of the sample Dic_1 after heat treatment.

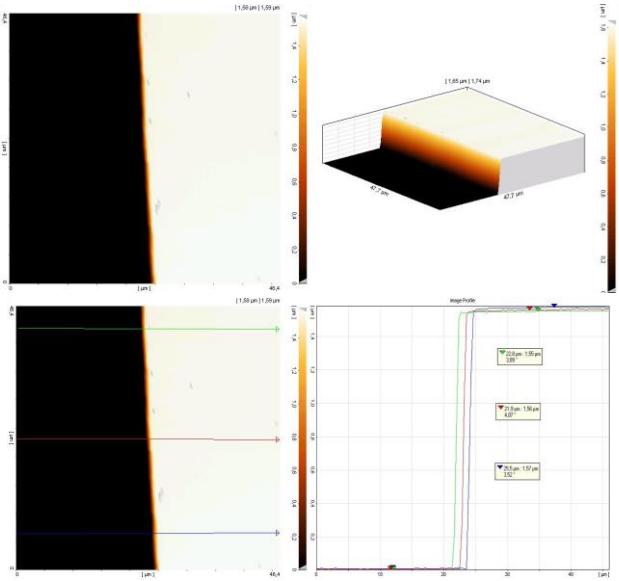

Figure IV-48. AFM measurements of the sample Dic_2 after heat treatment.

Table IV-22. Thickness values measured after treatment and designed

	Thickness average [nm]	Dev-Stand Thickness [nm]	Measure Error [%]	Thick design [nm]	Error respect to design [%]
AR_1	210.3	2.1	0.9	200.5	4.6
AR_1 HT	209.3	2.1	0.9	200.5	4.1
AR_2	313.0	2.8	0.9	316.6	1.2
AR_2 HT	312.0	2.8	0.9	316.6	1.5
Dic_1	1469.8	17.9	1.2	1432.7	2.5
Dic_1 HT	1455.2	25.8	1.8	1432.7	1.5
Dic_2	1585.0	16.9	1.1	1604.3	1.2
Dic_2 HT	1583.1	29.02	1.1	1604.3	1.2

4.3.5 Scanning Electron Microscope analysis (SEM)

Cross-section measurements were carried out with the scanning electron microscope allow to emphasize the deposited individual layers of the multilayer.
In images obtained with back-scattered electron (BSE) it is possible to note the alternating layers of high atomic number Z (TiO_2) with shades towards white, compared to layers with low atomic number Z (SiO_2) with shades to black [65]. This is even more evident in the images conducted with the secondary electrons (SE).

Table IV-23. Design project of dichroic analyze with SEM technique in cross section.

n° layer	Material	thickness (nm)
1	**TiO_2**	18.2
2	**SiO_2**	165.1
3	**TiO_2**	63.8
4	**SiO_2**	129.2
5	**TiO_2**	58.6
6	**SiO_2**	111.8
7	**TiO_2**	37.9
8	**SiO_2**	118.4
9	**TiO_2**	67.7
10	**SiO_2**	126.3
11	**TiO_2**	64.5
12	**SiO_2**	220.9
13	**TiO_2**	61.6
14	**SiO_2**	114.5
15	**TiO_2**	119.8
16	**SiO_2**	109.6
17	**TiO_2**	56.8
18	**SiO_2**	241.6
19	**TiO_2**	44.1
20	**SiO_2**	92.2
21	**TiO_2**	18.4
22	**SiO_2**	94.5
23	**TiO_2**	32.8

Figure IV-49 show the cross-section SEM immage of a dicroic filter [14] [100] with a total design thickness is 2168.5 nm (644.2 nm = of TiO_2 layers and 1524.3 nm = of SiO_2 layers).

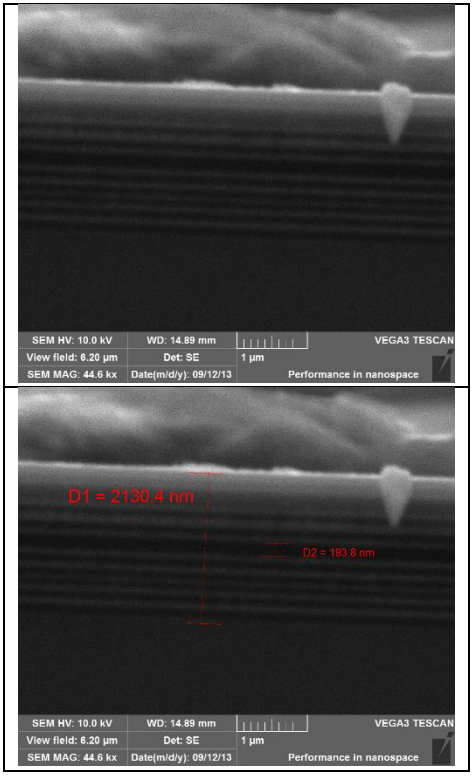

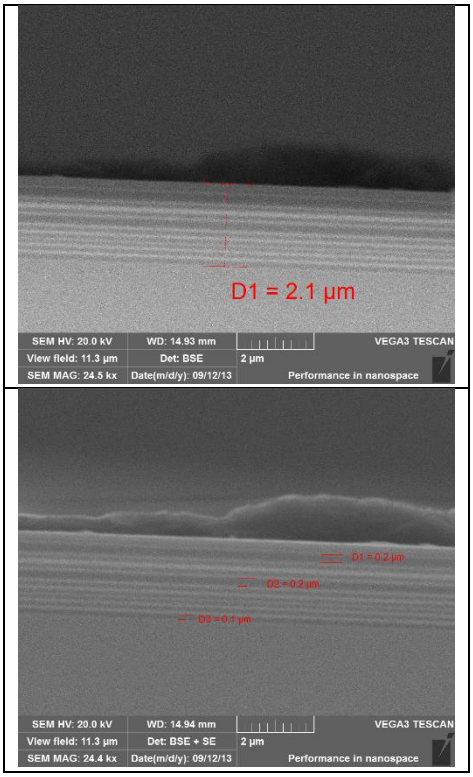

Figure IV-49. SEM cross-section image of dichroic optical multilayer.

The SEM images have enabled us to evaluate the quality of the deposition process by quantifying some thickness of a dichroic realized and comparing them with the thicknesses of the project.

4.3.6 Optical measure after annealing

Optical measurements were carried on TiO_2 thin films both as deposited and after heat treatment. In Figure IV-50 and Figure IV-51 the change in transmittance after heat treatment is highlighted [101].

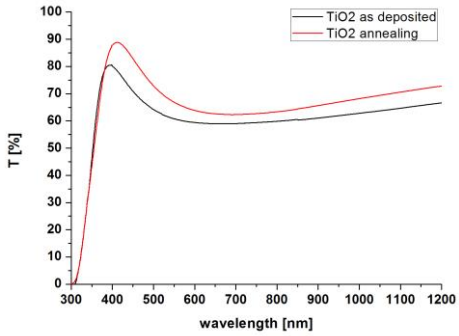

Figure IV-50. Thin film of TiO2 as deposited vs annealing (thickness = 79nm).

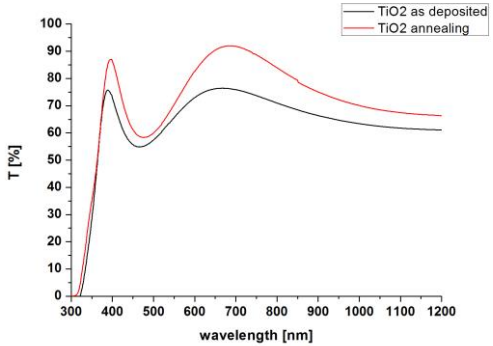

Figure IV-51. Thin film of TiO2 as deposited vs annealing (thickness = 158nm).

In particular, the refractive index variation after phase transformation is analyzed.

It can be noticed an increase of the refractive index and a slight decrease of the extinction coefficient (Figure IV-52 and Figure IV-53).

The variation of transmittance of the deposited multilayer is related to the variation of the coefficients n(λ) and k(λ). The n(λ) in particular decrease with

the crystallization from mix compound to anatase phase, and k(λ) decreases [26] [53] [27]. The optical variation improve the transmitted band of the realized optical filters [102] [103].

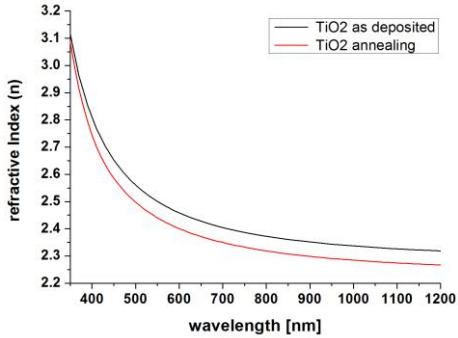

Figure IV-52. Refractive index of TiO_2 as deposited and after annealing.

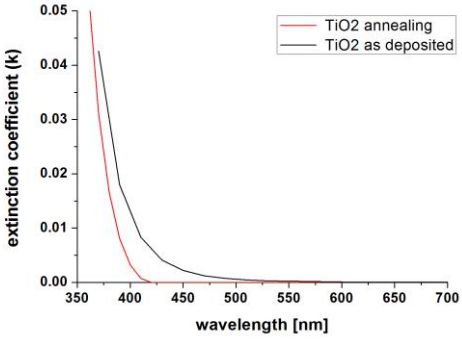

Figure IV-53. Extinction coefficient of TiO_2 as deposited and after annealing.

4.4 Concentrated Photovoltaic (CPV) splitting system

The CPV prototype was designed and analyzed as a function of the components.
The CPV system is composed of:

- primary optical system (NOI);
- dichroic splitting system;
- secondary optical system (SOE);
- photovoltaic cells EQE;
- solar tracking system

4.4.1 Dichroic filter

The photovoltaic cells are the final part of the whole CPV. However, they are the first part to be chosen as regards the design of the CPV system.
In particular, the optical bands are selecter depending on the External Quantum Efficiency (EQE of the cells, which are of Gallium Arsenide (GaAs) and Silicon (Si).

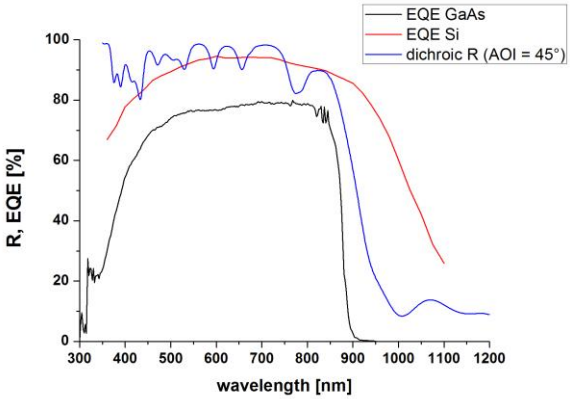

Figure IV-54. EQE of GaAs and Si cell and dichroic optical design.

A specific dichroic was designed and realized (Figure IV-55) which allows to match the two single-junction PV cells (SJSC). So, the prototype should be able to convert the range from 350 to 1200 nm.

Table IV-24. Dichroic optical target design.

Optical Target design AOI= 45°	
T [%]	**λ [nm]**
0	350 < λ< 850
50	λ= 900
100	950 < λ< 1200

Table IV-25. Dichroic optical simulation.

Optical Dichroic design AOI= 45°	
T Ave. [%]	**λ [nm]**
19.8	350 < λ< 850
50	λ= 894
92.1	950 < λ< 1200

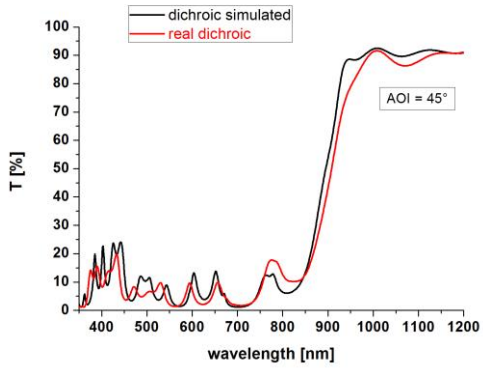

Figure IV-55. Transmittance of a dichroic used in the CPV system.

Table IV-26. Design of dichroic used in CPV prototype system.

N° layer	Material	Thickness [nm]
1	**TiO_2**	79.8
2	**SiO_2**	89.7
3	**TiO_2**	79.1
4	**SiO_2**	162.1
5	**TiO_2**	74.2
6	**SiO_2**	147.7
7	**TiO_2**	69.9
8	**SiO_2**	157.4
9	**TiO_2**	89.9
10	**SiO_2**	89.8
11	**TiO_2**	67.2
12	**SiO_2**	95.6
13	**TiO_2**	43.4
14	**SiO_2**	97.5
15	**TiO_2**	70.1
16	**SiO_2**	89.6
17	**TiO_2**	37.8
18	**SiO_2**	77.6
19	**TiO_2**	105.9
20	**SiO_2**	113.5
21	**TiO_2**	42.7

4.4.2 Solar radiation and tracking system

The CPV require a bi-axial tracking system in order to be always aligned with the solar radiation.
In this research work we used the solar tracking system AKKUTrack® with angular pointing sensitivity <0.1°, controlled by EVA software (Figure IV-56).

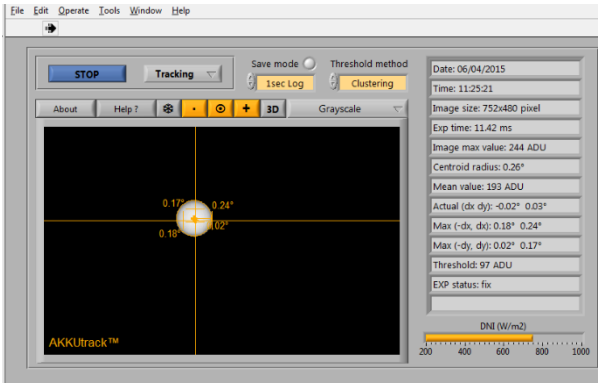

Figure IV-56. EVA software for control of the two-axis tracking system.

Furthermore, this solar tracking system allows analyzing the irradiance of the sun and can be mapped the sun.

It is therefore crucial the acquisition of the daily value of the Direct Normal Irradiance [W/m^2] (DNI) (Figure IV-57) to calculate the efficiency of the prototype system [104] [105].

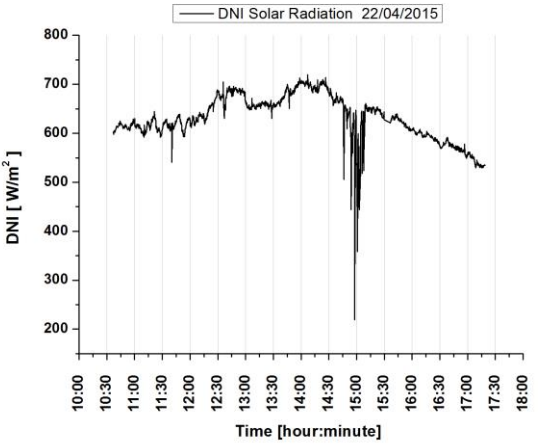

a)

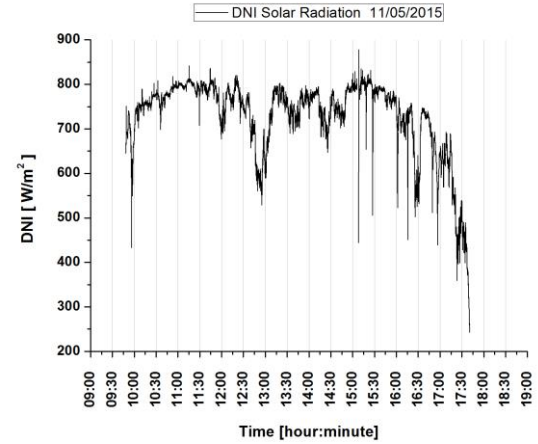

b)

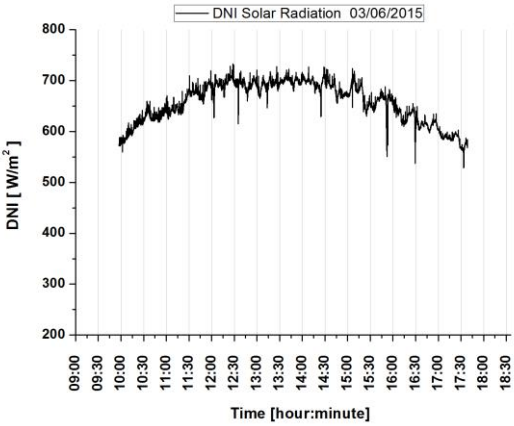

c)

Figure IV-57. Example of DNI daily experimental measures in 2015: a) April, b) May, c) June.

4.5 CPV Ray tracing design

The optical design of the CPV prototype has been conducted by means of the ray tracing Zemax®.
Ray tracing is a widely used technique for the simulation of the propagation of light through an optical system. The simulation of light propagation by means of ray tracing is also commonly called geometrical optics.
There are two typical ways to design with the ray tracing technique: sequential ray tracing and non-sequential ray tracing.
In sequential ray tracing the rays are traced through a predefined sequence of surfaces as they move from the land to the image of our system. The rays hit every surface in the order in which they were defined. Many imaging systems are well described by a sequential list of surfaces, each of them defining the boundary between a medium and the next.
In non-sequential ray tracing, the rays can hit different surfaces and objects not necessarily in the order they are listed in the software interface. In this mode the rays could hit the same object several times or even fail completely certain objects. Generally, the order in which the objects are affected depends on their geometry on the position and on the angle at which the rays enter the system. In non-sequential mode, the optical components are modeled as three dimensional objects, and each object has an orientation in the space (x,y,z) well-defined and independent of the other elements of the system. The rays can propagate through the optical components in any order, and trajectories take into account the possibility to suffer total internal reflection from the surfaces crossing.
Zemax software consists in an integrated environment in which it is possible to model an optical system in the form of lenses or mirrors disposed along an optical path, for analyzing the quality of the projected image from a source and then optimizing the constructive characteristics.
The user interface (Figure IV-58) consists of a table in which each row is a surface or optical element and whose columns contain the parameters of design and construction. The rays are always sent from a surface source (OBJ) to arrive at an image surface (IMA), through a sequence of surfaces inserted in the optical system.

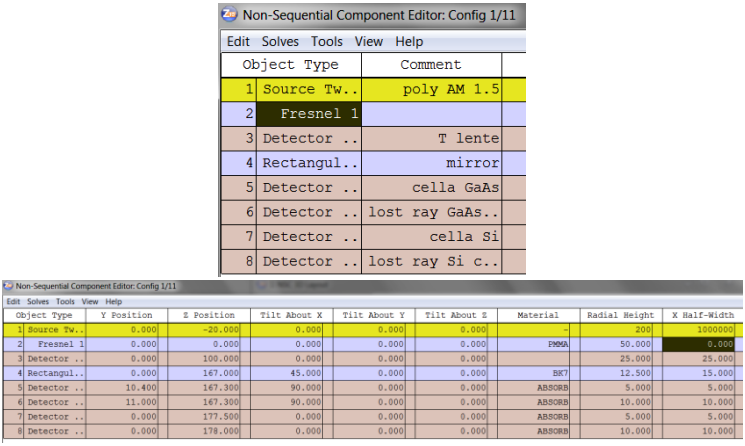

Figure IV-58. Zemax user interface

The first input parameter is the incoming solar spectrum AM = 1.5, in order to simulate the geometrical optics in the optical range of interest (Figure IV-59).

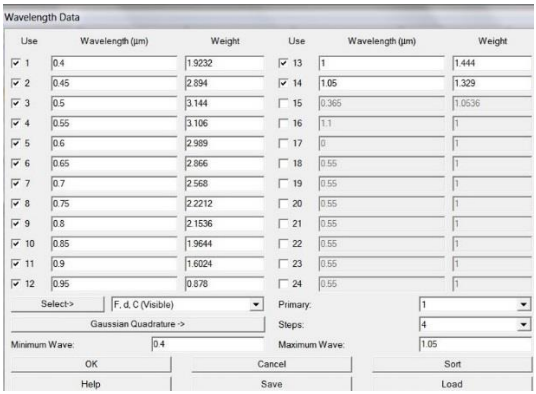

Figure IV-59. Input solar spectra parameter.

The 2D layout design shown in Figure IV-60 depicts the optical convergence of the solar rays entering in the first surface of the Fresnel lens with an angular divergence of 0.27°, and interacting with a second surface which is the dichroic filter. Between the two object, lens and dichroic, an ideal detector for quantifying optical losses.
The light splitted by the dichroic filter converges on two ideals detectors that simulate the two photovoltaic cells, and behind them, there are additional detectors which quantify the component of lost rays in the optical simulation.

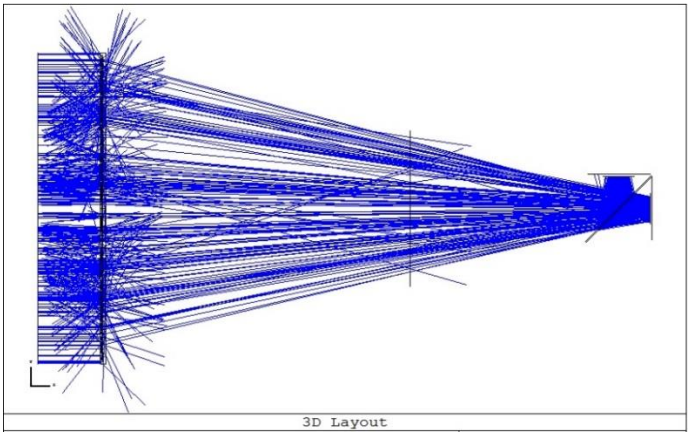

Figure IV-60. 2D Layout Zemax design.

It was conducted a simulation by varying the f/number of the Fresnel lens. Such CPV system differs from commercial CPV where the primary optics focuses the solar radiation directly on the photovoltaic cell (MJSC), due to the presence of the interposed dichroic filter.
The f/number is measure the aperture of the lens, and it describe the ratio of the effective focal length (EFL) to the diameter of the lens (Ø_{lens}) [106].

$$f/number = \frac{EFL}{\text{Ø}_{\text{lens}}} \qquad 17)$$

In Figure IV-61 are shown the results of the simulation of the optical efficiency prototype system as a function of the f/number value.

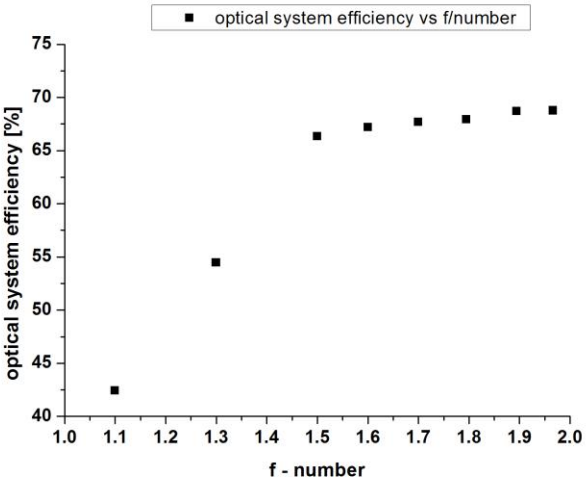

Figure IV-61. Optical efficiency vs f/number value.

The main motivation for this study is the fact that the dichroic filter is designed for an angle of incidence of 45°. In this case it is struck by a beam not collimated but with a cone angle.

Therefore, by analyzing the optical response of the dichroic filter at an angle of incidence between 0 ° and 70 ° (Figure IV-62) it is possible to observe the edge shift and the variation of optical efficiency in the two designed optical bands [14] [17].

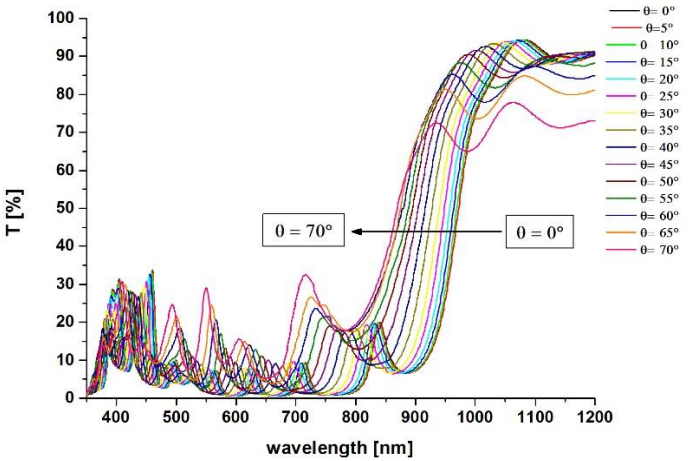

Figure IV-62. Experimental optical transmittance of the dichroic filter as a function of the incidence angle.

Figure IV-63 shows the trend of the optical loss of the system splitting or dichroic and two photovoltaic cells, with respect to the radiation emerging from the Fresnel lens.

Is possible to note how the optical loss increases as the aperture angle of the lens increases (49° at f/1.1), vice versa it tends to decrease when the lens angle is reduced (28° at f/2).

These simulations show that with the CPV system with spectral separation nees high f/number in order to limit optical loss of the dichroic filter varying the angle of incidence.

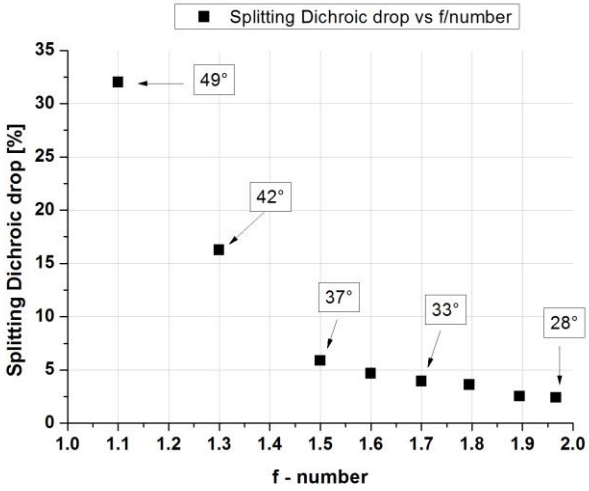

Figure IV-63. Splitting dichroic drop efficiency as function of f/number.

In the next step as the interval of f/number was selected from 1.7 to 2, where it shows better results.

In Figure IV-64, Figure IV-65 and Figure IV-66 some simulation results for the optical components of the optical system are shown, such as lens or dichroic filter for a range of f/number ranging from 1.77 to 1.775.

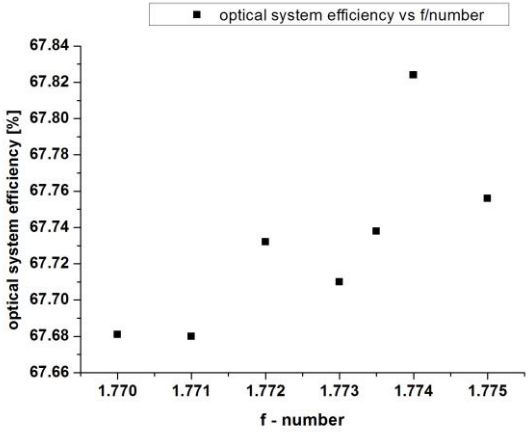

Figure IV-64. Optical system efficiency vs f/number (1.77 < f/# < 1.775).

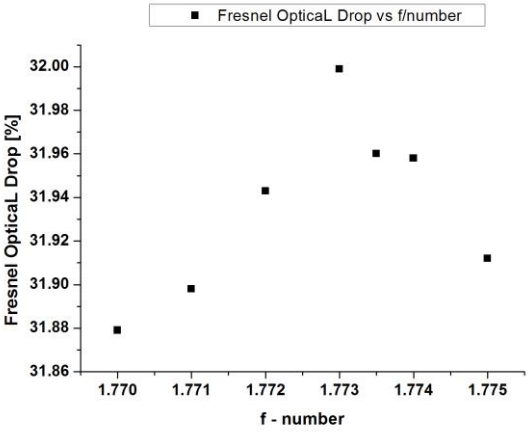

Figure IV-65. Fresnel Optical drop vs f/number (1.77 < f/# < 1.775).

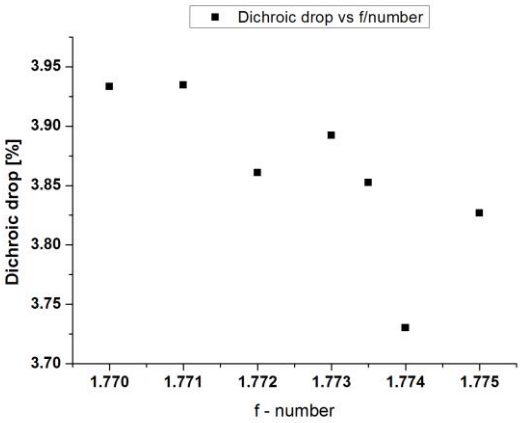

Figure IV-66. Dichroic drop efficiency vs f/number (1.77 < f/# < 1.775.)

4.5.1 Ray tracing tilting angle

The CPV systems are heavily dependent on the alignment of the tracking system with respet to the sun's rays.
The optical design of CPV was by varying the incidence angle on the Fresnel lens (Figure IV-67). In the design, the misalignment between the biaxial tacking and solar rays was simulated by changing the angle of inclination of the Fresnel lens.

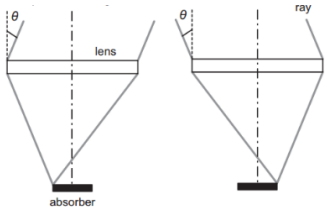

Figure IV-67. Non-imaging Fresnel lens with acceptance angle [107].

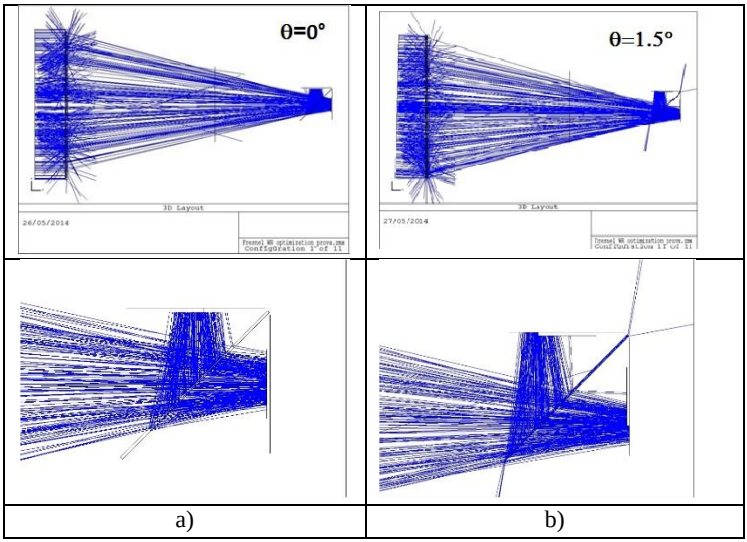

Figure IV-68. CPV system acceptance angle: a) tilting angle θ=O°, b) tilting angle θ=1.5°.

4.5.1.1 CPV Ray tracing design without solar rod

The CPV system is designed with a direct concentration on ideal detector (GaAs and Si) without the use of secondary optics with a concentration of 224X.

4.5.1.1.1 *"GaAs" ideal detector*

Table IV-27. Layout of ray tracing tilting angle on "GaAs" ideal detector.

Layout "GaAs" ideal detector vs tilt acceptance angle		
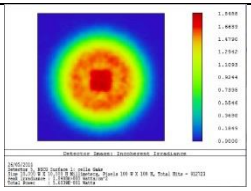	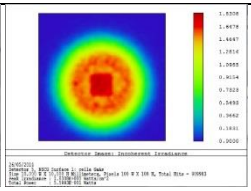	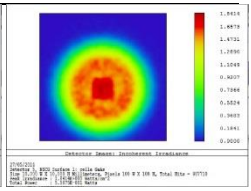
θ=0°	θ=0.1°	θ=0.2°
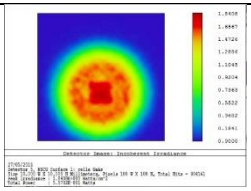	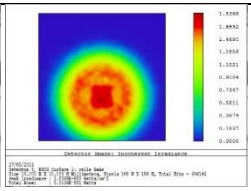	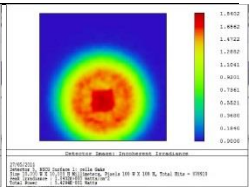
θ=0.3°	θ=0.4°	θ=0.5°
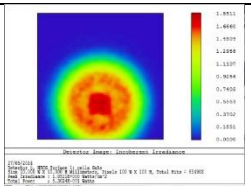	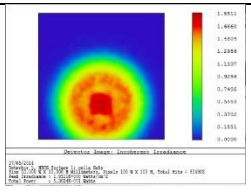	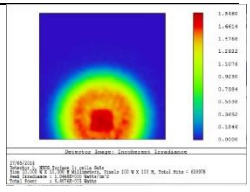
θ=0.6°	θ=0.8°	θ=1.0°
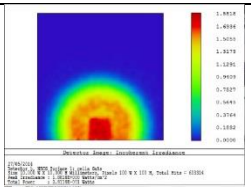	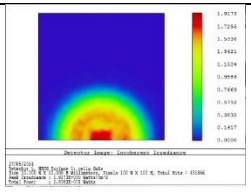	
θ=1.2°	θ=1.5°	

Table IV-28. Layout of ray tracing tilting angle on lost ray "GaAs" ideal detector.

Layout lost ray "GaAs" ideal detector vs tilt acceptance angle		
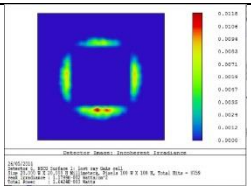	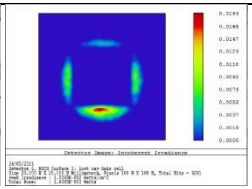	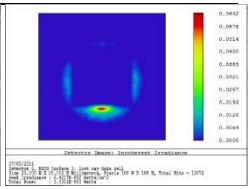
θ=0°	θ=0.1°	θ=0.2°
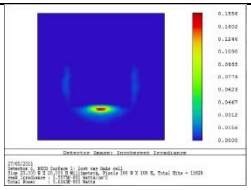	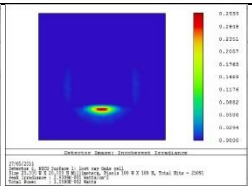	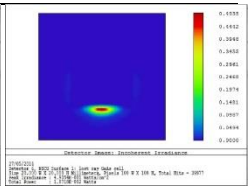
θ=0.3°	θ=0.4°	θ=0.5°
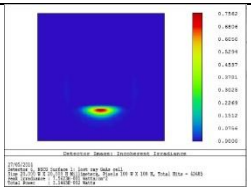	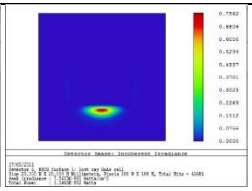	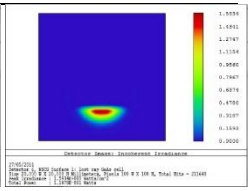
θ=0.6°	θ=0.8°	θ=1.0°
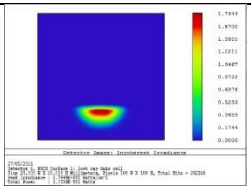	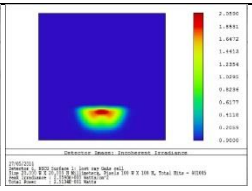	
θ=1.2°	θ=1.5°	

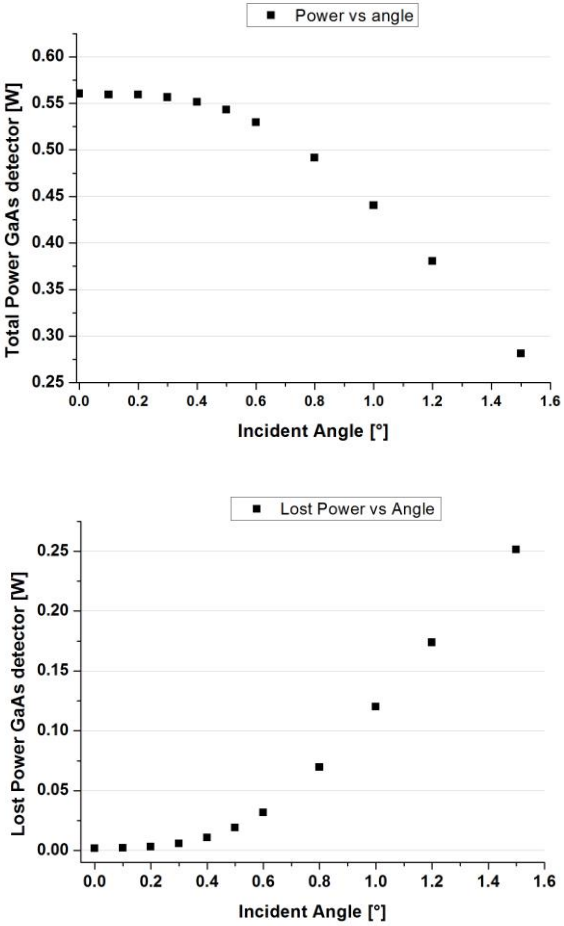

Figure IV-69. Power and lost power of "GaAs" ideal detector vs incidence angle.

4.5.1.1.2 "Si" ideal detector

Table IV-29. Layout of ray tracing tilting angle on "Si" ideal detector.

Layout "Si" ideal detector vs tilt acceptance angle		
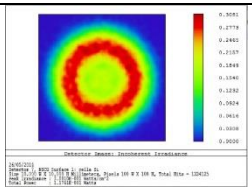	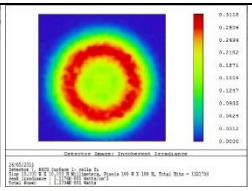	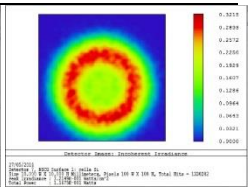
θ=0°	θ=0.1°	θ=0.2°
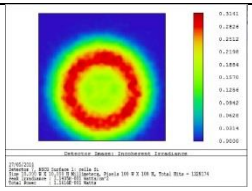	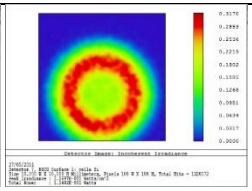	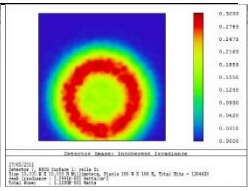
θ=0.3°	θ=0.4°	θ=0.5°
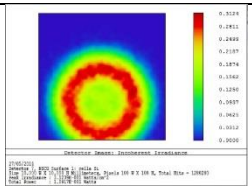	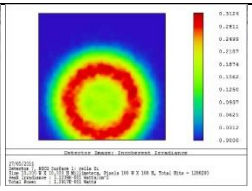	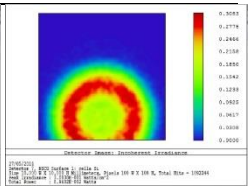
θ=0.6°	θ=0.8°	θ=1.0°
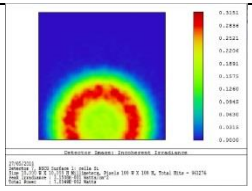	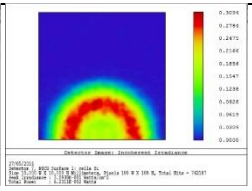	
θ=1.2°	θ=1.5°	

Table IV-30. Layout of ray tracing tilting angle on lost ray "Si" ideal detector.

Layout lost ray "GaAs" ideal detector vs tilt acceptance angle		
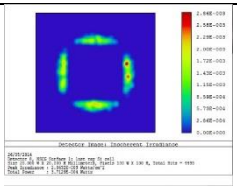	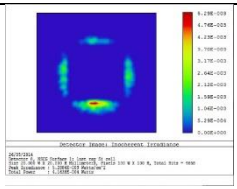	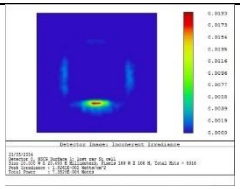
θ=0°	θ=0.1°	θ=0.2°
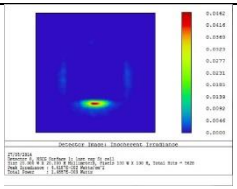	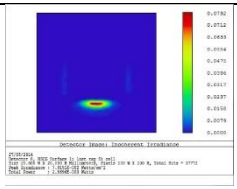	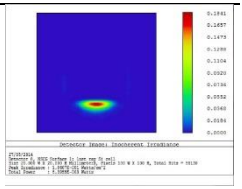
θ=0.3°	θ=0.4°	θ=0.5°
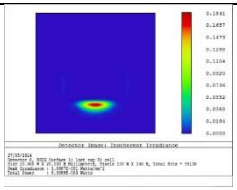	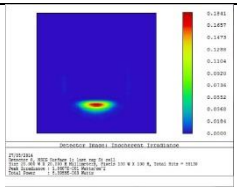	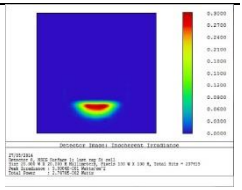
θ=0.6°	θ=0.8°	θ=1.0°
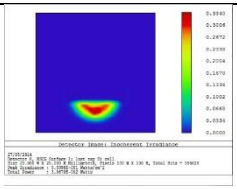	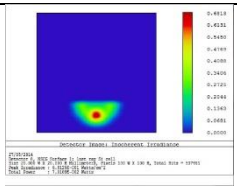	
θ=1.2°	θ=1.5°	

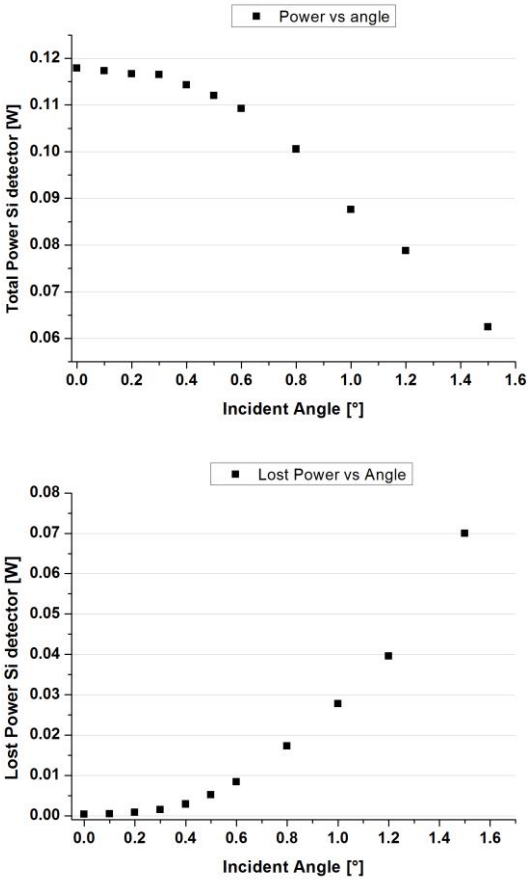

Figure IV-70. Power and lost power of "Si" ideal detector vs incidence angle.

4.5.1.1.3 Total design system without solar rod

It is possible to highlight that the optical design performed have a good optical efficiency, equal to 66-67% up to a tilting angle of t of 0.4° (Figure IV-71). Similarly, the system loss remains constant up to an angle of 0.4° (Figure

IV-72) and then grows very quickly. This is due to the spot of the solar radiation, which tends to exit from the cells by increasing the tilting angle (Table IV-27) (Table IV-29).

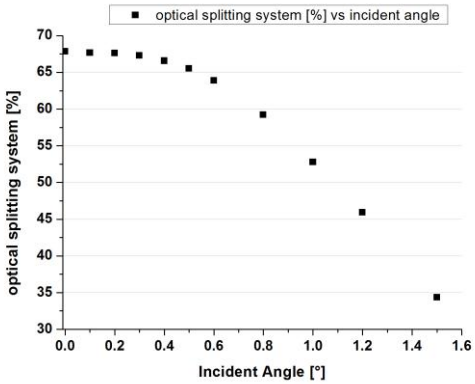

Figure IV-71. Optical splitting system efficiency without solar rod at different incident angle.

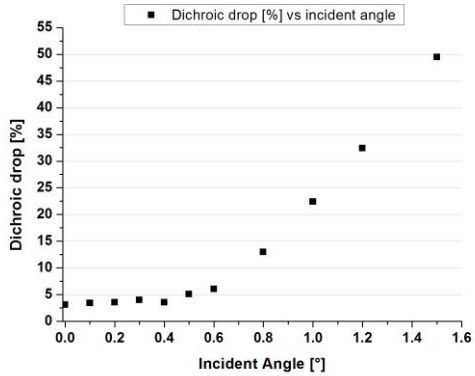

Figure IV-72. Dichroic drop efficiency at different incident angle.

4.5.1.2 CPV Ray tracing design with solar rod

A lens ray tracing design was conducted by inserting a secondary optic element (SOE) which has the function of homogenizing the radiation on the cells and to improve the angular acceptance of the system [108].

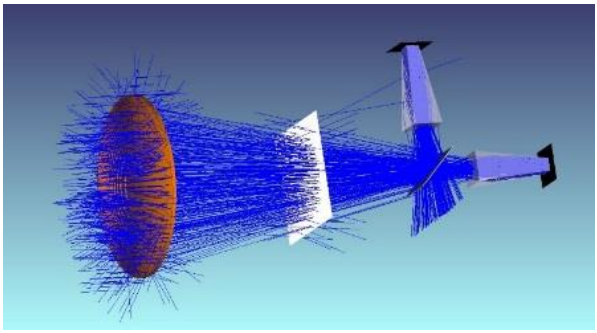

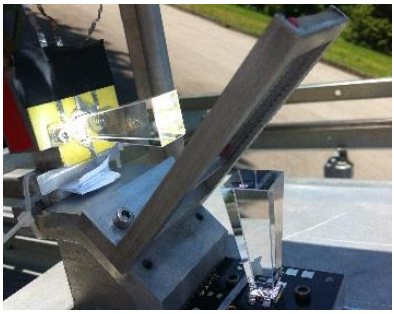

Figure IV-73. CPV splitting system with secondary optics element (SOE) solar rod.

4.5.1.2.1 *"GaAs" ideal detector*

Table IV-31. Layout ray tracing tilt acceptance angle on "GaAs" ideal detector with solar rod.

Layout "GaAs" ideal detector vs tilt acceptance angle		
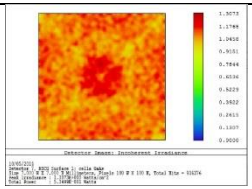	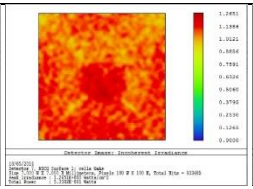	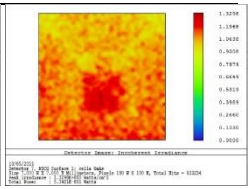
θ=0°	θ=0.1°	θ=0.2°
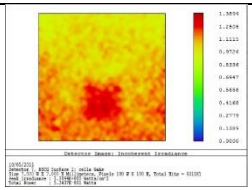	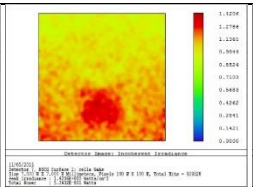	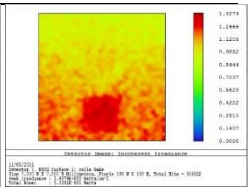
θ=0.3°	θ=0.4°	θ=0.5°
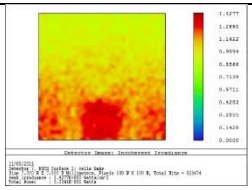	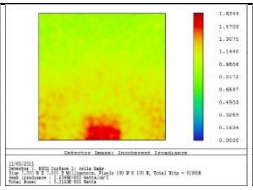	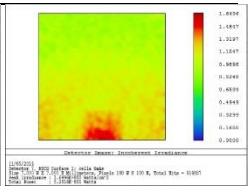
θ=0.6°	θ=0.8°	θ=1.0°

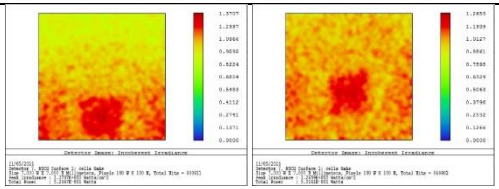

θ=1.2° θ=1.5°

Table IV-32. Layout ray of tracing tilting angle on lost ray "GaAs" ideal detector with solar rod.

Layout lost ray "GaAs" ideal detector vs tilt acceptance angle

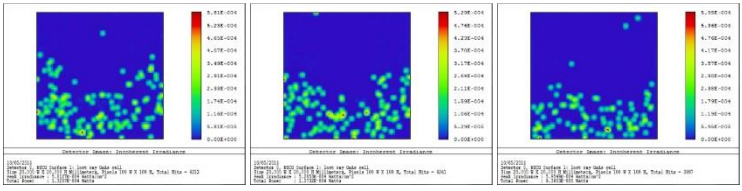

θ=0° θ=0.1° θ=0.2°

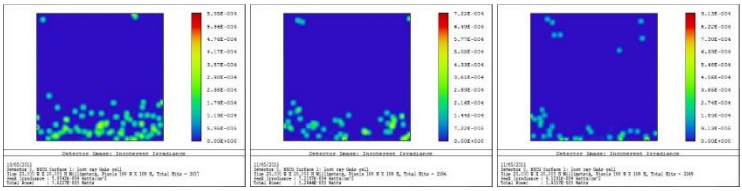

θ=0.3° θ=0.4° θ=0.5°

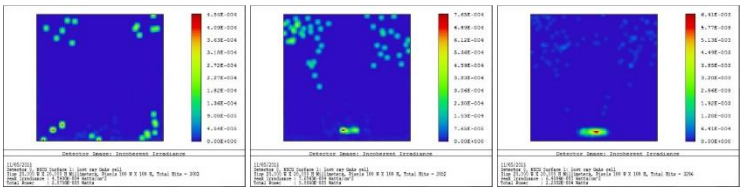

θ=0.6° θ=0.8° θ=1.0°

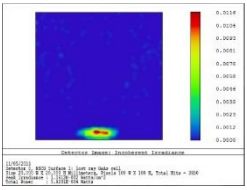

θ=1.2°

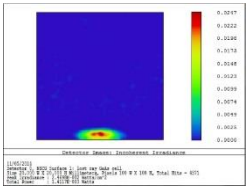

θ=1.5°

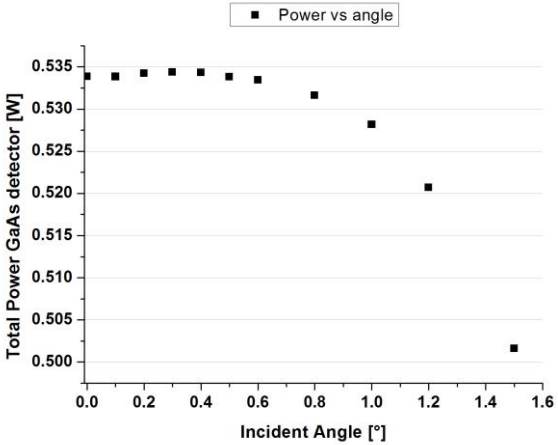
Power vs angle
Total Power GaAs detector [W]
0.535
0.530
0.525
0.520
0.515
0.510
0.505
0.500
0.0
0.2
0.4
0.6
0.8
1.0
1.2
1.4
1.6
Incident Angle [°]

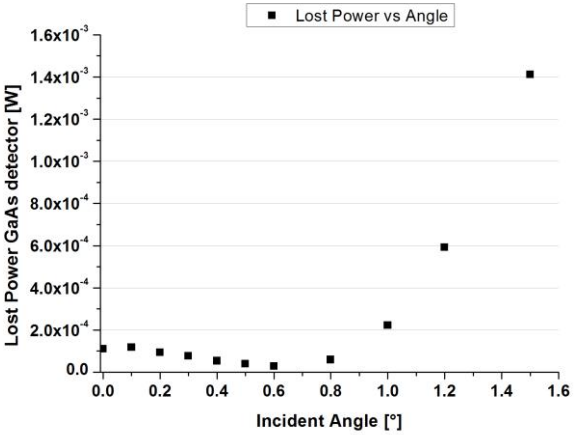

Figure IV-74. Power and lost power of "GaAs" ideal detector vs incidence angle with solar rod.

4.5.1.2.2 "Si" ideal detector

Table IV-33. Layout of ray tracing tilting angle on "Si" ideal detector with solar rod.

Layout "Si" ideal detector vs tilt acceptance angle		
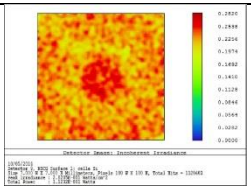	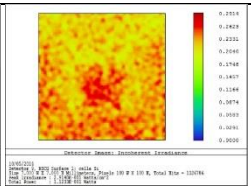	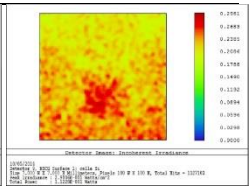
θ=0°	θ=0.1°	θ=0.2°

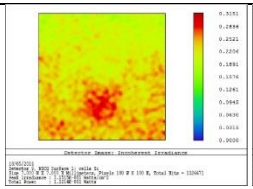
θ=0.3°

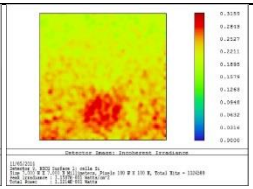
θ=0.4°

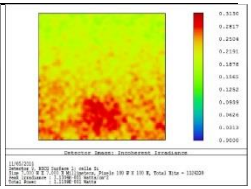
θ=0.5°

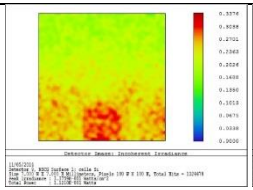
θ=0.6°

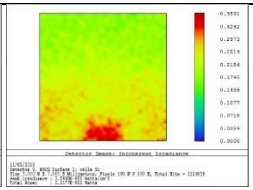
θ=0.8°

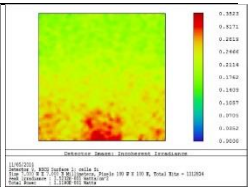
θ=1.0°

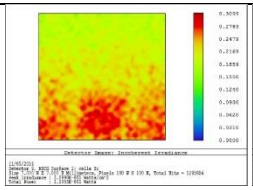
θ=1.2°

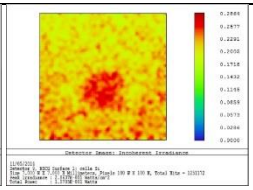
θ=1.5°

Table IV-34. Layout of ray tracing tilting angle on lost ray "Si" ideal detector with solar rod.

Layout lost ray "Si" ideal detector vs tilt acceptance angle		
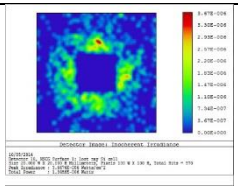	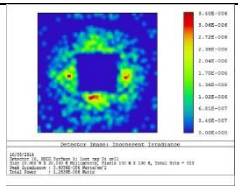	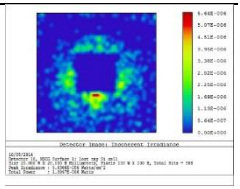
θ=0°	θ=0.1°	θ=0.2°

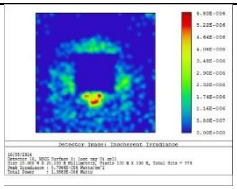

θ=0.3°

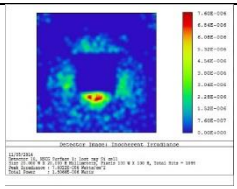

θ=0.4°

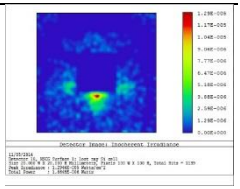

θ=0.5°

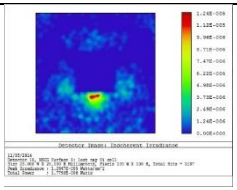

θ=0.6°

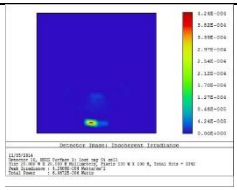

θ=0.8°

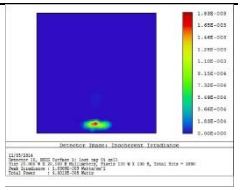

θ=1.0°

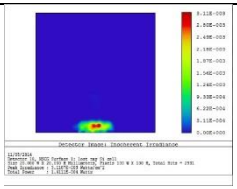

θ=1.2°

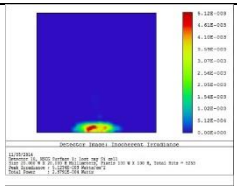

θ=1.5°

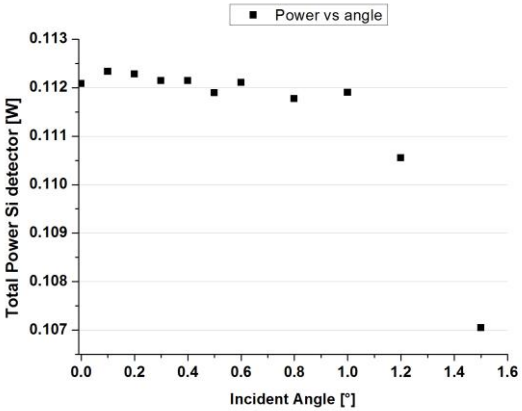

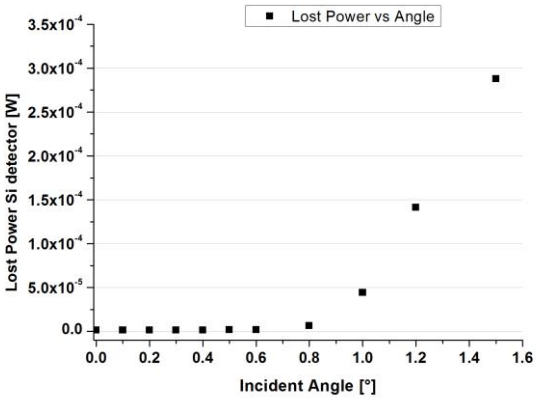

Figure IV-75. Power and lost power of "Si" ideal detector vs incidence angle with solar rod.

4.5.1.2.3 Total design system with solar rod

It is possible to highlight by optical simulations that the system has a good optical efficiency, equal to 64-65% up to a tilting lens angle of 0.8° (Figure IV-76 and Figure IV-71). Similarly, the optical loss in separation system maintain the optical efficiency up to an angle of 0.8° (Figure IV-77). The solar rod guides the light for internal reflection without losing part of it (Table IV-31) (Table IV-33).They are therefore indispensable to have a good distribution of solar radiation on the cells and to compensate the solar errors tracking about angles <1.0°.

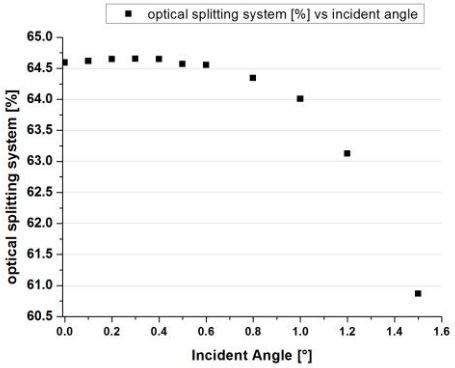

Figure IV-76. Optical splitting system efficiency with solar rod at different incident angle.

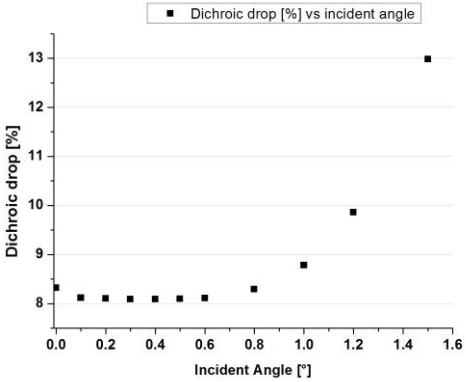

Figure IV-77. Dichroic drop efficiency with solar rod at different incident angle.

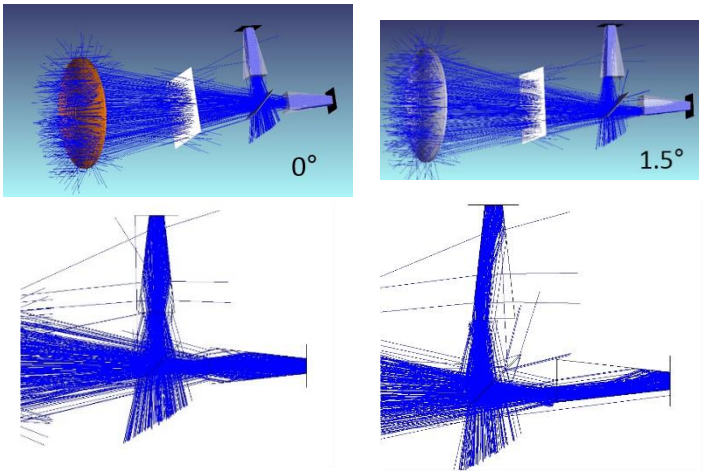

Figure IV-78. CPV system acceptance angle with solar rod: a) tilting angle θ=O°, b) tilting angle θ=1.5°.

4.5.2 CPV prototype system

Figure IV-79. CPV prototype spectra spitting system.

4.5.3 I-V-P Characteristic curve

The CPV prototype system was characterized to determine the electrical efficiency of the system. In particular, the characteristic I-V-P curves have been determined in order to quantify the electrical parameters of the photovoltaic cells (GaAs and Si) and therefore be able to quantify the efficiency of the system spectral separation in the two optical bands. In the reflected optical band the gallium arsenide cell response was characterized while in the transmitted optical band the silicon cell was characterized. The electrical response of the prototype system was compared with a commercial multi-junction cell of Spectrolab-Boeing.

4.5.3.1 Indoor measure SJSC (GaAs and Si cells)

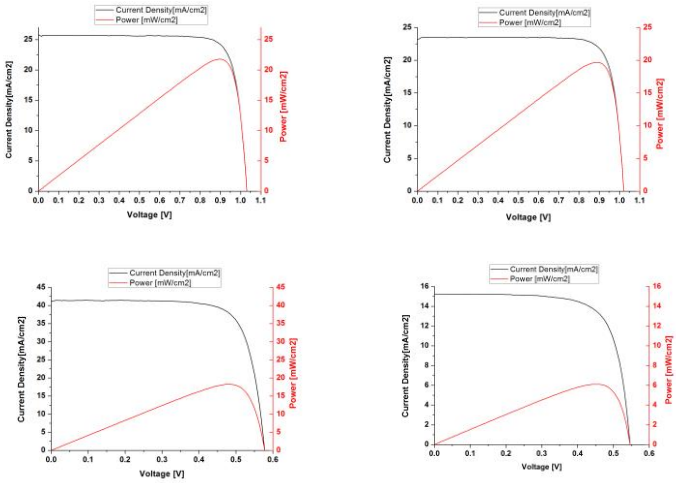

a) b)

Figure IV-80. I-V-P Indoor characteristic curve SJSC: a) GaAs-Si without dichroic, b) GaAs-Si with dichroic.

Table IV-35. I-V-P Indoor characterization of SJSC with and without dichroic mirror.

SJSC - Indoor Solar simulator					
	Si Cell	**Si Cell dichroic**	**GaAs Cell**	**GaAs Cell dichroic**	**Si-GaAs Cell dichroic**
V Open [V]	0.578	0.545	1.03	1.02	
J Short [mA/cm^2]	41.10	15.22	25.78	23.22	
FF [%]	76.60	73.50	83.50	83.10	
P max [mW/cm^2]	18.24	6.11	21.82	19.72	
η [%]	18.24 ± 0.08		21.80 ± 0.05		
η splitting [%]		6.10 ± 0.07		19.70 ± 0.06	**25.80 ± 0.10**

4.5.3.2 Indoor measure MJSC

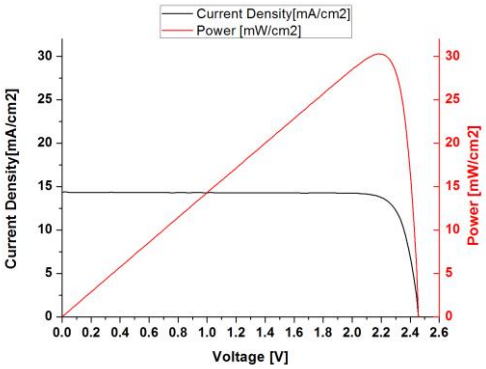

Figure IV-81. I-V-P Indoor characteristic curve MSJSC.

Table IV-36. I-V-P Indoor characterization of MJSC.

MISC – Indoor Solar simulator	
	MJSC Cell
V Open [V]	2.454
J Short [mA/cm^2]	14.38
FF [%]	85.90
P max [mW/cm^2]	30.30
η [%]	30.2 ± 0.1

4.5.3.3 Outdoor measure SJSC (GaAs and Si cells)

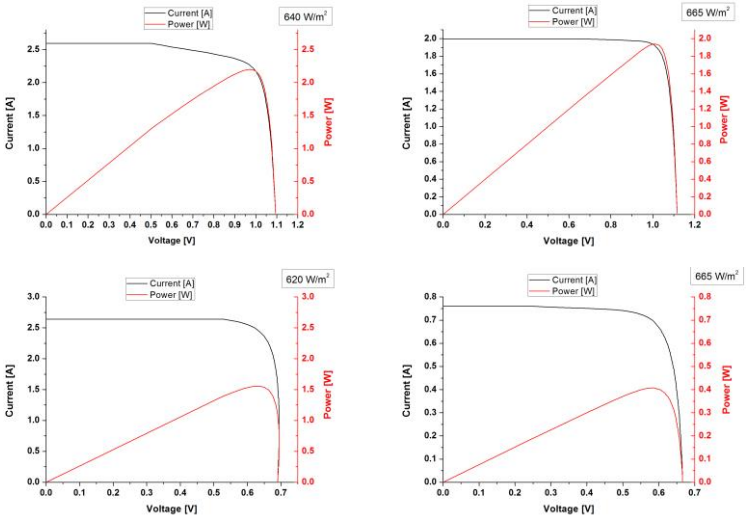

a) b)

Figure IV-82. I-V-P Outdoor characteristic curve SJSC: a) GaAs-Si without dichroic, b) GaAs-Si with dichroic.

Table IV-37. I-V-P Outdoor characterization of SJSC with and without dichroic mirror.

SJSC - Outdoor I-V-P Lens ø= 150mm EFL=254mm f/#1.7					
	Si Cell	**Si Cell dichroic**	**GaAs Cell**	**GaAs Cell dichroic**	**Si-GaAs Cell dichroic**
V Open [V]	0.696	0.668	1.110	1.116	
I Short [A]	2.64	0.76	2.42	1.998	
FF [%]	84.63	80.20	83.0	87.00	
P max [W]	1.56	0.41	2.22	1.94	
η [%]	14.3 ± 0.3	3.4 ± 0.2	17.5 ± 0.2	16.1 ± 0.1	
η system [%]					**19.45 ± 0.20**

4.5.3.4 Outdoor measure MJSC

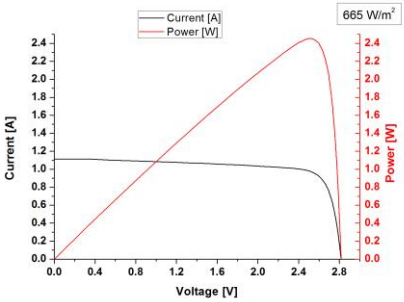

Figure IV-83. I-V-P Outdoor characteristic curve MJSC.

Table IV-38. I-V-P Outdoor characterization of MJSC.

MJSC - Outdoor I-V-P Lens ø= 150mm EFL=254mm f/#1.7	
	MJSC Cell
V Open [V]	2.883
I Short [A]	1.114
FF [%]	77.78
P max [W]	2.44
η system [%]	21.1 ± 0.2

4.5.3.5 Outdoor I-V-P daily measure

An efficiency characterization was conducted on a daily concentration systems with multijunction and with spectral separation at f/number 1.7 and 2, with and without solar rod. In t Figure IV-84 and Figure IV-85, it is possible to note the comparison between the different concentration systems.

Table IV-39. Experimental results daily efficiency of CPV systems without solar rod.

Lens ø= 150mm EFL=254mm			
	CPV - MJSC	**CPV splitting f/1.7**	**CPV splitting f/2**
η system [%]	20.70 ± 1.80	19.70 ± 0.70	20.00 ± 0.90

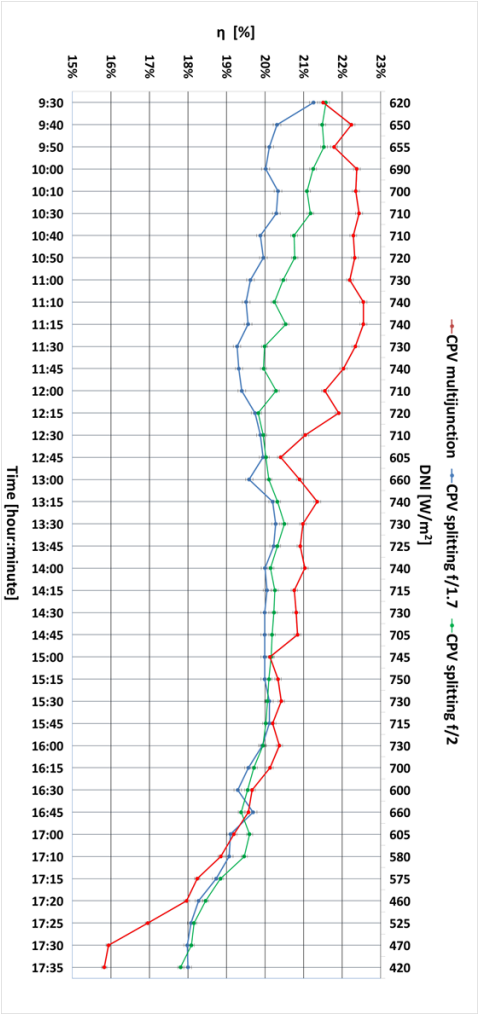

Figure IV-84. Daily efficiency system, CPV multijunction and CPV splitting system with f/number 1.7 and 2.

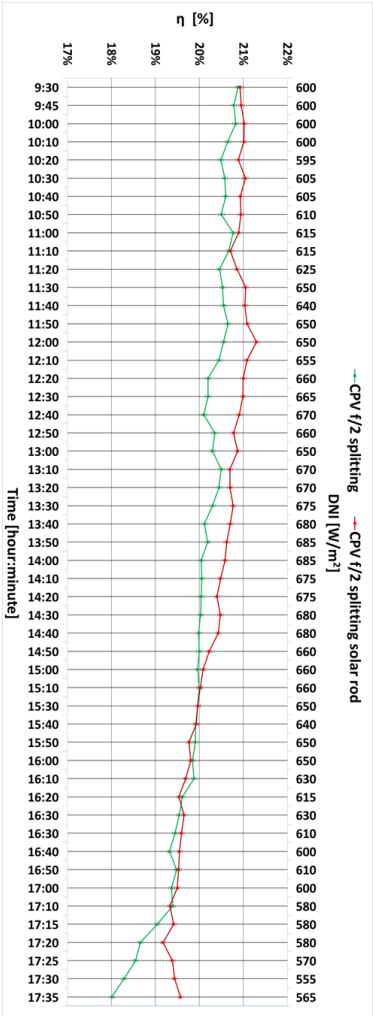

Figure IV-85. Daily efficiency system CPV splitting system with f/number 1.7 and 2 with solar rod.

Table IV-40. Experimental results daily efficiency of CPV systems with solar rod.

	Lens ø= 150mm	
	CPV splitting f/2 solar rod	**CPV splitting f/2**
η [%]	20.4 ± 0.6	20.0 ± 0.7

It was also evaluated the experimentally of the efficiency CPV system with spectral separation with and without solar rod. In Figure IV-86, it is shown how the CPV system with solar rod maintains high efficiency at tilting angles up to 0.7°- 0.8° while the system without solar rod has a drop of efficiency after 0.3°.

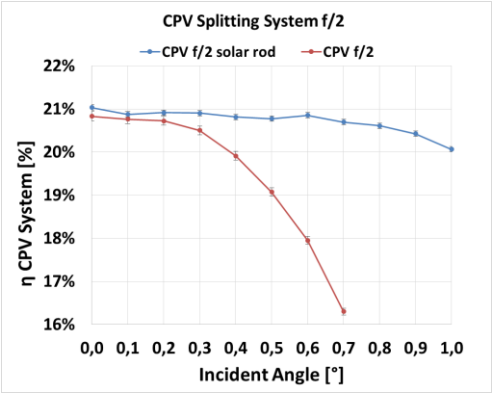

Figure IV-86. CPV splittin system f/2 with and without solar rod at different incident angle.

4.5.4 Thermal measurements with the spectral separation

During the research on concentrating photovoltaic system, we have undertaken the thermal analysis of the photovoltaic cells in solar concentration [109].

The analysis was carried out by simulating the photovoltaic cells with a known material of aluminum in order to determine the temperature inside the sample with a thermocouple and outside the sample with thermographic analysis.
In particular for thermographic analysis a calibrated emissivity equal to ε = 0.93 was used that has allowed detecting the temperature in function of exposure time to solar radiation.

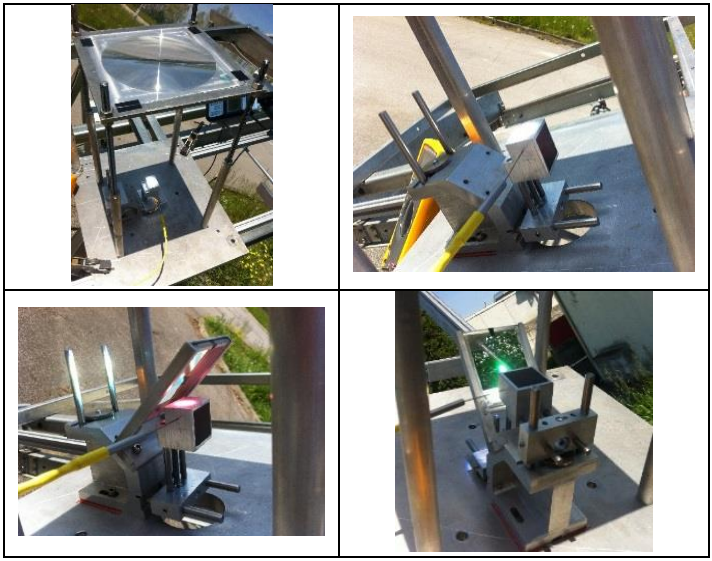

Figure IV-87. CPV prototype to evaluate the temperature on the cells.

In the Figure IV-88 is highlighted the thermal evolution of the silicon cell directly exposed to the solar radiation. There is a Fresnel lens concentrator with a diameter of 150 mm. The temperature achieved after 30 minutes is rnearly equal to 70°C both from thermocouple and from thermographic measurements.

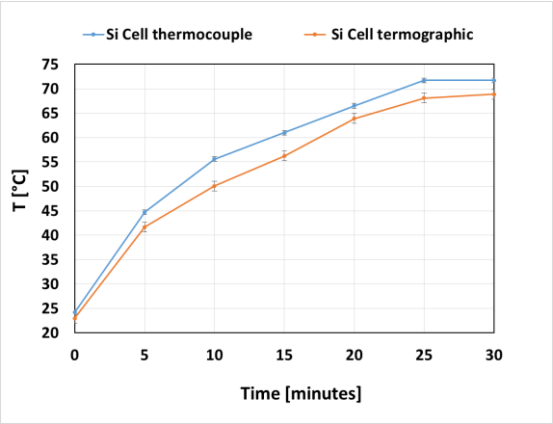

Figure IV-88. Temperature as a function of time of exposure of the silicon cell. It was evaluated the temperature of the silicon and of gallium arsenide cells by using the spectral separation.

Figure IV-89 shows the temperature reduction of ≈ 45% for Si cell and ≈ 30% of GaAs cell. This result shows as the dichroic filter allows to splitted the thermal contribution on the PV cell. The dichroic mirror therefore also being able to thermal selective filter.

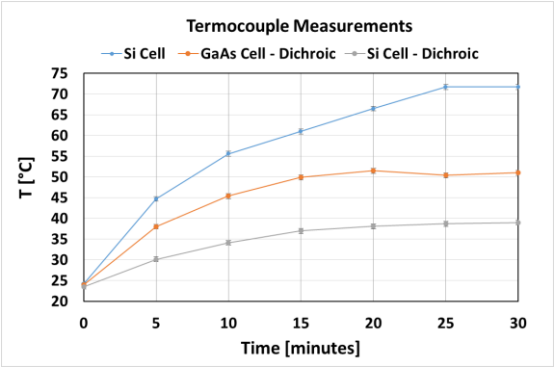

a)

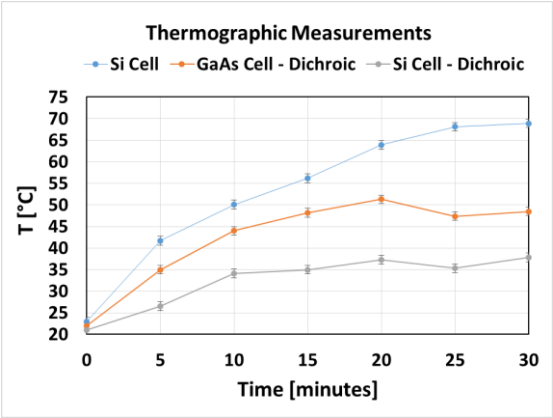

b)

Figure IV-89. Temperature as function of exposure time on Si and GaAs cell with dichroic filter, a) thermocouple measurements, b) thermographic measurements.

Chapter V

Conclusions and Future perspectives

Conclusion of Optical Multilayer filter

The optical materials in multilayer spectral separation were characterized to extrapolate the salient features needed for design and realization. The multilayer is composed of an optical substrate on witch make up a stacking of thin film layers that realize the coating.

The optical substrates such as sapphire, quartz and glass, are analyzed with analytic function to extrapolate the refractive index and the extinction coefficient.

The SiO_2 and TiO_2 single layers coatings were analyzed by a dispersion functions that model the optical transmittance and the reflectance of the experimental curves. An accurate statistical evaluation of the thickness by the atomic force microscopy (AFM) measurements, has allowed to obtain excellent results of correlation between the optical experimental measurements and the optical modeling response.

The refractive index of SiO_2 is 1.49 at 550 nm while for TiO_2 material is equal to 2.5 at 550 nm.

The atomic force microscope analysis allowed to determine the surfaces morphology of the thin films, emphasizing that the quadratic and algebraic roughness values are less than 4nm for TiO_2 and less than 2nm for SiO_2 thin films.

This indicate how the PVD magnetron sputtering technique deposition realize good quality surfaces and emphasize the separation of interfaces. This results

improve the multilayer optical response and decrease the scattering of the optical dispersion phenomena.

Compositional conclusion of multilayer thin film

The Rutherford Back Scattering (RBS) analysis on the single layers coating enfatize the stoichiometry ratio of O/Si equal to 2.02 and O/Ti equal to 2.03.
The analysis of the stoichiometry ratio has allowed identifying the optimal set point voltage deposition necessary to calibrate the deposition system. The reactive sputtering technology requires a very accurate control of oxygen flow. The calibration of voltage deposition oin the reactive sputtering allows to obtain a reliable and reproducible process.
The RBS analysis on the single layer has enabled to evaluate the homogeneity of deposition that determines the maximum area where to obtain uniform coatings.
The vacuum deposition system is composed of a rotating sample holder where the homogeneity of deposition is not uniform along the rotation axis.
Respect to a maximum distance of ±10cm from the center of the target deposition, the uniformity of deposition is equal to ±3%

Optical multilayer design allows to simulated antireflection and dichroic filters with high optical transmission or refraction efficiency with a low number of layers.
In particulary the dichroic design selected for the aim of this research activity has a number of layers equal to 21 with optical efficiency more than 90% in the two predefined optical bands.

Crystallographic conclusion of TiO_2

The multilayer have not a unique correlation between the optical design and experimental measurements. This effect is underline in the antireflection multilayers but is so much pronunced in dichroic mirrors.

In order to analyze this discrepancy detected, it was necessary to perform annealing treatment at the temperature of 350°C for 12 hours for the antireflection coatings and 24 hours for the dichroic mirrors.
The FT-IR spectroscopy analysis carried out on the thin films of TiO_2 at temperatures from 300°C to 350°C has shown the evolution in the spectrum of assorbance of the Ti-O-Ti at the wave number equal to 436cm^{-1}.
It appears evident that increasing annealing temperature there is a distinct phase transformation of TiO_2 from amorphous to crystalline phase.
This is also emphasized an estimate of the FWHM at various temperatures, with a value of 282 cm^{-1} for amorphous phase and 35cm^{-1} for the crystalline phase, due to a process of nucleation and growth of the material.
The phase variation from amorphous and crystalline titanium dioxide is also carried out by the high resolution X-Ray diffraction analysis on the samples as-deposited and heat treated.
The XRD spectrum of the TiO_2 thin film untreated presents a spread-spectrum index of a purely amorphous phase and a characteristic peak attributable to the rutile phase at $2\theta=27.3°$ (110) and $2\theta=53.57°$ (211).
The spectrum of the thermally treated sample shows characteristic peaks at $2\theta=25.4°$ (101) or $2\theta=48.2°$ (200) of the anatase phase. Do not appear in the sample instead of the thermally trattated crystallographic planes of rutile phase after heat treatment. Is to hypothesize an absorption of a rutile phase in the anatase phase that is stable in the temperature range between 350°C and 700°C.
The crystallographic size calculated by Debye-Scherrer equation on the more intense peak (101) of the anatase phase is equal to D=29nm.

Optical multilayer conclusion after annealing treatment

The antireflection and dichroic filters before annealing treatment showed no-correlation between the simulated spectrum and the real optical measurement. In particulary the variation of the as-deposited optical multilayers transmittance decreases linearly with increasing total thickness of the titanium dioxide. The optical transmission varying from a value of T=89% for a thickness equal to 53nm up to T=25% to a total thickness of TiO_2 equal to 716nm.

These multilayer filters after the annealing treatment exhibit optical responses comparable with the optical design, emphasizing the good correlation between the materials designed and reproducibility of the deposition process.

The optical design of the SiO_2 and TiO_2 alternating stacking layers is cheked also by scanning electron microscope (SEM) technique, analizing the multilayer in cross section images. It can be observe the quality of the layers interfaces and quantify a few thicknesses of the layers or the total thickness of the multilayer.

The correction between optical measurements before and after heat treatment is also shown by the thickness variation quantified by the AFM analysis.
This analysis demonstrating as the total multilayer thickness decreasing after annealing treatment highlighting a better correlation with the design project. A slight shift of the spectra is also highlighted by RBS analysis before and after annealing. This is justified by a slight thickness variation.

The optical constants of the TiO_2 material vary with the treatment of annealing at 350°C. In particular, the refractive index decrease from the compound phase to the anatase phase from a value of 2.5 to 2.44 at 550nm. The extinction coefficient decreases from the compaund to the anatase phase.
This is to promote the best transmitted optical responses in dichroic filters.

Conclusion of Concentrating Photovoltaic (CPV) prototype system

Among the many applications of optical interference filters it was analyzed and realized a concentrating photovoltaic system (CPV) using a dichroic filter. This prototype system has a multidisciplinary activity that range from the optical design, the solar tracking system, the electrical characterization, and the evaluation of the thermal component on the PV cells.
Analyzing the spectral response of the Silicon (Si) and Gallium Arsenide (GaAs) cells, it has been designed a dichroic filter to optically match these cells.

The analysis of external quantum efficiency of the cells allow to cover a higher range of wavelengths. The choice of the silicon cell is mainly due to the cost much lower than the cells III-V.
The separation system is designed as the reflected optical band ($350nm<\lambda<850$ nm) to GaAs cell, and the transmitted optical band ($950nm<\lambda<1200nm$) to Si cell.

Conclusion of Ray Tracing design

The ray tracing design has allowed to use non-imaging Fresnel lens, primary optics concentration element (POE), by witch to obtain the optical geometries to be used in prototyping phase.
With particular attention was analyzed and evaluated the optical matching between the Fresnel lens and the dichroic filter.
The more desirable optical coupling is result a slow type Fresnel lens that have high f-number between 1.7 and 2.0. The f-number symbolize the ratio between focal point and lens diameter of the Fresnel lens.
The POE optical lens of the system with f-number=2.0 have an efficiency equal to 67%. The ray tracing software design focus the radiation directly on the ideal detectors that simulate the PV surfaces cells.

The spot diagrams of the optical simulation show that there is a greater concentration of solar radiation in the central area of the PV cell. These provides a gradient of light on the PV cell.
The dichroic filter is designed to separate an incoming parallel light beam on the surface at 45° of the multilayer coating. If such radiation is incident on the surface with a conical geometry given by Fresnel lens focusing, the dichroic filter changes the optical response in terms of edge cutting wavelength and optical efficiency of the two separated optical bands.
The optical design of the prototype system has been fully performed by simulating an angular misalignment of the solar tracking system. The results show that the optical efficiency of the system decreases drastically for a skew angle greater than 0.4°.

It was completed a ray tracing design by inserting a solar rod, a secondary optics element (SOE) between the dichroic filter and the photovoltaic cells.

The solar rod allow as illustrated by spot diagrams, to uniform the solar radiation on photovoltaic cells. The solar rod increase the misalignment angle of the tracking system up to 0.8°, with a transmission efficiency of optical system equal to 64.5%.

Conclusion of prototype I-V-P characteristic curve and thermal characterization

The dichroic separation system was compared with a high-efficiency multi-junction cell.
As a first comparison were characterized by indoors measures of characteristic I-V-P curves by using a solar simulator.
These measurements have shown the indoor cell efficiency measured at standard conditions of 25°C and 1000W/m^2.
The indoor measures have shown that the multi-junction cell has an efficiency of 30.2 ± 0.1%, while the splitting system GaAs-Si has an efficiency of 25.8 ± 0.1%.
Through outdoor measurements, it was possible to compare the multi-junction system and prototype separation system using the same concentration lens.
The I-V-P characteristic curves measured, taking into account to quantify the input power, have allowed to extrapolate the efficiency system under the concentration with an f-number =1.7.
The concentration system with multi-junction cell has an efficiency of 21.10 ± 0.20%, while the separation system has an efficiency of 19.45 ± 0.15%.
The different CPV systems were measured by conducting a daily measures to show the trend of efficiency during the day.
The multi-junction concentration system presents an efficiency of 20.70 ± 1.80%, while the splitting concentration system with f/1.7 presents an efficiency of 19.70 ± 0.70%.
Was also measured the daily trend efficiency of a splitting concentration system that have the same concentration but with a f/number equal to 2, and it showed an efficiency of 20.10 ± 0.90%.
It can be seen that the multi-junction CPV system although having a higher average efficiency but shows a double deviation standar data than CPV splitting systems. This means that the CPV splitting systems is more constant

throughout the day, especially towards the evening hours when the solar radiation decreases.
Finally are compared two CPV splitting system with and without solar rod that have the same f/number equal to 2.
The CPV system with solar rod shows an average efficiency of 20.40 ± 0.60 greater than the system without solar rod of 20.00 ± 0.70.
This is likely due to a better solar radiation distribution on the surface of the PV cells and a lower optical loss-ray on the PV cells.
It has been verified experimentally the maximum tilt angle of the CPV splitting system such as to maintain high efficiency.
The CPV system with solar rod has a limit tilt angle of 0.7°- 0.8°, while the CPV system without solar rod shows a loss in efficiency for angles greater than 0.3°- 0.4°.
These results highlights as the CPV prototype splitting system with solar rod can allow a greater misalignment. Therefore it can be used a simpler and cheaper solar tracking system.

Finally, it evaluated the thermal component on the solar cells ensue by the solar concentration.
The PV cell was simulated by a bulk material as aluminum, which has been struck directly by the concentrated radiation and measuring the temperature reached after 30 minutes of exposure.
Within the material, the temperature of about 71°C was detected with a thermocouple, while on the surface the temperature equal to 69°C was measured by an infrared camera.
The temperature was measured on the same sample by using the dichroic filter in the two optical bands.
The temperature reduction on the Si cell in the transmitted band is equal to 45% that corresponds to a temperature of about 39°C. The GaAs cell in the reflected band have a reduction of temperature about 30% that corresponds to a temperature of 51°C.
This temperature reduction given by the splitting effect of the dichroic filter is confirmed both thermocouple and thermographic measures.
One can conclude therefore that the dichroic filter is also a temperature selective filter. The temperature reduction enables to limit the electrical losses of the PV cells induced by the heating.

This splitting effect removes the wavelengths of light that are not photo converted by the PV cell avoiding thermal overheating. The PV cells therefore using the spectral separation can be exposed to higher concentrations ratios.

General conclusions and Future perspectives

Considering the promising results and evaluating the international research about the spectral separation applied to photovoltaic systems is possible to think that this technology may be applied in future energy production plants.

Of particular interest is certainly the research on the performance of PV cells. It will be important to use materials with energy gap adaptable to the optical bands obtained in the splitting process of sunlight.
An important development to increase the CPV optical efficiency systems it using high performance materials and technologies production will be to obtain complex optical geometries as for Fresnel lens.
It will be important to optimize the dichroic filters design, combined by performance materials, will obtain more efficient and accurate spectral separations in two or more optical bands.
A better spectral separation matched with dedicated photovoltaic cells will convert more wavelengths of the solar spectrum, which will raise the overall efficiency.

References

[1] R. McConnell e V. Fthenakis, «Concentrated Photovoltaics,» in *Third Generation Photovoltaic*, USA, Intech, 2012, pp. 167 - 181.

[2] S. P. Philipps, F. Dimroth e A. W. Bett, «Chapter IC-6 HIgh Efficiency III–V Multijunction Solar Cells,» in *Solar Cells (Second Edition) - Material, Manufacture and Operation*, Elsevier, 2013, pp. 353 - 381.

[3] R. Swanson, «The promise of concentrators,» *Progress in Photovoltaic: Research and Application*, vol. 8, pp. 93 - 111, 2000.

[4] P.-G. Autumn, «Quantifying the Environmental Impact of CPV,» in *EPIA International Conference on CPV*, Munich, Germany, 2010.

[5] H. Lerchenmüller, «An industry point of view on the current CPV market,» in *EPIA CPV Conference*, Munich, Germany, 2010.

[6] L. E. Chaar, L. lamont e N. E. Zein, «Review of photovoltaic technologies,» *Renewable and Sustainable Energy Reviews*, vol. 15, pp. 2165 - 2175, 2011.

[7] European Photovoltaic Technology Platform, «A Strategic Research Agenda for Photovoltaic Solar Energy Technology, Edition 2,» in *26th European PV Solar Energy Conference and Exhibition* , Hamburg, 2011.

[8] S. P. Philipps, A. W. Bett, K. Horowitz e S. Kurtz, «CURRENT STATUS OF CONCENTRATOR PHOTOVOLTAIC (CPV) TECHNOLOGY,» in *CPV Report 1.1*, France, 2015.

[9] E. Jackson, «Areas for improvement of the semiconductor solar energy converter,» in *In Transactions of the conference on the use of solar energy*, Tuscan Arizona: University of Arizona, 1955.

[10] F. T. Welford e R. Winston, The optics non-imaging concentrators, New York: Academic Press, 1978.

[11] M. A. Green e A. Ho-Baillie, «Forty three per cent composite split-spectrum concentrator solar cell efficiency,» *PROGRESS IN PHOTOVOLTAICS: RESEARCH AND APPLICATIONS*, vol. 18, pp. 42 - 47, 2010.

[12] A. Imenes e D. Mills, «Spectral beam splitting technology for increased conversion efficiency in solar concentrating systems: a review,» *Solar Energy Materials & Solar Cells*, vol. 84, pp. 16 - 69, 2004.

[13] A. Mojiri, R. Taylor, E. Thomsen e G. Rosengarten, «Spectralbeamsplittingforefficient conversion of solarenergy—A review,» *Renewable and Sustainable Energy Reviews*, vol. 28, pp. 654 - 663, 2013.

[14] S. Rühle, A. Segal, A. Vilan, S. R. Kurtz, L. Grinis, A. Zaban, I. Lubomirsky e D. Cahen, «A two junction, four terminal photovoltaic device for enhanced light to electric power conversion using a low-cost dichroic mirror,» *JOURNAL OF RENEWABLE AND SUSTAINABLE ENERGY*, vol. 1, p. 013106, 2009.

[15] J. D. McCambridge, M. A. Steiner, B. L. Unger, K. A. Emery, E. L. Christensen, M. W. Wanlass, A. L. Gray, L. Talacs, R. Buelow, A. McCollum, J. W. Ashmead, G. R. Schmidt, A. W. Hass, J. R. Wilcox,

J. Van Meter, J. L. Gray, D. T. Moore, A. M. Barnett e R. J. Schwartz, «Compact spectrum splitting photovoltaic module with high efficiency,» *PROGRESS IN PHOTOVOLTAICS: RESEARCH AND APPLICATIONS*, vol. 19, pp. 352 - 360, 2011.

[16] O. Z. Sharaf e M. F. Orhan, «Concentrated photovoltaic thermal (CPVT) solar collector systems: Part II – Implemented systems, performance assessment, and future directions,» *Renewable and Sustainable Energy Reviews*, vol. 50, pp. 1566 - 1633, 2015.

[17] A. Mojiri, C. Stanley, R. A. Taylor, K. Kalantar-zadeh e G. Rosengarten, «A spectrally splitting photovoltaic-thermal hybrid receiver utilising direct absorption and wave interference light filtering,» *Solar Energy Materials & Solar Cells*, vol. 139, pp. 71 - 80, 2015.

[18] F. Crisostomo, R. A. Taylor, D. Surjadi, A. Mojiri, G. Rosengarten e E. R. Hawkes, «Spectral splitting strategy and optical model for the development of a concentrating hybrid PV/T collector,» *Applied Energy*, vol. 141, pp. 238 - 246, 2015.

[19] D. Li, D. Wan, X. Zhu, Y. Wang, Z. Han, S. Han, Y. Shan e F. Huang, «Broadband antireflection TiO2–SiO2 stack coatings with refractive-index-grade structure and their applications to Cu(In,Ga)Se2 solar cells,» *Solar Energy Materials & Solar Cells*, 2014.

[20] J. Musil, P. Baroch, J. Vlcek, K. Nam e J. Han, «Reactive magnetron sputtering of thin films: present status and trends,» *Thin Solid Films*, vol. 475, pp. 208 - 218, 2005.

[21] J. M. e. M. N. W.K. Chu, «Backscattering Spectrometry,» *Academic Press*, 1978.

[22] S. S. Cetin, S. Corekci, M. Cakmak e S. Ozcelik, «Structural investigation and electronic band transitions of nanostructured TiO2 thin films,» *Cryst. Res. Technol.*, vol. 46, p. 1207 – 1214, 2011.

[23] Y. Leprince-Wang e K. Yu-Zhang, «Study of the growth morphology of TiO thin films by AFM and TEM,» *Surface and Coating Tecnology*, vol. 140, pp. 155-160, 2001.

[24] C. Pecharromàn, F. Gracìa, J. P. Holgado, M. Ocana e A. R. Gonzalez-Elipe, «Determination of texture by infrared spectroscopy in titanium oxide-anatase thin films,» *Journal Applied Physics*, vol. 93, n. 4634, 2003.

[25] F.-M. Liu e T.-M. Wang, «Surface and optical properties of nanocrystalline anatase titania films grown by radio frequency reactive magnetron sputtering,» *Applied Surface Science*, vol. 195, pp. 284 - 290, 2002.

[26] Y.-Q. Hou, D.-M. Zhuang, G. Zhang, M. Zhao e M.-S. Wu, «Influence of annealing temperature on the properties of titanium oxide thin film,» *Applied Surface Science*, vol. 218, pp. 97 - 105, 2003.

[27] B. Zhao, J. Zhou, . Y. Chen e Y. Peng, «Effect of annealing temperature on the structure and optical properties of sputtered TiO2 films,» *Journal of Alloys and Compounds*, vol. 509, pp. 4060 - 4064, 2011.

[28] D. Chiaroni, V. Chiesa, F. Frattini, «A comparison between Italy and Other European Countries,» in *Renewable Energy Generation: Incentives Matter*, Butterworth-Heinemann an imprit of Elsevier, 2014, pp. 347-367.

[29] Il Ministro dello sviluppo economico, «Quarto conto energia,» Il Ministro dello sviluppo economico, Italia, 2011.

[30] Horne, S., «Concentrating photovoltaic (CPV) system and applications,» in *Concentrating Solar Power Technology*, SolFocus Inc., USA, 2012, pp. 323 - 361.

[31] H. Cotal, C. Fetzer, J. Boisvert, G. Kinsev, R. King, P. Hebert, H. Yoon e N. Karam, «III–V multijunction solar cells for concentrating photovoltaics,» *Energy & Environmental Science*, vol. 2, p. 174–192, 2009.

[32] D. M. A.G. Imenes, «Spectral beam splitting technology for increased conversion efficiency in solar concentrating systems: a review,» *Solar Energy Materials & Solar Cells*, vol. 84, pp. 19 - 69, 2004.

[33] R. Moon, L. James, H. Vander Plas, T. Yep, G. Antypas e Y. Chai, «Multigap solar cell requirements and the performance of AlGaAs and Si cells in concentrated sunlight,» in *Proceedings of the 13th IEEE Photovoltaic Specialists Conference*, Washington DC, USA, 1978, pp. 859 - 867.

[34] K. Xiong, S. Lu, J. Dong, T. Zhou, D. Jiang, R. Wang e H. Yang, «Light-splitting photovoltaic system utilizing two dual-junction solar cells,» *Solar Energy*, vol. 84, pp. 1975 - 1978, 2010.

[35] L. Fraas, J. Avery, H. Huang, L. Minkin e E. Shifman, «Demonstration of a 33% efficient Cassegrainian solar module,» in *Proceedings of the 4th World Conference on Photovoltaic Energy Conversion*, Waikoloa, Hawaii, USA, IEEE, 2006, pp. 679 - 682.

[36] B. Mitchell, G. Peharz, G. Siefer, M. Peters, T. Gandy, J. C. Goldschmidt, J. Benick, S. W. Glunz, A. Bett e F. Dimroth, «Four-junction spectral beam-splitting photovoltaic receiver with high optical efficiency,» *PROGRESS IN PHOTOVOLTAICS: RESEARCH AND APPLICATIONS*, vol. 19, pp. 61 - 72, 2011.

[37] A. Antonin, M. A. Butturi, P. Zurru, M. Norton e A. Parretta, «Development of a high/low concentration photovoltaic module with dichroic spectrum splitting,» *PROGRESS IN PHOTOVOLTAICS: RESEARCH AND APPLICATIONS*, vol. 23, pp. 1190 - 1201, 2015.

[38] A. Barnett, D. Kirkpatric, C. Honsberg, D. Moore, M. Wanlass, K. Emery, R. Schwartz, D. Carlson, S. Bowden, D. Aiken, A. Gray, S. Kurtz, L. Kazmerski, M. Steiner, J. Gray, T. Davenport, R. Buelow, L. Takacs, N. Shatz, J. Bortz, O. Jani, K. Goossen, F. Kiamilev, A. Doolittle, I. Ferguson, B. Unger, G. Schmidt, E. Christensen e D. Salzman, «Very high efficiency solar cell modules,» *PROGRESS IN PHOTOVOLTAICS: RESEARCH AND APPLICATIONS*, vol. 17, pp. 75 - 83, 2009.

[39] X. Wang, N. Waite, P. Murcia, K. Emery, M. Steiner, F. Kiamilev, K. Goossen, C. Honsberg e A. Barnett, «Lateral spectrum splitting concentrator photovoltaics: direct measurement of component and submodule efficiency,» *PROGRESS IN PHOTOVOLTAICS: RESEARCH AND APPLICATIONS*, vol. 20, pp. 149 - 165, 2012.

[40] E. Kintisch, «LIGHT-SPLITTING TRICK SQUEEZES MORE ELECTRICITY OUT OF SUN'S RAYS,» *Solar Power - Science* , vol. 317, n. 5838, pp. 583 - 584, 2007.

[41] V. Kumar, R. Shirivastava e S. Untawale, «Fresnel lens: A promising alternative of reflectors in concentrated solar power,» *Renewable and Sustainable Energy Reviews*, vol. 44, pp. 376-390, 2015.

[42] D. Miller, M. Kempe, C. Kennedy e S. Kurtz, «Analysis of Transmitted Optical Spectrum Enabling Accelerated Testing of CPV Designs,» in *Solar Energy Tecnology Conference*, San Diego, California, 2009.

[43] H. Baig, K. C. Heasman e T. K. Mallick, «Non-uniform illuminationinconcentratingsolarcells,»

RenewableandSustainableEnergyReviews, vol. 16, pp. 5890 - 5909, 2012.

[44] H. Baig, N. Sellami e T. K. Mallick, «Trapping light escaping from the edges of the optical element in a Concentrating Photovoltaic system,» *Energy Conversion and Management*, vol. 90, pp. 238 - 246, 2015.

[45] G. Segev e A. Kribus, «Performance of CPV modules based on vertical multi-junction cells under non-uniform illumination,» *Solar Energy*, vol. 88, pp. 120- 128, 2013.

[46] D. C. Carter, D. Sproul e D. J. Christie, *Effective Control for Reactive Sputtering Processes*, Vacuum tecnology & coating, 2006.

[47] D. M. Mattox, Handbook of Physical Vapor Deposition (PVD) Processing, Albuquerque, NM: Management Plus, Inc., 2010.

[48] D. Pelleymounter, D. Christie e . B. Fries, *Pulsed DC Power for Magnetron Sputtering: Strategies for Maximizing Quality and Flexibility*, Fort Collins, CO: Advanced Energy Industries, Inc., 2014.

[49] D. M. Mattox, «Physical Vapor Deposition Processing,» in *Metal Finishing*, Society of Vacuum Coaters, 2002, pp. 394-408.

[50] L. Lou, G. MacDonough, H. Walde, D. Carter, G. Roche e R. Scholl, «Closed loop controlled reactive dual magnetron sputtering,» *Advance Energy Industries*.

[51] Society of Vacuum Coaters, *Tutorial Course: The Practice of Reactive Sputtering*, Garmisch Partenkirchen: SVC, 2010.

[52] H. Macleod, Thin-FIlm Optical Filters, second edition, Bristol: IOP Publishing, Dirac House, 2001.

[53] J. Yao, . J. Shao, H. He e Z. Fan, «Effects of annealing on laser-induced damage threshold of TiO2/SiO2 high reflectors,» *Applied Surface Science*, vol. 253, pp. 8911 - 8914, 2007.

[54] M. Hasan, A. Haseeb, R. Saidur, H. Masjuki e M. Hamdi, «Influence of substrate and annealing temperatures on optical properties of RF-sputtered TiO2 thin films,» *Optical Materials*, vol. 32, pp. 690 - 695, 2010.

[55] Roditi, «www.roditi.com,» [Online]. Available: http://www.roditi.com/SingleCrystal/Sapphire/C-Plane.html.

[56] crystran, «http://www.crystran.co.uk/,» [Online]. Available: http://www.crystran.co.uk/userfiles/files/optical-glass-n-bk7-data-sheet.pdf.

[57] J. Kardellis e M. Kapsali, «Simulating the dust effect on the energy performance of photovoltaic generators,» *Energy*, vol. 36, pp. 5154-5161, 2011.

[58] O. Stelzen, V. Hopfe e P. Klobes, «Determination of optical parameters for amorphous thin film materials on semi-transparent substrates from transmittance and reflectance measurements,» *Journal of Physics D: Applied Physics*, vol. 24, pp. 2088-94, 1991.

[59] E. Nichelatti, «Complex refractive index of a slab from reflectance and transmittance: analytical solution,» *JOURNAL OF OPTICS A: PURE AND APPLIED OPTICS*, vol. 4, pp. 400-403, 2002.

[60] M. Ashar, F. Placido e S. Naseem, «Characterization of reactively evaporeted TiO2 thin films as high and medium index layers for optical application,» *The European Physical Journal Appyied Physics*, vol. 35, pp. 177-184, 2006.

[61] A. Forouhi e I. Bloomer, «Chapter 7 – Calculation of Optical Constants, n and k, in the Interband Region,» in *Handbook of Optical Constants of Solids, Volume 2*, Academic Press, 1998, p. Pages 151–175.

[62] W. Raniero, G. Della Mea e M. Campostrini, «Functionalization of surfaces with optical coatings produced by PVD magnetron sputtering,» *IGI Global*, 2015.

[63] Thin film design software (TF-Calc) Version 3.5, Software Spectra, Inc. Portland, OR 97229 USA, <www.sspectra.com>.

[64] S. S. Inc., «http://www.sspectra.com/,» [Online]. Available: http://www.sspectra.com/support/index.html.

[65] H. A. Muhammad, S. Muhammad, F. Placido e N. Shahzad, «Modeling and preparation of pratical optical filters,» *Current Applied Physics*, vol. 9, pp. 1046-1053, 2009.

[66] R. R. Willey, Pratical Production of Optical Thin Films, second edition, Charlevoix USA: Willey Optical Consultants.

[67] R. R. Willey, Pratical Design of Optical Thin Films, third edition, Charlevoix USA: Willey Optical Consultants.

[68] Cvimellesgriot, «www.cvimellesgriot.com,» [Online]. Available: http://cvilaseroptics.com/Frontend/PDFs/optical_coatings.pdf.

[69] R. Winston e J. O'Gallagher, «Nonimaging Concentrator (Optics),» in *Encyclopedia of Physical Science and Technology (Third Edition)*, 2003, pp. 507-522.

[70] D. C. Lainè, «Transmissive, non-imaging Fresnel Types of reflective radiation concentrators revisited,» *Optics & Laser Tecnology*, vol. 54, pp. 274-283, 2013.

[71] G. Segev e A. Kribus, «Performance of CPV modules based on vertical multi-junction,» *Solar Energy*, vol. 88, pp. 120-128, 2013.

[72] T. K. Yew, K. K. Chong e B. H. Lim, «Performance study of crossed compound parabolic concentrator as secondary optics in non-imaging dish concentrator for the application of dense-array concentrator photovoltaic system,» *Solar Energy*, vol. 120, pp. 296-309, 2015.

[73] A. International, *ASTM G173-03(2012), Standard Tables for Reference Solar Spectral Irradiances: Direct Normal and Hemispherical on 37° Tilted Surface*, West Conshohocken, PA, 2012.

[74] Y. Yao, Y. Hu, S. Gao, G. Yang e J. Du, «A multipurpose dual-axis solar tracker with two tracking strategies,» *Renewable Energy*, vol. 72, pp. 88-98, 2014.

[75] B. Du, E. Hu e M. Kolhe, «Performance analysis of water cooled concentrated photovoltaic (CPV) system,» *Renewable and Sustainable Energy Reviews*, vol. 16, pp. 6732-6736, 2012.

[76] AKKUtrack, «www.akkutrack.com,» [Online]. Available: https://app.box.com/s/bo8p1eupy86yqdfh3ufhrnlfj7f104zj.

[77] S. Chander, A. Purohit, . A. Sharma, Arvind, S. Nehra e M. Dhaka, «A study on photovoltaic parameters of mono-crystalline silicon solar cell with cell temperature,» *Energy Reports*, vol. 1, pp. 104-109, 2015.

[78] M. E. Ya'acob, H. Hizam, M. Bakri A, M. Amran, M. Radzi, T. Khatic e A. Rahim, «Performance Test Conditions for Direct Temperature

Elements of Multiple PV Array configurations in Malaysia,» *Energy Procedia*, vol. 61, pp. 2387-2390, 2014.

[79] W. Raniero, M. Campostrini, G. Maggioni, G. Della Mea e A. Quaranta, «Physical vapour deposition reactive magnetron sputtering for the production and application of dichroics in photovoltaic system with solar spectral splitting,» *Applied Surface Science*, vol. 308, pp. 170-175, 2014.

[80] D. Pjevic, M. Obradovic, T. Marinkovic, A. Grce, M. Milosavljevic, R. Grieseler, T. Kups, M. Wilke e P. Schaaf, «Properties of sputtered TiO2 thin films as a function of deposition and annealing parameters,» *Physica B*, vol. 463, pp. 20-25, 2015.

[81] W. Raniero, G. Maggioni, G. Della Mea, M. Campostrini, S. Marigo e M. Nardo , «Rutherford Backscattering Spectrometry (RBS) analysis of dichroic systems for optical applications,» *AIP Conference Proceedings*, vol. 133, n. 1530, 2013.

[82] M. Mazur, D. Wojcieszak, J. Domaradzki, D. Kaczmarek, S. Song e F. Placido, «TiO2/SiO2 multilayer as an antireflective and protective coating deposited by microwave assisted magnetron sputtering,» *Opto-Electronics Review 21*, vol. 21, pp. 233-238, 2013.

[83] A. Imenes, D. Buie e D. McKenzie, «The design of broadband, wide-angle interference filters for solar concentrating systems,» *Solar Energy Materials & Solar Cells*, vol. 90, pp. 1579 - 1606, 2006.

[84] Y. Cui, j. Sun, Z. Hu, W. Yu, N. Xu, N. Xu, Z. Ying e J. Wu, «Synthesis, phase transition and optical properties of nanocrystalline titanium dioxide films deposited by plasma assisted reactive pulsed laser deposition,» *Surface & Coatings Technology*, vol. 231, pp. 180 - 184, 2013.

[85] D. Li, M. Carette, A. Granier, J. Landesman e A. Goullet, «Effect of ion bombardment on the structural and optical properties of TiO2 thin films deposited from oxygen/titanium tetraisopropoxide inductively coupled plasma,» *Thin Solid Films*, vol. 589, pp. 783 - 791, 2015.

[86] F. Hamelmann, U. Heinzmann, A. Szekeres, N. Kirov e T. Nikolova, «Deposition of silicon oxide thin films in teos with addition of oxigen to the plasma ambient: IR analysis,» *Journal of Optoelectronics and Advanced Materials*, vol. 7, n. 1, pp. 389 - 392, 2005.

[87] P. Vitanov, A. Harizanova e T. Ivanova, «Structural and dielectric properties of TiO2 thin films deposited by the sol-gel method on Si substrates,» *Journal ofPhysics*, vol. 356, 2012.

[88] M. Fallet, S. Perpoon, J. L. Deschanvres e M. Langlet, «Influence of physico-structural properties on the photocatalytic activity of sol-gel derived TiO2 thin film,» *Journal of Material Science*, n. 41, pp. 2915 - 2927, 2006.

[89] M. Horprathum, P. Eiamchai, P. Chindaudom, N. Nuntawong, V. Patthanasettakul, P. Limnonthakul e P. Limsuwan, «Characterization of inhomogeneity in TiO2 thin films prepared by pulsed dc reactive magnetron sputtering,» *Thin Solid Films*, vol. 520, pp. 272 - 279, 2011.

[90] J. DeLoach e C. Aita, «Thickness-dependent crystallinity of sputter-deposited titania,» *J. Vac. Sci. Technol. A*, vol. 13, p. n 3, 1998.

[91] P. Lobl, M. Huppertz e D. Mergel, «Nucleation and growth in TiO2 films prepared by sputtering and evaporation,» *Thin solid films*, vol. 251, pp. 72 - 79, 1994.

[92] X. Wanga, H. Masumoto, Y. Someno e T. Hirai, «Microstructure and optical properties of amorphous TiO2-SiO2 composite ®lms

synthesized by helicon plasma sputtering,» *J. Appl. Phys,* vol. 93, n. 4634, 2003.

[93] P. Singh e D. Kaur, «Room temperature growth of nanocrystalline anatase TiO2 thin films by dc magnetron sputtering,» *Physica B,* vol. 405, pp. 1258 - 1266, 2010.

[94] F. Yang, Y. Chu, L. Huo, Y. Yang, Y. Liu e J. Liu, «Preparation of uniform rhodamine B-doped SiO2/TiO2 composite Microsphe-res,» *Journal of Solid State Chemistry,* vol. 179, p. 457 – 463, 2006.

[95] E. Cetinorgu, N. Geron, S. Goldsmith e R. Boxman, «Phase determination of filtered vacuum arc deposited TiO2 thin films by optical modeling,» *Thin Solid Films,* vol. 518, pp. 1060-1066, 2009.

[96] T. Grzyb, M. Weclawiak e S. Lis, «Influence of nanocrystals size on the structural and luminescent properties of GdOF:Eu3+,» *Journal of Alloys and Compounds,* vol. 539, pp. 82 - 89, 2012.

[97] C. T. Wei e H. Shieh, «Optical and mechanical property changes in thin-film filters with post deposition thermal treatments,» *Japanese Journal of Applied Physics,* vol. 45, n. 3 A, pp. 1743 - 1787, 2006.

[98] C. Wang, Y. Jin, J. Shao e Z. Fan, «Influence of three post-treatment methods on properties of ZrO2 thin films,» *Journal of Laser,* vol. 10, n. 35, pp. 1600 - 1604.

[99] M. Sajjad Hussain, . M. Mehmood, J. Ahmad, M. Tauseef Tanvir, A. Faheem Khan , T. Ali e A. Mahmood , «RBS depth profiling and optical characterization of multilayers of TiO2 (20 nm) and Ge (15 nm),» *Materials Chemistry and Physics,* vol. 139, pp. 17-26, 2013.

[100] K. Jiang, A. Zakutayev, J. Stowers, M. D. Anderson, J. Tate, D. H. McIntyre, D. C. Johnson e . D. A. Keszler, «Low-temperature, solution processing of TiO2 thin films and fabrication of multilayer

dielectric optical elements,» *Solid State Sciences,* vol. 11, pp. 1692 - 1699, 2009.

[101] D. Pjević, M. Obradović, T. Marinković , A. Grce, M. Milosavljević, R. Grieseler, T. Kups, M. Wilke e P. Schaaf, «Properties of sputtered TiO2 thin films as a function of deposition and annealing parameters,» *Physica B,* vol. 463, pp. 20 - 25, 2015.

[102] Z. Wang, N. Yao e X. Hu, «Single material TiO2 double layers antireflection coating with photocatalytic property prepared by magnetron sputtering technique,» *Vacuum,* vol. 108, pp. 20 - 26, 2014.

[103] N. Martin, C. Rousselot, D. Rondot, F. Palmino e R. Mercier, «Microstructure modificationn of amorphous titanium oxide thin films during annealing treatment,» *Thin Solid Film,* vol. 300, pp. 113-121, 1997.

[104] S. Quesada-Ruiz, Y. Chu, J. Tovar-Pescador, H. Pedro e C. Coimbra, «Cloud-tracking methodology for intra-hour DNI forecasting,» *Solar Energy,* vol. 102, pp. 267 - 275, 2014.

[105] S. Dugaria, A. Padovan, V. Sabatelli e D. Del Col, «Assessment of estimation methods of DNI resource in solar concentrating systems,» *Solar Energy,* 2015.

[106] R. Leutz e A. Suzuki, Nonimaging Fresnel Lenses: Design and performance of solar concentrators, New York: Springer, 2001.

[107] A. Akisawa, M. Hiramatsu e . K. Ozaki, «Design of dome-shaped non-imaging Fresnel lenses taking chromatic aberration into account,» *Solar Energy,* vol. 86, pp. 877 - 885, 2012.

[108] A. Algarue, S. Mahmoud e R. AL-Dadah, «Optical Performance of Low Concentration Ratio Reflective and Refractive Concentrators for

Photovoltaic Applications,» *Energy Procedia*, vol. 61, pp. 2375 - 2378, 2014.

[109] N. Xu, J. Ji, W. Sun, W. Sun, L. Han, H. Chen e Z. Jin, *Energy Conversion and Management*, vol. 100, pp. 191 - 200, 2015.

[110] X. Wang, H. Masumoto, Y. Someno e T. Hirai, «Microstructure and optical properties of amorphous TiO2-SiO2 composite films synthesized by helicon plasma sputtering,» *Thin solid films*, vol. 338, pp. 105-109, 1999.

Publications on peer reviewed journals

- W. Raniero, G. Maggioni, G. Della Mea, M. Campostrini, S. Marigo, and M. Nardo: "Rutherford backscattering spectrometry (RBS) analysis of dichroic systems for optical application", AIP Conference Proceedings 1530, Vol. 133 (2013), AIP Publishing.

- W. Raniero, M. Campostrini, G. Maggioni, G. Della Meaa, A. Quaranta: "Physical vapour deposition reactive magnetron sputtering for the production and application of dichroics in photovoltaic system with solar spectral splitting", Applied Surface Science, Vol. 308, pp. 170–175 (2014), Elsevier.

- W. Raniero, G. Della Mea, M. Campostrini "Functionalization of surfaces with optical coatings produced by PVD magnetron sputtering" IGI-Global, In press.

Participation to congresses, schools and workshops

- W. Raniero, M. Campostrini, G. Maggioni, G. Della Mea , A.Quaranta: "Physical Vapour Deposition Reactive Magnetron Sputtering (PVD) For Realization Of Dichroics Designed for Spectral Separation In Photovoltaic System" Smart & Functional Coatings, European conference, Turin 2013.
- G.Maggioni, W. Raniero, G. Della Mea, M.Campostrini, M. Nardo, S.Marigo: "Rutherford Backscattering Spectrometry (RBS) analysis of dichroics system for optical applications" ION Beam Conference, INFN-LNL 2012.
- S. Novak, V. Singh, N. Patel, J. Marro, J. Giammarco, I. Luzinov, A. Quaranta, W. Raniero, M. Chiesa, A. Agarwal, K. Richardson, "Radiation effects in chalcogenide glass materials for mid-IR photonic

devices," DGG-GOMD: Joint meeting of German Society of Glass Technology and American Ceramic Society Glass and Optical Materials Division, Aachen, Germany, (May 28, 2014).

- "Practical Design and Production of Optical Thin Films" 16th European Conference on Composite Materials (ECCM16), February 10nd-14th 2014, Newcastle, United Kingdom.

- "LabVIEW Core 1" course – Assago (MI), 2013, Italy.

- "LabVIEW Core 2" course – Padua, 2014, Italy.

- 14th International Conference on Plasma Surface Engineering (PSE) September, 15 – 19, 2014, tutorial: "Fundamentals and Trends of Plasma Surface Processing", Garmisch-Partenkirchen, Germany.

Other activities

Project Collaboration

- Collaboration in the LNL-INFN National Project "NORCIA" (Novel Reasearch Challenges in Accelerators), study the deposition of multilayers material for the study and development of resonant cavities for the realization of new particle accelerators resistant to high electro-magnetic fields.

- **Project Collaboration**

  Collaboration with CNR-RFX, study of the properties of electrical insulation at high voltages within the project for the development of an injector of neutral for the fusion experiment "ITER" nuclear fear.

Student tutoring

- Research advisor of a graduate student in Materials Engineering (University of Trento, 2012) regardin the"Realizzazione di un Sistema a separazione spettrale della radiazione solare per applicazioni energetiche".

- Research advisor of a graduate student in Materials Engineering entitled (University of Trento, 2012) regardin the "Progettazione, realizzazione ed ottimizzazione di filtri dicroici utilizzati per la separazione in bande predefinite della radiazione solare".

- Research advisor of a graduate student in Mechatronics Engineering (University of Trento 2014) regardin the "Studio dei fenomeni di scattering per specchi astronomici".

- Research advisor of a graduate student in Materials Engineering (University of Trento 2015) regardin the "Deposizione con tecniche fisiche di film nanometrici di ossidi inorganici per protezione delle superfici di materiali di interesse artistico".

Acknowledgements

I would like to gratefully thank my advisor Prof. Gianantonio Della Mea for giving me the opportunity to join to the research groups at Department of Industrial Engineering (Trento) and Laboratory Materials at LNL-INFN (Padua), where I had the opportunity to implement my technical skills and to collaborate with a several researchers and technicians with high scientific level.

I kindly thank to Prof. Donato Vincenzi for the technical and scientific support and his experience in optical simulation and prototype photovoltaic system.

I would like to thank to Selvino Marigo for technical support in the prototyping phase and his patience that he showed me all these years.
I want to kindly thank all collegues and technicians that working at National Institute of Nuclear Physics (INFN) at Legnaro – Padua, and in particular, Ph.D. candidate Matteo Campostrini and Dr. Daniele Scarpa for technical support and friendship established, Dr. Gianluigi Maggioni, Dr. Sara Carturan and Prof. Alberto Quaranta for the technical skills that have given me over these years.
I want to thank to Ph.D. candidate Matteo Dalla Palma and Ph.D. Annalisa Cataldi for technical cooperation during these years and Dr. Sara Di Salvo for the administrative collaboration.
My gratitude is dedicate to my family Ortensia, Katya, Domenico and my favorite grandson Josef, and also the family of my girlfriend Elena, Diego and Ilaria for all the good deeds that we provide every day.

Special thanks to my girlfriend Laura for supporting me during times of sadness and difficulty, providing me love and indescribable moments of life.

Finally, I would like to thank my beloved father for having transmitted human values such as respect, humanity and sence of duty that will be forever my cultural background.

Trento, 14th December, 2015